

Chapter 2

Basic Interactions

Abstract Understanding the interactions of photons and slow electrons with condensed matter is fundamental for the understanding of the imaging process in emission and reflection electron microscopy with slow electrons. While some of these interactions are common to both emission and reflection imaging, such as the propagation of the electrons in the sample to its surface, there are fundamental differences between the two imaging modes. Following the historical evolution of surface imaging with slow electrons, this chapter discusses first the processes involved in emission microscopy and then turns to those important in reflection microscopy with electrons entering the sample, i.e., to low energy electron microscopy (LEEM). In mirror electron microscopy the incident beam does not interact with the sample but only with the field modification caused by the sample, which is a problem of electron optics and image formation and will be discussed in Chap. 4.

2.1 Fundamental Theories of Electron Emission

In emission imaging the dominant mode has become photoelectron emission while secondary electron emission caused by electron, ion, or fast atom bombardment, which was the most important mode before the advent of ultrahigh vacuum, is not used anymore and will, therefore, be discussed only briefly. Similarly thermionic emission, the main method in the early days, has been relegated to studies of thermionic emitters while in many cases it is a disturbing factor, for example in LEEM at high temperatures. In all imaging methods the sample is in a high field so that in principle field emission can occur too, though only in special cases. For these reasons we will first discuss photoemission, thermionic emission, and field emission briefly jointly within the traditional formalism, then concentrate on the various modes of photoemission on a broader basis and finally consider secondary emission caused by incident particles in connection with photon-created secondary electrons.

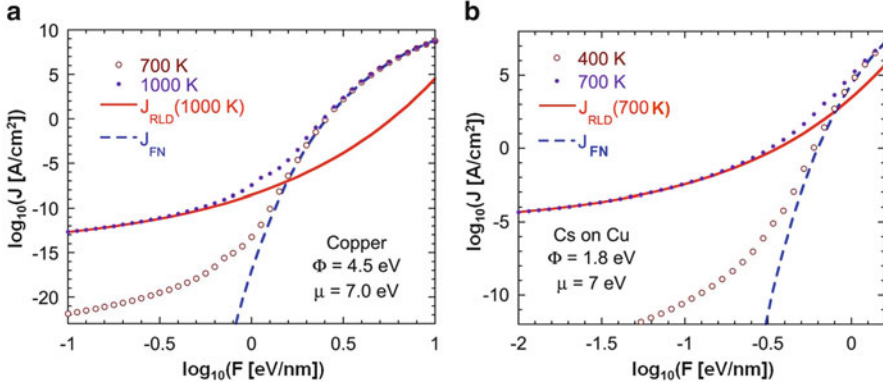


Fig. 2.1 Thermal field emission current density as a function of the applied field strength according to several theoretical models: Fowler-Nordheim (FN, *dashed line*), Richardson-Laue-Dushman (RLD, *full line*), and general field emission model (*dotted and open circle lines*) for two different temperatures). μ is the Fermi energy, Φ the work function. (a) clean Cu, (b) cesiated Cu. Adapted from Ref. [2] with permission from the American Institute of Physics, © 2007

The fundamental theories of thermionic emission (TE), photoemission (PE), and field emission (FE) are the Richardson-Laue-Dushman (RLD) theory, the Fowler-DuBridge theory, and the Fowler-Nordheim (FN) theory, respectively. In emission microscopy the sample is in a high field, at nonzero temperature and in photoemission it is also illuminated so that in principle all emission modes can occur simultaneously. It is therefore useful to consider first generalized theories, which take account of all emission modes in order to see the possible influence of simultaneous TE, FE and/or PE. Purely analytical theories [1] do not allow general predictions because they require numerical evaluation of the resulting equations for specific values of the relevant quantities such as temperature, field, work function, etc. Figure 2.1 shows an example of the total current density for simultaneous TE and FE for two work function values and two temperatures at a chemical potential μ (= Fermi energy E_F at $T=0$ K) of 7 eV [2]. The dashed curves are from the classical (temperature-independent) Fowler-Nordheim theory, the solid curves from the classical (field-independent) RLD-theory for the higher of the two temperatures shown. The open and solid circles are from the general thermal field theory developed in Ref. [2]. Figure 2.1a is typical for Cu, Fig. 2.1b for cesiated Cu. At the lower temperatures there is a clear influence of the field on the emission in both cases but the current densities at typical field strengths used in emission microscopy (0.1 V/nm) are far below those useful for imaging. Only when features with small radius of curvature, which cause strong local field enhancement, are present on the surface, the general thermal field theory becomes relevant. At temperatures at which TE sufficient for imaging occurs, the field influence on emission can be completely neglected. A qualitative way to look at this problem is to compare the field term with the work function Φ in the Schottky equation for the total emitted current

$$J = A_0 T^2 \exp \left[\left(\sqrt{e^3 F} - \Phi \right) / kT \right], \quad (2.1)$$

where $A_0 = 4\pi m k^2 e / h^3 = 1.20 \times 10^6 \text{ A/m}^{-2} \text{ K}^{-2}$ is the universal Richardson constant and F the field strength. For typical fields in emission microscopy $(e^3 F)^{1/2} \leq 0.12 \text{ eV}$, so that the field F has a significant influence only for small Φ . Having thus excluded the influence of the field on TE microscopy—except FE through an insulating barrier in MIM (metal–insulator–metal) or SIM (semiconductor–insulator–metal) cathodes—we restrict the further discussion to the generalized RLD equation for the total emitted current (Eq. (2.1) without the field term). At the same time we take two aspects into account in a phenomenological manner, which are not included in the RLD equation: the averaged quantum-mechanical reflection factor at the surface r and the influence of the band structure with a factor λ_B , by replacing A_0 with the generalized Richardson constant A_G [3]:

$$A_G = \lambda_B (1 - r) A_0. \quad (2.2)$$

Usually also the temperature dependence of $\Phi \approx \Phi_0 + cT$ is included in λ_B via the factor $\exp(c/k)$. Calculations of the influence of these parameters can be found in Ref. [3], experimental results for various tungsten surfaces in Ref. [4]. The total emission current determines the image brightness in emission microscopy and thus the contrast between regions with different Φ , r , and λ_B . Details can be found in the classic paper by Herring and Nichols [5] and in reviews of the subject [3, 6, 7]. For the image resolution the energy, energy distribution, and angular distribution of the emitted electrons are of importance. The energy distribution is well approximated by a Maxwell distribution

$$dJ/dE \sim E \exp(-E/kT), \quad (2.3)$$

which has a maximum E_0 at kT and a full width at half maximum ΔE of $2.45 kT = 21 \times 10^{-5} T$. TE microscopy uses in general temperatures below 2000 K so that $E_0 \leq 0.17 \text{ eV}$ and $\Delta E \leq 0.4 \text{ eV}$. The angular distribution can be approximated by a $\cos^2 \theta$ function because only the normal component of the energy is important for escape into the vacuum. The consequences of angular and energy distribution will be discussed in the chapters on image formation and electron optics (Chaps. 3 and 4).

Next we consider the case of simultaneous TE and PE. Figure 2.2 [2] is an example, again for clean Cu and cesiated Cu parameters. Here the dashed and solid curves show the relative quantum yields $P(\hbar\omega)/P(\hbar\omega_0)$ ($\hbar\omega_0 = 6.2 \text{ eV}$) for clean Cu and cesiated Cu, respectively, the solid and open circles the corresponding curves from the generalized thermal and photo emission theory developed in Ref. [2]. It is evident that at the higher work function values, which are encountered in general, the classical Fowler-DuBridge theory is completely sufficient and that at extremely low work functions only minor deviations occur from it at 600 K. It should be mentioned, however, that the inverse effect to thermal-enhanced

Fig. 2.2 Comparison between Fowler-Dubridge equation (*lines*) and general photoemission equation (*points*) for Cu and cesiated Cu. Adapted from Ref. [2] with permission from the American Institute of Physics, © 2007

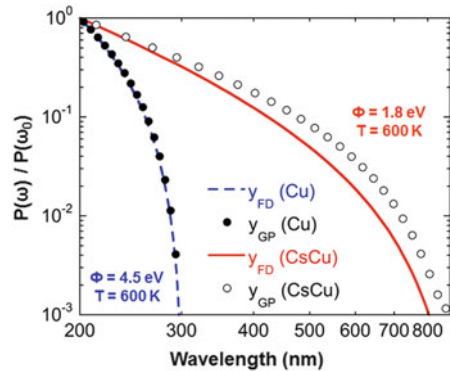
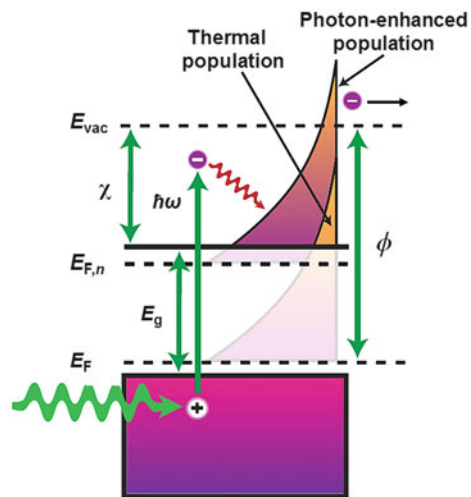


Fig. 2.3 Photon-enhanced thermionic emission from a p-type semiconductor. Photoabsorption shifts the thermal energy distribution of the electrons from the Fermi level E_F to the quasi-Fermi level $E_{F,n}$, thus allowing the high energy tail of the electrons to overcome the work function Φ , electron affinity χ . Adapted from Ref. [8] with permission from Nature Publishing Group (UK)



PE emission, photon-enhanced TE emission, also occurs and can be important in semiconductors [8]. Photoexcitation increases the electron concentration n in the conduction band, which shifts the Fermi level from E_F to $E_{F,n} = E_F + kT \ln(n/n_{eq})$ (n_{eq} equilibrium electron concentration in the conduction band) as indicated in Fig. 2.3. An example is GaN, which has a band gap of 3.4 eV. If its electron affinity is reduced to 0.3–0.4 eV by Cs adsorption then illumination with 3.5 eV photons more than doubles the quantum efficiency from about 320 to 500 K [8]. Of course, these are unusual conditions in emission microscopy. Therefore, we will not dwell any further on the combined effects of TE, FE, and PE, having seen that they are in general not significant in emission microscopy, and concentrate now on the various aspects of pure photoemission.

2.2 Photoemission

2.2.1 General Considerations

The modern theory of photo electron emission phenomena is based in the so-called one-step model [9, 10]. This model treats all aspects of the phenomena within the same framework, from the photo-excitation process via the electron transport to the surface and the transmission through the surface barrier to the detector. These three steps, which were originally treated separately in the properly named three-step model [11] are intimately connected, which makes the three-step model only a first but in many cases a useful approximation. Using it means that the relaxation of the initial N electron system into the final electron system, multiple scattering of the photoelectron and other processes involved in photoemission are not taken into account, a deficiency which is important in photoelectron spectroscopy and photoelectron diffraction but less critical in photoelectron microscopy where other factors such as surface topography and lens aberrations are more important. With this in mind, the discussion in this section will be mainly in the framework of the three-step model. For detailed descriptions of the one-step model and its relation to the three-step model the reader is referred to advanced books which emphasize spectroscopy, diffraction, and other phenomena [12–17].

In the following we outline the general theory of photoemission without going into detail because this is beyond the scope of this book. For the details the reader is referred to the literature on photoelectron spectroscopy cited above, in particular to Ref. [15]. The starting point of the theory of photoemission excited by a photon with energy $\hbar\omega$ is in general Fermi's Golden Rule

$$T_{if} = \frac{2\pi}{\hbar} \left| \langle f | H_{\text{int}} | i \rangle + \sum_n \frac{\langle f | H_{\text{int}} | n \rangle \langle n | H_{\text{int}} | i \rangle}{\varepsilon_i - \varepsilon_n} \right|^2 \delta(\varepsilon_f - \varepsilon_i - \hbar\omega), \quad (2.4)$$

which gives the transition probability per unit time up to second order from the initial state i (ψ_i) of the system with energy ε_i to the final state f (ψ_f) with energy ε_f either directly or via virtual intermediate states n (ψ_n) in response to the Hamiltonian H_{int} . The task is now to choose the wave functions ψ_i , ψ_f , ψ_n and the Hamiltonian H_{int} , which describe the states of the system and its interaction with the electromagnetic wave best. In principle the interaction of an electromagnetic (EM) wave with matter is a problem of quantum electrodynamics, but in practice such a treatment is too complex in general. In view of the fact that the energies involved in photo electron emission microscopy (PEEM) are usually less than 1 keV and only in hard X-ray PEEM (XPEEM) up to several keV, energies which are small compared to the rest mass energy of the electron (511 keV), nonrelativistic approximations of the relativistic equations are sufficient for the interpretation of most PEEM results.

A useful starting point is the nonrelativistic limit of the Dirac equation of a single electron in an electromagnetic field [18], the Pauli-Schrödinger equation. If we neglect relativistic correction terms, which are not important in PEEM, then its Hamiltonian is

$$H_{\text{int}} = \frac{1}{2m} \left(\mathbf{p} - \frac{e}{c} \mathbf{A} \right)^2 + e\Phi - \frac{e\hbar^2}{2me} \boldsymbol{\sigma} \cdot \mathbf{B} - \frac{e\hbar^2}{4mc^2} \boldsymbol{\sigma} \cdot (\mathbf{E} \times \mathbf{p}). \quad (2.5)$$

\mathbf{p} ($= -i\hbar\nabla$) is the momentum (operator), \mathbf{A} the vector potential of the electromagnetic field, Φ the scalar potential, $\boldsymbol{\sigma}$ the spin (operator), \mathbf{B} the magnetic field, and \mathbf{E} the electric field. The last term is the only relativistic correction and represents the spin-orbit interaction H_{so} , the term preceding it is the Zeeman term H_{B} . Both of them cause spin-dependent energy level splitting, which plays an important role in several PEEM subfields. The wave functions Ψ are in the nonrelativistic approximation two-component spinors with the components $|\uparrow\rangle$, $|\downarrow\rangle$, and the corresponding space-dependent wave functions $\varphi_{\uparrow}(\mathbf{r})$, $\varphi_{\downarrow}(\mathbf{r})$. Usually the wave function Ψ is a linear combination of the two spinor functions $\varphi_{\uparrow}(\mathbf{r}) |\uparrow\rangle$ and $\varphi_{\downarrow}(\mathbf{r}) |\downarrow\rangle$, in the following abbreviated with $\psi_{\uparrow}(\mathbf{r})$ and $\psi_{\downarrow}(\mathbf{r})$ or briefly $\psi(\mathbf{r})$.

Equation (2.5) is a one-particle Hamiltonian. The specimens in PEEM are many-particle systems with strong electron-electron interactions, usually in a periodic potential. Electron-electron interactions are generally described by a spin-dependent exchange-correlation potential $V_{\text{xc}}^{\uparrow\downarrow}(\mathbf{r})$. This adds an additional term $H_{\text{xc}} = eV_{\text{xc}}^{\uparrow\downarrow}(\mathbf{r})$ to Eq. (2.5), which can then be written in the form

$$H_{\text{int}} = H_0 + H_{\text{rad}} + H_{\text{xc}} + H_{\text{B}} + H_{\text{so}}, \quad (2.6)$$

with

$$H_0 = -\frac{\hbar^2}{2m} \Delta + eV(\mathbf{r}) \quad (2.7)$$

and

$$H_{\text{rad}} = -\frac{e}{2mc} (\mathbf{A} \cdot \mathbf{p} + \mathbf{p} \cdot \mathbf{A}) + \frac{e^2}{2mc^2} A^2. \quad (2.8)$$

H_0 describes the electron in the potential field $V(\mathbf{r})$ without electron-electron interactions, H_{rad} the interaction of the electron with the EM field. Rewriting $\mathbf{A} \cdot \mathbf{p} + \mathbf{p} \cdot \mathbf{A} = 2\mathbf{A} \cdot \mathbf{p} - \mathbf{A} \cdot \mathbf{p} + \mathbf{p} \cdot \mathbf{A}$, using the commutation rule for \mathbf{A} and \mathbf{p} , $\mathbf{p} \cdot \mathbf{A} - \mathbf{A} \cdot \mathbf{p} = -i\hbar\nabla \cdot \mathbf{A}$, and expressing \mathbf{p} by $-i\hbar\nabla$ we finally arrive at

$$H_{\text{int}} = -\frac{\hbar^2}{2m} \Delta + i\frac{e\hbar}{mc} \mathbf{A} \cdot \nabla + i\frac{e\hbar}{2mc} \nabla \cdot \mathbf{A} + \frac{e^2}{2mc^2} A^2 + V(\mathbf{r}) + H_{\text{xc}} + H_{\text{B}} + H_{\text{so}}. \quad (2.9)$$

From this starting point we can now consider photoemission at different levels of simplification without going into the details of the calculations. The \mathbf{A} -containing terms determine H_{int} , the remaining terms the initial and final wave functions.

2.2.2 The Free Electron Gas Approximation

The simplest model of photoemission assumes that the electrons are free and move in a positive background produced by the homogeneously distributed charge of the ion cores. This produces a potential well with constant potential V_0 , which is filled with electrons up the Fermi level E_F . The Fermi level and the top of the potential well (the vacuum level) differ by the work function Φ . Furthermore it is assumed that there is no magnetic field B . Together with the absence of electron–electron interactions these assumptions reduce the Hamiltonian (2.6) to the first two terms (2.7) + (2.8) with $V(\mathbf{r}) = V_0$. Furthermore it is assumed that the boundary between the semi-infinite potential well and vacuum at $z = 0$ is abrupt and that \mathbf{A} is constant so that $\nabla \cdot \mathbf{A} = 0$. In classical ultrahigh vacuum PEEM (UVPEEM) with Hg arc, D₂, or He lamps the electromagnetic wave is weak enough so that the A^2 term can be neglected but when high-power lasers are used in UVPEEM it becomes important. The spin is taken into account simply by double occupancy of each state in the free electron system (\uparrow, \downarrow). With these assumptions the Pauli-Schrödinger equation becomes the Schrödinger equation with the Hamiltonian

$$H_{\text{Sch}} = -\frac{\hbar^2}{2m}\Delta + eV_0 + i\frac{e\hbar}{mc}\mathbf{A} \cdot \nabla + \frac{e^2}{2mc^2}A^2. \quad (2.10)$$

Kantorovich [19] has solved with this Hamiltonian the Schrödinger equation for a plane incident wave $\mathbf{A} = \mathbf{A}_0 \cos \omega t$ with the Ansatz for the wave function

$$\Psi = \sum_{n=0}^{\infty} \Psi_n \exp \left[-i \left(n\omega - \frac{p^2}{2m\hbar} \right) t \right], \quad (2.11)$$

With $|\Psi_n| \sim |\mathbf{A}_0|^n \sim (E_0 c / \omega)^n$, where E_0 is the amplitude of the electric field of the wave and $p^2 / 2m$ is the kinetic energy of the free electron in the absence of the EM wave. The results of his very condensed paper are shown in Refs. [20, 21]. In brief, the current density of electrons which have absorbed n photons, J_n is proportional to the $2n$ th power of the E_0 , i.e., proportional to n th power of the intensity. For $n = 0$ his results reduces to the RLD (thermionic emission) result, for $n = 1$ to that of the Fowler-duBridge theory [22, 23] (photoemission, which will discussed next) because the fundamental assumptions are identical in these studies.

These fundamental assumptions have some fundamental flaws, the most important one being the assumption of free electrons. Free electrons have a parabolic band structure $E(\mathbf{k}) \sim k^2$. A transition from a lower (at \mathbf{k}_1) to a higher (at \mathbf{k}_2) energy level is therefore possible only if simultaneously a momentum

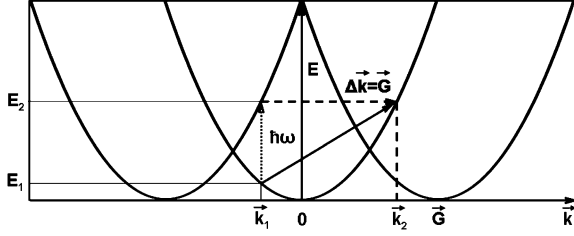


Fig. 2.4 Extended zone scheme of a quasi-free electron metal with the reciprocal lattice periodicity G . The momentum transfer $G = k_2 - k_1$ allows the vertical transition to the higher energy state $E_2 = E_1 + \hbar\omega$

transfer $\Delta k = k_1 - k_2$ occurs, which is much larger than what the photon can supply ($k_{ph} = h/\lambda$). This problem was “solved” by assuming that the surface was providing the necessary momentum, therefore the old name surface photoelectric effect. This should not be confused with today’s surface photoemission from surface states and surface resonances, which are true surface effects. The assumption that the EM wave is constant in the semi-infinite potential well ($A = \text{const}$) is incompatible with the very process of electron excitation, which attenuates the EM field. Likewise, the assumption that all excited electrons reach the interface is also unrealistic, mainly because they lose energy by inelastic scattering on their way to the surface and cannot escape any longer. Mahan [24] has taken these two effects into account. The momentum transfer problem was solved by replacing the homogeneous background charge distribution by the periodic arrangement of the ion cores, which in k space leads to a periodic arrangement of $E(k)$ parabolas instead of a single parabola. Now the interaction of the electron with the lattice provides the necessary momentum, while the photon provides the energy as shown in Fig. 2.4. The surface is now involved only in as much as it imposes the conservation of the parallel momentum of the electron during emission. Mahan calculated also the angular distribution and finally took the band splitting at the reciprocal lattice zone boundaries into account.

Although the free electron model has many inconsistencies as reviewed, for example, by Dobretsov [6], its predictions are in surprisingly good quantitative agreement with many experimental observations, not only from free electron-like metals but also from semiconducting and insulating materials. Therefore, it is appropriate to examine to what extent it is useful for UVPEEM. Obviously it is not applicable for studies, in which the excluded Hamiltonian components play a role, such as in magnetism, spin–orbit splitting, or strong correlations. However, for questions such as the dependence of the photoemission yield upon photon energy or work function the Fowler-DuBridge theory seems to be sufficient. An example is the yield dependence upon photon energy. The theory predicts for the current density

$$J = \alpha A_0 T^2 f\left(\frac{h\nu - \Phi}{k_B T}\right) \quad (2.12)$$

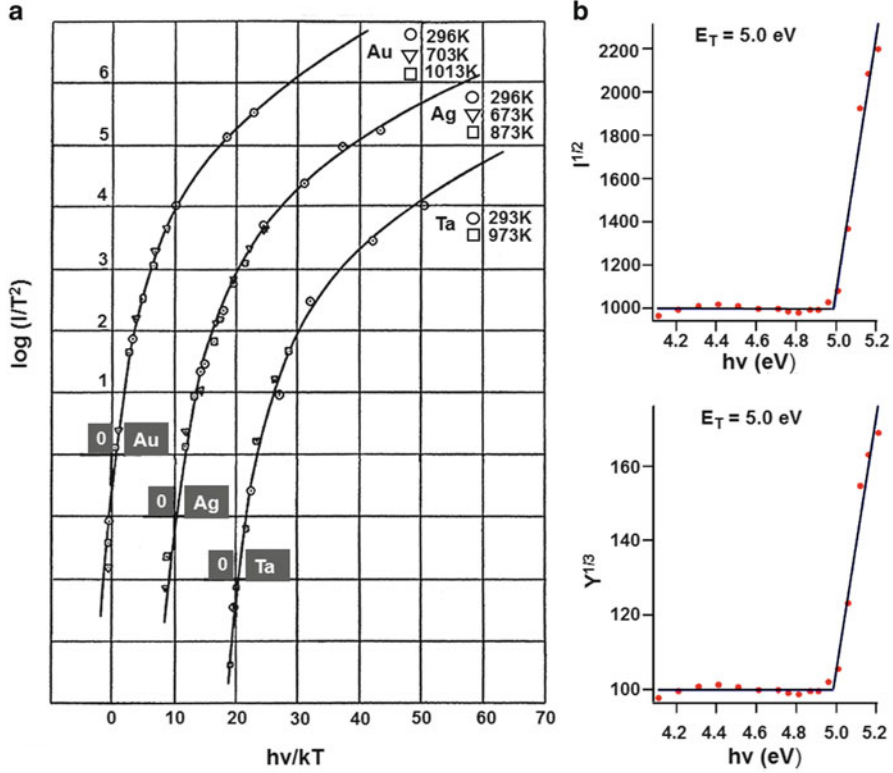


Fig. 2.5 (a) Fowler function of three metals at several temperatures. The zeros are shifted for clarity as indicated. Adapted from Ref. [22]. (b) Photoelectron yield at constant temperature from a single fibrogen molecule as a function of photon energy fitted with different exponents m according to the semiempirical law $Y \sim (h\nu - E_{th})^m$, where E_{th} is a threshold energy. (a) Adapted with permission from Ref. [22]. Copyright 1931 by the American Physical Society. (b) Reproduced from Ref. [25] with permission from the American Institute of Physics, © 2008

where α is a proportionality constant, A_0 the Richardson constant mentioned earlier and

$$\begin{aligned}
 f\left(\frac{h\nu - \Phi}{k_B T}\right) &\equiv f(x) = \int_{-\infty}^x \ln(1 + e^t) dt \\
 &= \frac{x^2}{2} + \frac{\pi^2}{6} - e^{-x} + \frac{e^{-2x}}{2^2} - \frac{e^{-3x}}{3^2} + \dots \quad \text{for } x \geq 0, \\
 &= e^x - \frac{e^{2x}}{2^2} + \frac{e^{3x}}{3^2} - \dots \quad \text{for } x \leq 0
 \end{aligned} \tag{2.13}$$

is the Fowler function. In Fig. 2.5a [22] this function is compared with experimental data for several nonfree electron-like metals, illustrating excellent agreement between theory and experiment.

In UVPEEM a similar agreement should be expected because of the low electron energies all electrons are transmitted through the objective lens so that the total current determines the intensity. In most UVPEEM studies the light source is not monochromatic so that a direct comparison with the Fowler function is not possible. Free electron laser (FEL) light, however, is tunable over a sufficient energy range to allow fitting the emission current with the Fowler formula. Because of the small accessible energy range only the leading term in $f(x)$, $x^2/2$, is taken into account, so that a plot of $J^{1/2}(h\nu)$ should be linear as evidenced in Fig. 2.5b [25] for a biological molecule (fibrinogen). A fit with $f^{1/3}(h\nu)$ is, however, equally good as shown in the lower part of Fig. 2.5b. This power law is one of several, which Kane [26] has suggested for different emission processes from semiconductors. This example illustrates that little can be deduced about the emission process from fits over a small energy range, except an approximate determination of the work function. Data obtained over a wider photon energy range, which can be obtained with synchrotron radiation and are shown later in Fig. 3.48, are more illustrative. They show considerable structure, saturation, or even a decrease of the emission current at high energies, features which are due to changes in the reflectance of the surface with energy, band structure effects, variations of the excitation cross section etc, phenomena not taken into account in the simple free electron-based photoemission theory. At best, we can use the emission current to determine the work function and make use of varying work function across the specimen for work function contrast, but also this can be used only with limitations, which will be discussed later.

2.2.3 Band Structure UV Photoemission

The next aspect, which we have to take into account in photoemission, is the band structure, which has been and is studied extensively with angle-resolved photoelectron spectroscopy (ARUPS, when a He lamp is used or ARPES, when synchrotron radiation is used) [13–17]. UVPEEM without contrast aperture is angle-integrating at very low photon energy—and also energy-integrating without an energy filter—so that the contrast in the real image is determined by the total current. Even with a contrast aperture a wide angular range contributes to the image when a Hg arc lamp is used. All PEEM instruments allow also imaging of the reciprocal space. If equipped with an energy filter, photoelectron diffraction (PED) patterns, and in particular angle-resolved spectra can be obtained. PEEM is increasingly being used together with PED and ARPES, so that we have to discuss here these fields too.

The ARPES spectrum is determined by the band structure and the transition selection rules, which are governed by the crystal symmetry. Although PEEM instruments with energy filters allow fast acquisition of ARPES spectra, their energy and angular resolution is far inferior to that of instruments dedicated solely for this purpose. Thus fine details of these spectra cannot be recorded with PEEM instruments. In addition, the polar and generally also the azimuthal angle of incidence are fixed in PEEM. Furthermore, the accessible emission angle is limited

to a cone normal to the surface, whose cone angle decreases rapidly with increasing electron energy as will be discussed in Chap. 4. Therefore ARPES studies in PEEM are limited in several respects. However, PEEM instruments have the important advantage that the spectra can be taken from very small regions of the specimen down to less than 1 μm in diameter and can be correlated with the microstructure of the specimen. This advantage is enhanced even more in combined spectroscopic photoemission and low energy electron microscopes (SPELEEMs), which allow correlation with the local crystal structure via LEEM and low energy electron diffraction (LEED). (This is important because many specimens are intentionally or unintentionally heterogeneous. High energy and angle resolution instruments generally average over different regions in such specimens.) For this reason we will discuss here, though in a very condensed and somewhat superficial manner, the influence of the crystal structure on the energy and angular distribution of photoelectrons. Detailed discussions of these aspects can be found in Chaps. 6 and 7 of Ref. [15] and in Ref. [27].

In a crystal the band crossings at the periodicity boundaries (Brillouin zones) open up into band gaps and the different periodicities in different directions produce direction-dependent band structures. Simultaneously the localization of the positive charge of the ion cores produces localized fields, which makes the band structure spin-dependent, according to the relativistic correction term in the Hamiltonian (2.5) in the spin-orbit coupling. This is not only true for crystals containing atoms with high nuclear charge but has also to be taken into account in crystals with lighter atoms such as in GaAs for which fully relativistic calculations have been made early in connection with photoemission [28]. In addition, the electron-electron interactions have to be taken into account with the H_{xc} term in the Hamiltonian. Band structure calculations with all these ingredients give the band structure of the ground state of the system with the wave functions ψ_i of the initial state of the photoemission process. The result is usually not presented in the extended zone scheme shown in Fig. 2.4 but in the reduced zone scheme, in which the bands, displaced by the reciprocal lattice vectors \mathbf{G} , are folded back on the zone centered at $\mathbf{G} = 0$. Simultaneously, the reduced zone band structures in the mayor crystal directions are shown side by side. In three dimensions the zone boundaries of the first Brillouin zone are shown in Fig. 2.6a for a fcc lattice with the notation of symmetry points and symmetry directions. Also shown in this figure (Fig. 2.6b, c) [29] is the band structure of Cu, one of the metals whose $J(h\nu)$ dependence fits so well the free electron Fowler function (Fig. 2.5a), despite the strong deviations from the free electron band structure [29].

The interaction Hamiltonian with the electromagnetic wave, which describes the excitation process into the final state ψ_f is usually considerably simplified. We have already discarded the A^2 term and assumed $\nabla \cdot \mathbf{A} = 0 = 0$ for photoemission from the bulk. We also restrict ourselves to the first term in Fermi's golden rule. As a consequence the Hamiltonian H_{rad} in the matrix element M_{if} , which determines the probability for a transition from an initial state i to a final state f , caused by the interaction with the EM wave, becomes

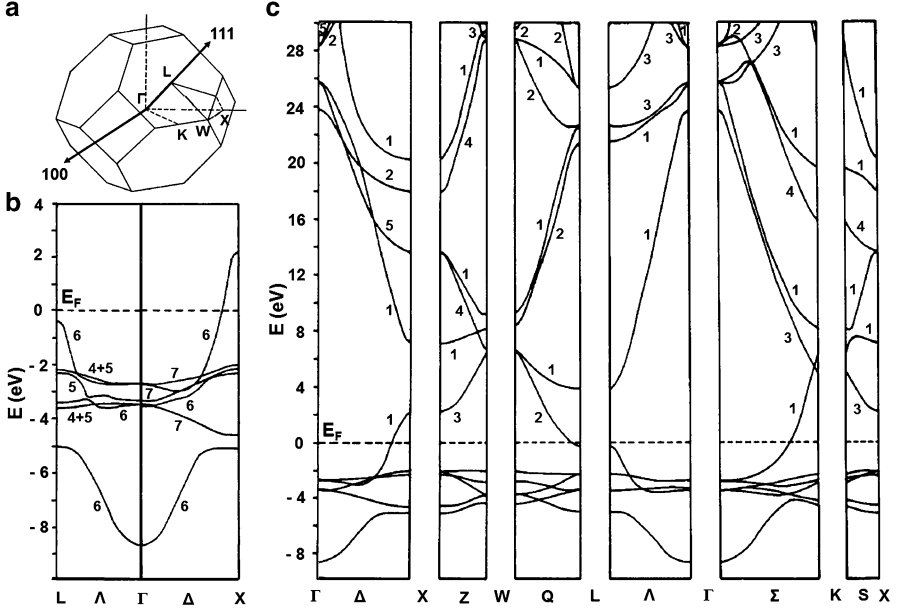


Fig. 2.6 Electrons in an fcc crystal. (a) First Brillouin zone. (b) Relativistic band structure of Cu along the $\langle 111 \rangle$ and $\langle 100 \rangle$ direction. (c) Skalar relativistic band structure of Cu along several high symmetry directions. For explanation see text. (b, c) Reproduced with permission from Ref. [29]. © IOP Publishing 1984. All rights reserved

$$M_{if} = i \frac{e\hbar}{mc} \psi_f | \mathbf{A} \cdot \nabla | \psi_i. \quad (2.14)$$

This matrix element can be expressed in various ways [13–17], usually with the assumption that the wavelength of the EM wave is large compared to the interatomic distances—called dipole approximation—which is well-fulfilled in the wavelength range of interest in band structure UVPEEM. Taking conservation of energy and of momentum into account we can finally write the transition probability as

$$T_{if} = \frac{2\pi}{\hbar} |\psi_f | \mathbf{A} \cdot \nabla | \psi_i |^2 \delta(\varepsilon_f - \varepsilon_i - \hbar\omega) \delta(\mathbf{k}_f - \mathbf{k}_i - \mathbf{G}). \quad (2.15)$$

The wave function ψ_i is obtained by solving the Pauli-Schrödinger equation with the Hamiltonian without H_{rad} . This is in general justified because the incident wave is only a weak disturbance of the system. In the three-step model ψ_f is obtained in the same manner and the propagation to and through the surface is taken into account separately. The one-step model takes into account that the final state consists of the photoelectron and a screened, decaying hole in the occupied states. The photoelectron not only experiences the exchange-correlation interaction

(“self-energy” Σ) and attenuation (imaginary potential V_i), both energy-dependent, but also multiple scattering in the crystal lattice (“inverse LEED state”). The formalisms used in the one-step model can be found in Refs. [13–17]. Even the one-step model calculations do not give quantitative agreement with experiment without fitting Σ and V_i to the experiment as illustrated, for example, in Ref. [30]. Therefore we restrict ourselves to the three-step model, which gives at least semi-quantitative results which are sufficient in general for the interpretation of the ARPES results obtained in PEEM instruments in terms of the *electronic* structure. The extraction of the *atomic* structure from photoelectron diffraction patterns (PED) in the extended UV range up to about 100 eV is difficult because of strong multiple scattering and useful only when no other methods are available such as PED with high photon energies, where single forward scattering is a good approximation in many cases, or LEED when the specimen has sufficient long range order to allow a quantitative LEED analysis.

The knowledge of ψ_i and ψ_f gives also the band structure $E(\mathbf{k})$ which is illustrated in Fig. 2.6 for Cu, together with the Brillouin zone and the symmetry points and symmetry directions (a). Figure 2.6b shows the relativistic band structure (with spin–orbit coupling) in two main symmetry directions ($\langle 111 \rangle$, $\langle 100 \rangle$), Fig. 2.6c the scalar-relativistic band structure (without spin–orbit coupling) for more high symmetry directions up to 30 eV above the Fermi level [29]. The numbers indicate the symmetry properties of the bands, which determine the allowed (vertical) interband transitions between occupied and unoccupied bands. The relevant selection rules, which depend upon the polarization direction of the vector potential (see Eq. (2.15)), for normal incidence and some high symmetry directions can be found, for example, in Ref. [15]. The good agreement between ARPES measurements and theory is also illustrated in the same reference.

In UVPEEM the angle of incidence, measured from the normal is in general between 75° and 45° , the azimuth not in a high symmetry direction and the light is not polarized, laser-UVPEEM experiments excepted. The emission angle range of the photoelectrons around the surface normal can be limited at higher energies with the contrast aperture to a small cone so that some emission angle sensitivity can be achieved in imaging, for example along the $\langle 111 \rangle$ (Λ) direction of a (111)-oriented crystal. Typical cone half-angles range from 2° at 22 eV to 1° at 90 eV electrons with an aperture used for high-resolution imaging. However near threshold the angle is quite large, for example nearly 10° at 1 eV. Without aperture all electrons are transmitted through the objective lens at this energy so that the image brightness is determined by the angle-integrated intensity as already mentioned earlier. This can be calculated from the band structure via the joint density of states defined

$$D(\hbar\omega) = \frac{1}{2\pi^3} \sum_{i,f} \int \frac{d\Omega_{f,i}(\mathbf{k})}{|\nabla_{\mathbf{k}} E_f(\mathbf{k}) - \nabla_{\mathbf{k}} E_i(\mathbf{k})|}, \quad (2.16)$$

where $d\Omega_{f,i}(\mathbf{k})$ is an element of a surface of constant energy difference between initial and final bands and $\nabla_{\mathbf{k}} E(\mathbf{k})$ is the slope of the energy surface $E(\mathbf{k})$.

More conveniently this information is obtained by measurements from a flat polycrystalline surface with completely random orientation of the crystals. In any case the brightness of an UVPEEM image is not simply determined by the work function according to the Fowler-DuBridge theory (Eqs. (2.13) and (2.14)) but depends in general also upon the band structure, the light polarization, the angles of incidence, and the emission angle range used for imaging.

Up to now we have assumed that the amplitude A_0 of the vector potential is constant at the atomic level with the argument that the wavelength in the UVPEEM range is much larger than the interatomic distance. However, at the surface the dielectric constant changes within a short distance and, therefore, also A , invalidating the assumption $\nabla \cdot \mathbf{A} = 0$ made up to now. This case has been discussed in a profound manner by Feibelman [31] and studied extensively in the literature. Strongly simplified, the sudden termination of the crystal lattice produces bonding states (surface states or surface resonances) of the electrons different from those in the bulk and the weaker bonding causes a stronger interaction with the incident wave, modifying A_0 within a short distance. This intimate coupling between EM wave and local electronic properties is, for example, clearly evident in a surface excitation, which has been and is being studied extensively with PEEM, the surface plasmon-polariton. We will come back to this later.

Quite general, surface excitations are important in PEEM because the polar angle of incidence θ is usually large, for example 74° in one of the commercial instruments. Therefore, the normal component A_\perp of \mathbf{A} and consequently also of the electric field, E_\perp , which determines the surface excitation probability, is large. This is evident in many experimental results, for example in the early experiments by Gartland et al. [32, 33] on Cu(111), who observed a maximum in the total photoemission intensity at an angle of incidence of 71° . More recent results for this surface (Fig. 2.7 [34]) show in (a) the quantum efficiency—the angle-integrated number of photoelectrons emitted per incident photon—as a function of θ for three different photon energies. At normal incidence ($A_\perp = 0$) there is only emission from the bulk, which increases with increasing number of accessible bulk states (increasing photon energy), but with increasing θ (A_\perp) emission from the surface state dominates at all energies. The transitions from bulk states, which are possible at the three energies, are indicated by different shading in the surface-projected band structure (b).

This example illustrates that when a surface state exists, it will determine the PEEM image intensity near threshold because of the large angle of incidence and the normal emission. At higher energies the relative contribution of surface states to bulk states decreases strongly because the number of contributing bulk states increases considerably. When a small contrast aperture is used in PEEM, only electrons close to the surface normal contribute to the image. This limits the number of accessible final states and produces intensity variations with energy corresponding to the band structure of the unoccupied states, as illustrated by experiments with Cu(111) and Ag(111) surface states [35]. The band structure causes also a strong nonmonotonic variation of the inelastic mean free path. In view of the strong influence of surface states a brief look at their spatial extension

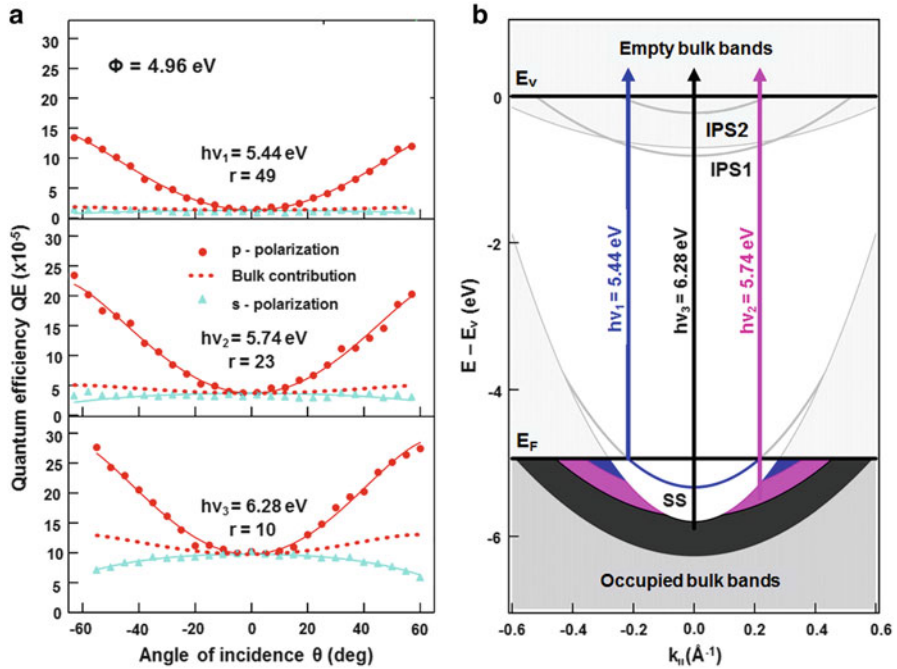


Fig. 2.7 Vectorial photoeffect in photoemission with polarized light. (a) Quantum efficiency from a Cu(111) surface as a function of the incident light angle θ and polarization for the three different photon energies. r is a measure for the relative absorption efficiency of the E_{field} components (or vector potential A) perpendicular and parallel to the surface. (b) Surface-projected band structure of the Cu(111) surface showing the initial states from which electrons can be excited above the vacuum level. Low energy light (blue) can cause emission nearly only from surface state (SS) but with increasing energy (pink and black) also bulk states are increasingly accessible. What is important for PEEM is the strong increase with increasing θ (increasing E_{\perp}). Adapted from Ref. [34] with permission from the American Institute of Physics, © 2008

normal to the surface is appropriate. Figure 2.8 [36] shows the wave functions of the surface state and of a bulk state with comparable energy, together with the potential $V(z)$ as a function of distance from the surface for Al(111) and Be(0001). It is evident that strong potential variations cause a strong localization and high amplitude of the surface state while weak potential variations cause significant overlap of surface and bulk state.

The results shown in Fig. 2.7 were obtained with single photon photoexcitation. Multiphoton excitation opens up additional channels for photoemission. This is illustrated in Fig. 2.9 for multiphoton photoemission (n PPE) normal to the Cu(100) surface [37]. This surface has no surface state but a surface resonance (SR) and similar to Cu(111) two image potential states (IP). One of them is indicated in the right hand side of the figure, which shows the band structure along the surface normal (in the lower half) and the n PPE transitions induced by multiple absorption of 3.07 eV photons. The resulting photoelectron yields are shown on the left side of the figure. It is apparent that the high intensity of 3PPE and 4PPE is mediated

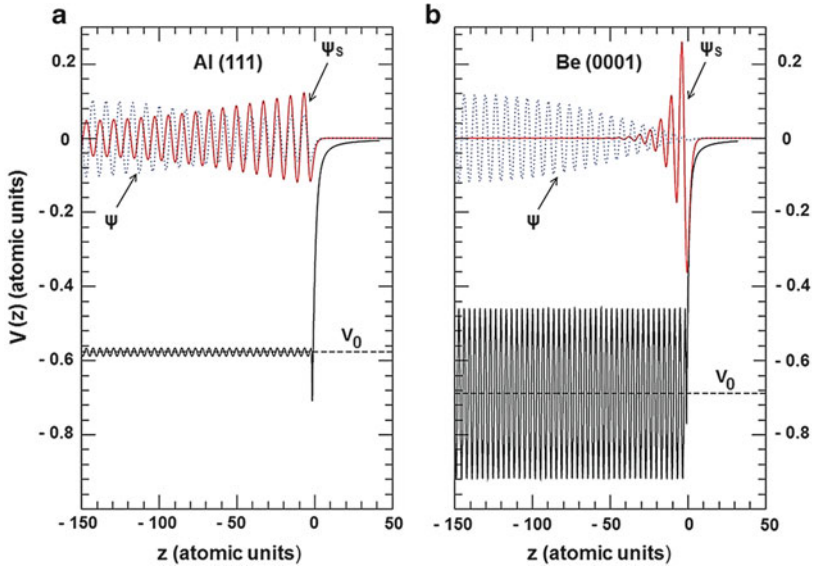


Fig. 2.8 Surface state Ψ_s (red) and bulk state Ψ wave functions (gray) of Al(111) (a) and Be(0001) (b). The potential $V(z)$ is shown in black. Although the mean inner potential V_0 of the two metals is similar, the Be potential is much more corrugated, which is responsible for the rapid decay of the surface state into the bulk compared to Al. Reprinted with permission from Ref. [36]. Copyright 2012 by the American Physical Society

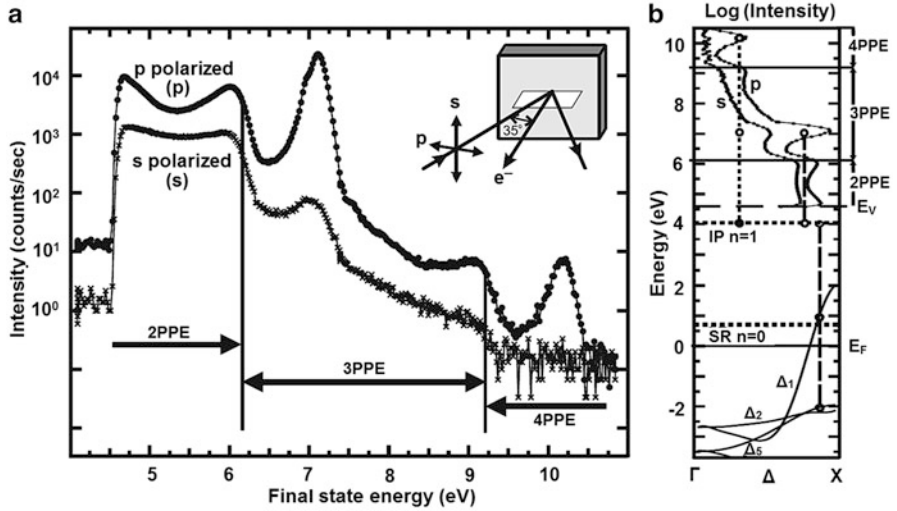


Fig. 2.9 Above threshold photoemission mediated by n -photon absorption from Cu(100) (work function $\Phi = 4.63$ eV). (a) Normal emission multiphoton photoelectron yield excited by p- and s-polarized frequency-doubled light from a Ti:sapphire laser ($\hbar\omega = 3.07$ eV) in logarithmic scale; $\theta = 35^\circ$. The arrows show the contributions of the various n PPE processes, the inset the experimental geometry. (b) Illustration of the 3PPE and 4PPE transitions via an image potential state IP leading to the $I(E)$ dependence shown in (a). Adapted with permission from Ref. [37]. Copyright 2006 by the American Physical Society

by transition to the IP 1 state followed by absorption of one or two more photons. A full understanding of the spectrum, in particular of the lower efficiency of 2PPE compared to 3PPE, requires a detailed discussion of the band structure, which can be found in the original publication [37]. Much of the information from photoelectron spectroscopy discussed here has not been used yet in PEEM but should become important with increasing use of spectroscopic instruments. The n PPEEM studies made to date usually show many spots with much higher intensity (“hot spots”), which very likely are also present in the laterally averaging spectroscopy studies and may distort the spectra unless they have the same spectrum as the rest of the surface. An interesting phenomenon involving n PPE is the emission from negative electron affinity diamondoid (tetramantane-6-thiol) monolayers on Ag(111) and Au(111) surfaces. With 400 nm light $n=2$ was observed, with 800 nm light $n=3.7$ [38]. The narrow energy distribution and high yield makes this phenomenon promising for high brilliance pulsed electron sources.

2.2.4 Spin Effects in UV Photoemission

Up to now we have not taken the spin of the electron into account although spin-orbit coupling makes the band structure and consequently also interband transitions spin-dependent, irrespective of whether or not the material is ferromagnetic or antiferromagnetic or not. Spin-polarized photoemission has been studied for a long time, both with conventional light sources such as HeI light (21.2 eV) and with synchrotron radiation [39–42]. Most work was done with circular-polarized light but for special geometries and symmetries linear-polarized light also allows spin-discrimination. Here we show only a recent example of spin selection in a nonferromagnetic material, Cu(100), using 3PPE, circular polarization, and normal emission. Figure 2.10 [43] illustrates the principle and the result: (a) the 3PPE transition from the spin-orbit split bands of the relativistic band structure shown already in Fig. 2.6 near the zone boundary via the unoccupied sp band and the image potential state to final unoccupied states; (b) the k -region, in which the transitions occur is re-plotted strongly distorted along the energy scale together with the transitions A and B with opposite spin orientation (top). The non-spin-resolved spectrum obtained with a fundamental energy of 3.05 eV, displayed in (b) (bottom), shows that the two spin signals differ by more than a factor of two. This bodes well for energy-resolved magnetic imaging of ferromagnetic materials without spin detection. Its usefulness for PEEM of nonmagnetic materials is not obvious, although strain, step bunches, adsorbate islands can modify the spin-orbit splitting so that they could be imaged this way in principle. However, the work function changes caused by these surface modifications provide a much direct and easier way to image them.

In ferromagnetic materials the situation is quite different. In addition to the spin-splitting of the energy bands caused by the spin-orbit interaction we have the spin-splitting caused by the exchange interaction. This opens up additional routes for spin-dependent photoelectron emission as illustrated in Fig. 2.11 for a

Fig. 2.10 Spin-selected photoemission via circular-polarized three photon photoemission (3PPE, $\hbar\omega = 3.07$ eV) from spin-orbit split states of Cu(100); $\theta = 42^\circ$. For explanation see text. Adapted with permission from Ref. [43]. Copyright 2008 by the American Physical Society

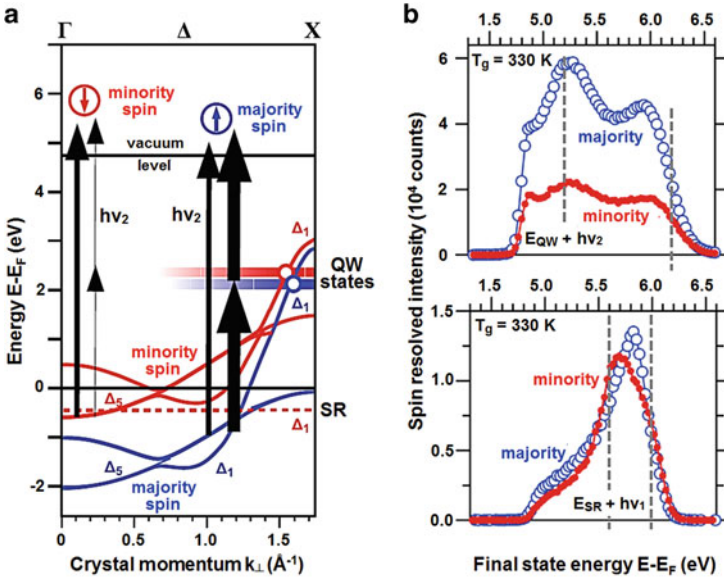
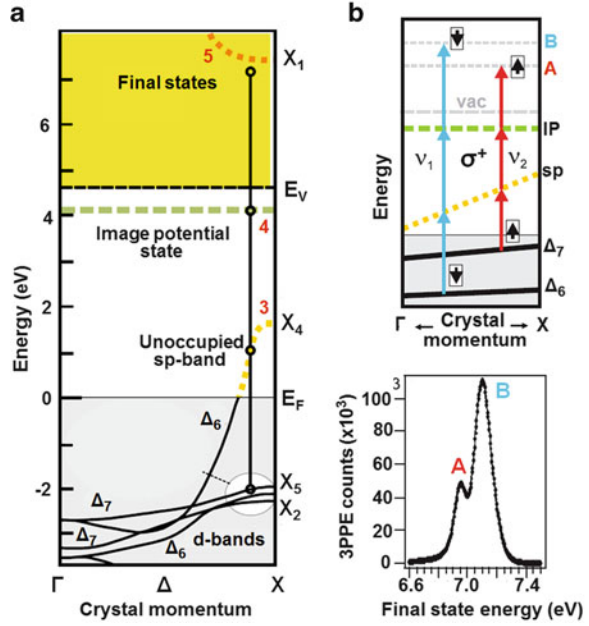


Fig. 2.11 Spin-selected photoemission via linear-polarized one- and two-photon photoemission ($\hbar\omega = 3.1$ eV) from exchange-split states in a fcc Co film on Cu(100); $\theta = 45^\circ$. For explanation see text. Adapted with permission from Ref. [44]. Copyright 2012 by the American Physical Society

6-monolayer thick epitaxial fcc Co film on Cu(100) for emission normal to the surface upon excitation with p-polarized light incident at 45° [44]. Co(100) has a surface resonance and the film has a quantum well state near the zone boundary. In the band structure picture (a) the transitions possible from the exchange-split bands via one and two photon absorption with photon energies of $h\nu_1 = 6.0$ eV and $h\nu_2 = 3.1$ eV, respectively, are indicated by arrows whose width indicates their relative contribution to the intensity; (b) shows the spin-resolved intensities for 2PPE as a function of final state energy (top) and the corresponding results for 1PPE (bottom). It is obvious that the transition from the majority spin band via the quantum well state is more than a factor of 2 stronger than the transition from the minority spin band, while in the corresponding 1PPE transition the difference is much smaller. This example points out the importance of multiphoton photoemission and of sufficiently long-lived intermediate states for spin-resolved measurements such as for spin-resolved PEEM. It is interesting to note that the energy dependence of the final state intensity in the 2PPE transition in the Co film is quite sensitive to the film structure but not the spin polarization of the emitted electrons.

Spin-resolved PEEM becomes important whenever the direction of the spin alignment is not homogeneous. In the bulk the alignment is determined by the magnetocrystalline anisotropy, which is caused by the spin-orbit coupling but in thin films or small particles other anisotropies dominate the alignment: surface and interface anisotropy, magnetoelastic anisotropy caused by misfit strain, and shape anisotropy, a consequence of the shape- and size-dependent strayfield energy. The competition between all these anisotropies breaks up the homogeneous spin alignment into domains with different spin-orientations, separated by domain walls. Spin-resolved PEEM allows studying these domains and domain walls as a function of applied field, temperature, and other influences such as current through thin magnetic wires (spin current). An example of the application of the 2PPE process illustrated in Fig. 2.11 is the imaging of the domain structure of a 8-monolayer thick Co film on Cu(100) with an imaging spin-filter [45], using p-polarized light, which will be described in Chap. 3.

It should be mentioned that magnetic domain images excited by p-polarized light can also be obtained in near threshold emission without spin filter. Actually the first UVPEEM domain images were from a 100 nm thick polycrystalline Fe film, excited with light from a Hg high-pressure arc lamp [46]. Without spin selection magnetic contrast is obtained by changing the magnetization direction, subtracting the resulting images, and dividing by their sum pixel by pixel. This gives the magnetic linear dichroism (MLD) asymmetry image $A_{\text{MLD}} = [I(M_+) - I(M_-)]/[I(M_+) + I(M_-)]$. The magnetic contrast in this film cannot be explained in terms of a picture similar to that shown in Fig. 2.11 because the film is polycrystalline, has no quantum well state and the photon energy is too low for excitation into one of the known unoccupied states. Therefore, a phenomenological explanation in terms of a photoemission counterpart to the magneto-optical Kerr effect was given.

Magnetic *linear* dichroism is restricted to certain measurement geometries and crystal symmetries [27, 39–42]. Therefore, most of the magnetic

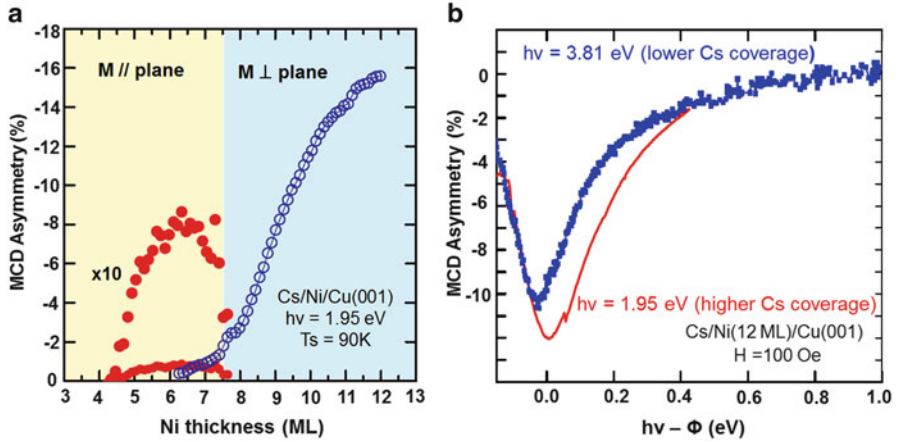


Fig. 2.12 Threshold magnetic circular dichroism (MCD) in photoemission. (a) Thickness dependence of the MCD of a cesiated Ni film on Cu(100) surface with work function $\Phi = 1.8$ eV, measured via the drain current from the sample. (b) Dependence of the MCD of a cesiated 12 monolayer thick Ni film on Cu(001) upon the difference between photon energy and work function. Adapted with permission from Ref. [47]. Copyright 2006 by the American Physical Society

dichroismspectroscopy studies used *circular* polarized light, which has fewer restrictions. In magnetic circular dichroism (MCD) measurements usually the helicity of the circular polarized light is changed instead of the magnetization direction and the MCD asymmetry A_{MCD} is defined by $(I_r - I_l)/(I_r + I_l)$, where r and l stand for right-handed and left-handed helicity. As an introduction to threshold MCDPEEM Fig. 2.12 [47] shows some results of the MCD calculated from total emission current measurements, that is measurements without angle and energy selection, from epitaxial Ni films on Cu(100). Illumination with 1.95 and 3.81 eV light was used. Up to a thickness of 7.5 monolayers the magnetization in these films is in the film plane, above this thickness perpendicular to the film plane as indicated in Fig. 2.12a. The work function of the surface was adjusted by Cs deposition so that with 1.95 eV photons threshold emission occurred. At threshold the MCD is largest as seen in Fig. 2.12b, which shows the dependence of the MCD upon the difference between photon energy and work function for two different photon energies. In contrast, the total emission current increases strongly. This difference is due to the fact that additional transitions with opposite sign of the MCD or zero MCD from different energy bands near the Fermi level become possible. This indicates the unique possibilities of threshold MCD for magnetic imaging, which were demonstrated soon thereafter [48] with Cs-adjusted threshold PEEM with 3.05 eV cw laser and a 3.06 eV pulsed laserlight incident at 55° , using the same 12 nm thick Ni film as in Fig. 2.12b. Thus threshold MCDPEEM promises to become an important magnetic imaging method, though somewhat limited by the need of adjusting the work function to the photon energy. This adjustment is limited by the availability of tunable bright light sources in the energy range of most work functions.

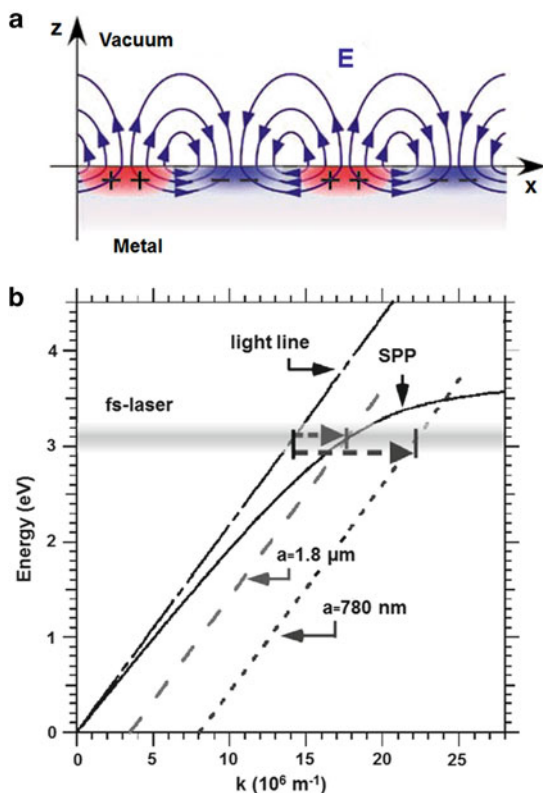
Before leaving the subject of spin-related effects another relativistic effect should be mentioned yet, which occurs on surfaces with a large potential gradient, equivalent to a strong electric field, the Rashba effect [49]. It causes an energy splitting which is proportional to the momentum k of the electron. In the nearly free electron picture the Rashba effect is at constant energy apparent in two concentric rings instead of one ring in k space, with the spin rotating in opposite direction in the two rings. The study of this phenomenon has been the domain of high-resolution ARPES but in cases, in which the energy splitting is large it is also accessible to spectroscopic PEEM in the reciprocal space imaging (LEED) mode. Using the field-limiting aperture allows studying variations of the Rashba effect across the surface in the submicron range.

2.2.5 Surface Plasmon Photoemission

The pulsed laser multiphoton photoemission experiments described in the previous paragraphs were made on well-prepared smooth surfaces and could be interpreted in terms of the band structure including quantum well and image potential states. It had been observed already around 1990 that pulsed lasers with photon energies below the work function could produce emission of energetic electrons. Aeschlimann et al. [50] studied this phenomenon on Cu(100) and Cu(110) single crystal surfaces. They noticed that the electron yield depended strongly on the surface roughness and attributed the strong emission to surface plasmon excitation, based on Raether's work [51]. Raether's group had studied surface plasmons in depth with electron energy loss spectroscopy and optical methods and had found that their oscillations can enhance the local field strength of the incident wave by orders of magnitude. The physics of localized surface plasmons (LSPs) and of surface plasmon polaritons (SPPs, evanescent surface electromagnetic waves) [52–56] connected with propagating surface plasmons (charge density wave) has developed into an important field, mainly because of its possible practical application in many fields, in particular in nano-optics ("plasmonics") [57–62].

Here we briefly summarize only the basics needed later in the discussion of plasmon-PEEM (Chap. 6). Plasmons can be excited by light in materials, whose real part ϵ_1 of the complex dielectric function $\epsilon = \epsilon_1 + i\epsilon_2$ is negative and its imaginary part $\epsilon_2 \ll \epsilon_1$. Ag is the best material from this point of view, followed by Au, with Cu in some distance. In these materials plasmons can be excited in many forms of the specimen. We discuss here only the limiting cases, the perfectly smooth planar surface and the small spherical or ellipsoidal particle. The charge distribution and associated electric field of a SPP on a planar surface is illustrated in Fig. 2.13a [63]. The energy of a SPP depends upon its wavelength as shown by the dispersion relation marked SPP in Fig. 2.13b [63]. Its energy comes from absorption of light, whose dispersion relation is shown by the light line. For absorption to occur energy and momentum have to be conserved. This can be achieved (1) by changing the slope of the light line so that it intersect the SPP curve or (2) by shifting the light line to

Fig. 2.13 Surface plasmons. (a) Charge distribution and associated electric field of a surface plasmon. (b) Dispersion relation of surface plasmons and coupling with light. For explanation see text. From Ref. [63] with permission. Copyright 2008 The Vacuum Society of Japan



the right as indicated in Fig. 2.13b. Method (1) is the classical Kretschmann method of illuminating a very thin film on a prism with refractive index n from the backside, which reduces the slope of the light line by a factor $1/n$ so that it intersects the SPP curve. This is impractical for PEEM, though possible in principle, while solution (2) is simpler to realize because it can be done by illumination from the front. The shift implies a momentum transfer. This is achieved either by diffraction from a surface grating or by scattering from small surface irregularities, which can be produced in nearly any size, shape, and distribution. In the first method a true SPP is produced, also called surface plasmon wave (SPW) [64]. In the second case localized surface plasmons (LSPs) are excited, which can also support a SPW via coupling between the LSPs. In both cases the radiation fields of the oscillating charges cause a strong enhancement of the incident wave field, producing the high fields mentioned above. For example, for plasmon excitation in a flat Ag film in the Kretschmann set-up the plasmon field is under optimum conditions (zero optical reflectivity) up to 250 stronger than the incident field at a wavelength of 600 nm. The same field *intensity* enhancement $E_{\text{Plas}}^2/E_{\text{inc}}^2$ can also be achieved with grating excitation [51]. However, with increasing deviation from the optimum conditions

the field enhancement decreases strongly, for example to 80 at 420 nm. The decay length ($1/e$ distance) of the plasmon field into the vacuum is in the 100 nm range, for example 390 nm in the case of Ag under the optimum excitation conditions mentioned, *into* the metal it is the skin depth, 24 nm and the decay length of the SPP *along* the surface is 36 μm . Taking the group velocity $d\omega/dk$ —the slope of the SPP curve in Fig. 2.13b, divided by \hbar —into account, a lifetime of the SPP in the low 10 fs range follows. The short decay length and life time of these evanescent waves is due to energy transfer from the collective charge fluctuations of the plasmon to phonons (heating), to photons (radiation), and to electrons (single electron excitations), the last transfer being the process of interest in PEEM.

The second limiting case, the small particle is illustrated in Fig. 2.14a [65] for a spherical particle. Under the influence of the oscillating field the electrons oscillate collectively, forming localized charge oscillations in the field direction. The field *amplitude* enhancement factor $FEF = |F_n|/|F_{\text{inc}}|$ (F_n normal component of oscillating field) caused by these oscillations are shown for spherical and ellipsoidal particles with an axial ratio $a/b = 3$ along the long axis in Fig. 2.14b, c [66] for different particle sizes and shapes. For $a/b = 5$ and $a = 25$ nm $FEF = 250$ at the optimum wavelength, similar to the maximum values for the flat film. This change in the interaction with aspect ratio is illustrated by extinction measurements from well-defined particles prepared by electron beam lithography in Fig. 2.14d, e [67] for polarization parallel and perpendicular to the long axis, respectively for $b \approx 40$ nm. The large difference between the two polarization directions due to the different polarizabilities and the log scale should be noted. A detailed account of this limiting case can be found in Ref. [68].

The two limiting cases show that large field enhancements can occur in a wide range of specimen configurations and excitation modes. The question is now how large are the plasmonic fields. The average intensity of the incident wave is connected with the amplitude of the electric field by $I = 0.5c\epsilon_0 E_0^2 = 26.544 \times 10^{-4} E_0^2$, where E_0 is measured in V/m and I in W/m^2 . For an average intensity of 10^{12} W/m^2 , which is in the range used in many experiments, the peak field strength E_0 is $\approx 0.2 \times 10^8 \text{ V/m}$. At this field strength no field emission can occur. The onset of field emission is usually characterized by the Keldysh parameter $\gamma = \omega(2m\Phi)^{1/2}/eE$, which depends upon the frequency ω of the light wave, the work function Φ , and the field E . For $\gamma \ll 1$ electrons tunnel through the barrier, for $\gamma \gg 1$ they are excited over the surface barrier via multiphoton photoemission. At the frequently used wavelength $\lambda = 800$ nm, corresponding to $\omega = 2.35 \times 10^{15} \text{ Hz}$, $\gamma = 1$ at a field strength of $2.26 \times 10^{10} \text{ V/m}$ for Ag whose work function is 4.26 eV. We will discuss here only the case $\gamma > 1$, i.e., multiphoton photoemission ($n\text{PPE}$), which is experimentally verified by the dependence of the emission current upon light intensity, $I_n \sim E^{2n}$. At low intensities, e.g., in the 10^{11} and low 10^{12} W/m^2 range 2PPE is observed and the energy distribution of the emitted electrons reflects the density of states of the material [50, 69–71]. With increasing power 3PPE and even 4PPE occurs and the energy distribution changes dramatically, with energies far above those expected from the absorbed photon energy. For example, Irvine et al. [72] observed at an intensity of

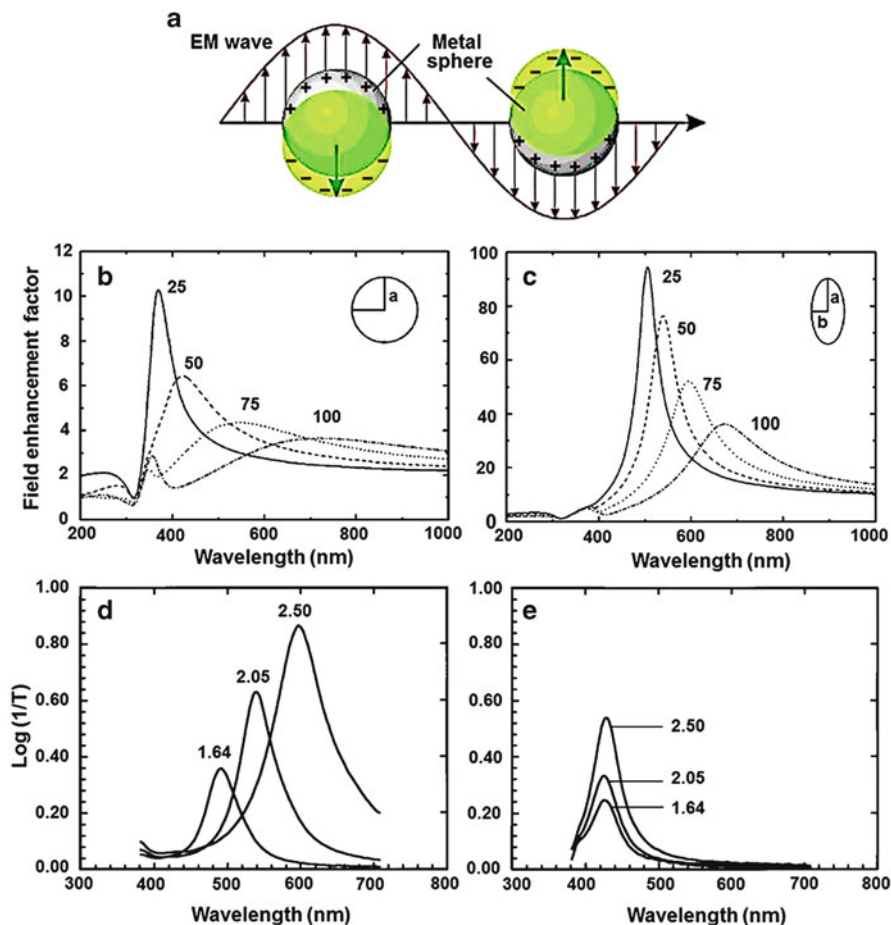


Fig. 2.14 Plasmons in small particles. (a) Schematic of the excitation of synchronous charge fluctuations in the particles by an incident electromagnetic wave, which produces plasma radiation, leading to a strong enhancement of the electromagnetic field. (b, c) Dependence of the field enhancement on the size of (b) spherical particles and (c) ellipsoidal particles with $a/b = 3$ as function of wavelength; a in nm, dielectric constants of Ag, wave incident along horizontal direction. (d, e) Extinction ($1/\text{Transmission}$) of light incident on 30 nm thick elliptically-shaped Ag particles for various a/b ratios with $b \approx 40$ nm as a function of wavelength incident (d) parallel and (e) perpendicular to the long axis. (a) Adapted with permission from Ref. [65]. Copyright 2003 American Chemical Society. (b, c) Adapted with permission from Ref. [66]. Copyright 2004 by the American Physical Society. (d, e) From Ref. [67] with permission from Optical Society of America

$1.8 \times 10^{13} \text{ W/m}^2$ 3PPE and a maximum of the energy distribution at 315 eV with a full width at half maximum (FWHM) of 83 eV. They attributed the high energy and large energy width to acceleration of the electrons by the ponderomotive force of the oscillating surface field. The energy of an emitted electron is determined by the phase of the field at which it is ejected from the field. In order to achieve agreement

between calculation and experiment a field enhancement factor of about 10^3 was necessary, higher than what has been mentioned above. At somewhat lower intensities ($(0.17\text{--}0.89) \times 10^{13} \text{ W/m}^2$) Aeschlimann et al. [50] observed an energy-dependent power dependence of the emission ($n = 2.8$ at 0.8 eV and 3.2 at 2.5 eV) and an exponential decrease of the intensity with energy up to 6 keV at the highest power, which was attributed to field enhancement at hot spots. The wide energy spread reduces the resolution in PEEM so that most PEEM experiments (Chap. 6) use lower laser powers to which we restrict the following discussion of the recent theoretical results.

Most calculations assume a free electron metal. The most detailed treatment of interest for n PPE has been given by Yalinin et al. [73]. They calculated the total emission current and its angular distribution for 800 nm light ($\omega = 2.35 \times 10^{15} \text{ Hz}$), work function $\Phi = 5.5 \text{ eV}$ and initial-state energy (Fermi energy) of 4.5 eV as a function of the amplitude E_0 of the incident light for pulse durations between 2.7 and 27 fs . They found good agreement between three different theoretical approaches and approximations, including the solution of the one-dimensional Schrödinger equation. In the range of interest for PEEM—their weak-field regime—they obtained a power dependence of the emission probability upon E_0 with $n = 4$ for $\Phi = 5.5 \text{ eV}$ and with $n = 5$ for a fictive $\Phi = 7.1 \text{ eV}$. However with increasing E_0 increasing deviations from the integer values occurred (Fig. 2.15a) [73], which they attributed to decreasing reflection of the oscillating electron in the oscillating ponderomotive field at the surface. This could, for example, explain the deviations mentioned above. Details of the angular distribution, of the time-dependent field, etc., can be found in their paper. Here it should only be mentioned that it does not include the image potential and the field penetration but nevertheless accounts for many experimental observations. The field penetration (or induced potential) plays an important role at and near the surface plasmon resonance. This is illustrated in Fig. 2.15b [74], which shows the energy distribution of the electrons emitted normal to the surface upon excitation by very short pulses with the surface plasmon frequency ω_s . Figure 2.15c [74] gives a visual impression of the induced potential. In an earlier study of the same system (Al(111)) [75], which was limited to $\omega > \omega_s$, the field penetration was not taken into account. The results showed features observed in experiments, for example the exponential decrease of the intensity with energy mentioned above. Details can be found in this paper. Band structure effects, including surface states seem to change the energy distributions calculated for the free electron model little for Al but have a strong influence in Be. This has been attributed to the much stronger localization of the surface state in Be than in Al, illustrated in Fig. 2.8, with a correspondingly much higher density of states in it in Be than in Al [36]. Thus, while it appears that the free electron model can explain many experimental results, there are also many details, which are material-specific. The details of plasmon-mediated photoemission depend on many factors: (1) the properties of the plasmon-exciting wave, such as pulse frequency, length, shape, intensity, polarization, (2) the properties of the specimen such as period, profile, and length of the grating, size, shape, and distribution of particles, (3) the relation between incident wave and specimen,

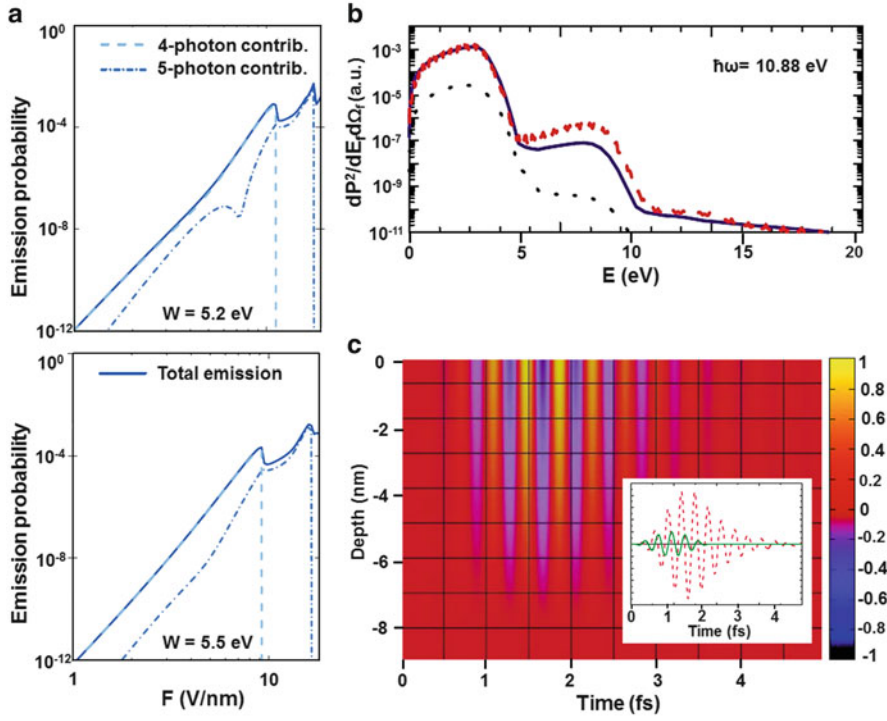


Fig. 2.15 Influence of field enhancement on photoemission due to plasmon excitation by high power fs pulses. (a) Contributions of 4PPE and 5PPE processes to the total (full line) emission probability for a work functions of 5.2 eV (*top*) and 5.5 eV (*bottom*) and $\hbar\omega = 1.55$ eV (Ti:sapphire laser) as function of field strength. The 4PPE is the threshold multiphoton process and dominates the total emission. Above 18 V/nm tunneling occurs. (b) Differential electron emission probability as a function of the electron energy for normal emission, excited at the surface plasmon frequency. The *dashed* and *solid* curves take the induced potential into account, the *dotted* curve not, indicating the strong influence of the induced potential on the emission probability at all energies. (c) Induced potential as a function of time and distance z perpendicular to the surface for excitation at the plasma frequency. The *inset* shows the laser pulse (*solid* line) and plasmon pulse (*dashed* line) at a depth of 2.5 nm. (a) Reprinted with permission from Ref. [73]. Copyright 2011 by the American Physical Society. (b, c) From Ref. [74] with permission from Optical Society of America

such as angle of incidence—also azimuthal angle in case of non-isometric particles—, match between frequency of incident wave and particle size- and shape-dependent plasmon frequency, and other parameters. Therefore a comparison between theory and experiment and even between different experiments is difficult.

For applications in plasmon nanooptics the decay length along plasmon stripes or wires, which is determined by the plasmon life time, and the coupling between wires and particles via the plasmonic radiation field, which is determined by the decay length is important. In the past optical and laterally integrating photoemission measurements were used to characterize the radiation field and scanning

electron microscopy (SEM) to characterize the structure of the patterns. PEEM can accomplish both in the 10–100 nm range and has been used very successfully for this purpose as we will see in Chap. 6. In both cases the same light sources and plasmon materials are used: predominantly Ti:sapphire laser-based systems with repetition rates between 75 and 95 MHz, pulse widths of several 10 fs, pulse energies of the order 1 nJ, power densities between 10^2 and 10^3 MW/cm² resulting in field strengths in the 10^6 V/cm range. These systems are tunable over a narrow wavelength range (typically from 770 to 830 nm, corresponding to 1.61–1.49 eV), which gives some flexibility in the adaption to the plasmon material. In order to overcome the work function of the material the pulses are first frequency-doubled so that emission via 2PPE becomes possible or high radiation power is used to excite n PPE with $n > 2$. Free-electron-like metals, for which most of the theoretical work has been done, have either very high surface plasmon energies, such as Al, or are very reactive such as the alkali metals, or have no well-defined plasma resonances. For these reasons Ag, Au, and to a certain extent also Cu, are the materials of choice. Furthermore their surface plasmon energies are in the range accessible with frequency-doubled light from the Ti:sapphire laser. As will become evident in Chap. 6 there are additional reasons for the choice of this laser in PEEM.

2.2.6 X-Ray Photoemission

From the point of view of PEEM X-ray photoemission may be divided into three groups: (1) slow secondary electron emission, (2) Auger electron emission, and (3) true photo electron emission. Auger electron emission is rarely used in PEEM because the strong peaks involve two electrons in the valence band. As a consequence the peaks are broad and much less suited for imaging than the true photoelectron peaks. Therefore, they will not be discussed here. For the first group a more appropriate name would be XSEEM but the acronym XPEEM has been generally accepted also for secondary electrons, not only for true photoelectrons. The argument for this usage is that the intensity of the secondary electrons is determined by the ionization cross section of inner shells just like in true photoemission. We start, therefore, with the third group although it is less widely used for two reasons: (1) it requires an energy filter, with which in many instruments are not equipped and (2) the intensity of secondary electrons is usually much higher than that of the true photoelectrons, which allows faster image acquisition. We call in the following the true photoelectrons simply photoelectrons and the electrons in the first group secondary electrons.

2.2.6.1 Photoelectron Emission

The characteristic parameters in this emission process are photoelectron energy, intensity, and angular distribution. The first two are determined by the binding energy E_B of the core level, by the polarization-dependent selection rules and by the

photon energy $\hbar\omega$ used for imaging, the third one by the structure of the specimen. With energies referred to the Fermi energy the kinetic energy of the photoelectron is then with the work function Φ

$$E_{\text{kin}} = \hbar\omega - \Phi - E_{\text{B}}. \quad (2.17)$$

The binding or ionization energy is defined by the energy difference of the *total* N -electron system before and after ionization of the selected core level:

$$E_{\text{B}} = E_{\text{tot}}(N - 1) - E_{\text{tot}}(N). \quad (2.18)$$

Core level ionization is a localized process in an extended, usually crystalline environment. The calculation of $E_{\text{tot}}(N - 1)$ and $E_{\text{tot}}(N)$ is usually done by imbedding the atom/ion in which the hole is created and its immediate neighbors (ligands) into the environment represented by an effective crystal field simulated by point charges, as illustrated by calculations of the p-shell ionization of MnO [76]. The other approach is to start from the crystalline environment by calculating the crystal potential of an infinite crystal with one of the state of the art computational methods such as the density functional theory and deriving from it a set of Wannier functions localized at the central atom and its ligands. This method has recently also been applied to MnO and other oxides [77]. Both methods are called multiplet ligand-field theories but differ in the representation of the localized state and its environment. The calculations are quite elaborate and have not only to take exchange, correlation, and spin-orbit coupling of the two states into account but also the relaxation processes following the hole creation in the core level, which may be divided roughly into local (intra- and interatomic) and collective processes or—in XPS jargon—into shake-up and shake-down processes. The local relaxation involves cascading processes, in which an electron with lower binding energy fills the hole, thus creating another hole to be filled again. These electrons do not have to come from the atom with the original hole but also from a neighbor atom. As a result a number of electron configurations with different total energies are formed in the final state, giving rise to the multiplet structure in the photoelectron spectrum, which is usually described by atomic quantum numbers. In as much as in this relaxation process also the most weakly bound valence electrons are involved, there is also a collective response to the hole creation, which is particularly evident in 3d transition metals and their compounds. Interestingly the relaxation processes can not only involve transitions to more strongly bound states but also to unoccupied higher energy level states, with the energy increase compensated by parallel transitions to more strongly bound states. An example is the so-called frustrated Auger configuration process [78], in which an electron is promoted into an unoccupied 4f state.

Although serious efforts started already 40 years ago [79], the calculation of the multiplet structure is still an active field of research and the advantages and accuracy of different approaches are still a matter of discussion [80, 81]. Relative intensities and electron configuration assignments may well change with further improvements of the models and methods used in these calculations so

that we will not dwell further on this subject but refer to reviews of this subject [82, 83]. The most important aspect of these calculations for spectroscopy in PEEM is the chemical shift caused by the bonding to the ligands and the relaxations in the emission process, which is used for identifying the bonding state, usually the oxidation state. Due to the complexity of the calculations reliable theoretical data are available only for a limited number of systems so that the experimentalist has to rely in his interpretation on simpler calculations (see e.g., [84]) and on the results of spectroscopic studies of well-defined systems if available.

While multiplet calculations are difficult, experiment has also its problems, which we illustrate now with a few examples of relative simple systems. These problems range from nonconductive specimens to background subtraction and to peak fitting. Charging not only causes peak shifts, which usually can be accounted for by comparison with peaks with known binding energy, but can also cause peak broadening, making correct peak fitting questionable. For background subtraction and peak fitting a number of proven methods are available [85] from which the experimentalist can choose, which puts some uncertainty into the final result [86]. Furthermore experimental conditions such as energy, energy width, polarization, angle of incidence of the X-rays, emission direction of the electrons (“take-off angle”), energy resolution of the analyzer and other factors have a strong influence. Figure 2.16a–f [87–91] illustrates some of these problems. Except for (c) and (d) the spectra are taken with Al $K\alpha$ radiation with high-resolution spectrometers. They show the S 2p peak in different environments taken with different experimental conditions. In all cases the dominating features can be fitted with the spin–orbit split S $p_{3/2}$ and $p_{1/2}$ doublet with 1.20 eV spacing and 2:1 intensity ratio as expected from theory. However, there are significant differences in the peak shapes between (a) and (b) which are from UHV-cleaved sphalerite ($Zn_{1-x}Fe_xS$) surfaces, and between (d), (e) and (f) which are from UHV-cleaved pyrrhotite (Fe_7S_8 , $Fe_{10}S_{11}$) surfaces. The difference between spectrum (a) with $x = 0$ [87] and (b) with $x = 0.25$ [88] cannot be explained by differences in take-off angle ($\theta = 45^\circ$ in a), 90° (open symbols), and 20° (full symbols) in (b) nor by different instrument resolution. The difference in x should rather have the opposite effect because of the more complex environment of S in (b). A possible cause for the broader peak in (a) is charging [88]. The difference between 90° and 20° take-off angle in (b) is attributed to the larger contribution of S surface atoms with slightly different bonding. Charging-induced peak broadening may also be responsible for the difference between the spectra (e) [90] and (f) [91], taken under very similar conditions (electron kinetic energy 1325 eV), but the large width of spectrum (d) [90] clearly has a different reason. It was taken with 210 eV synchrotron radiation light so that the spectrum is very surface-sensitive because of the low energy (48 eV) of the photoelectrons. As a consequence, a strong surface peak doublet with lower binding energy is needed for fitting the spectrum. A high binding energy peak doublet is needed in the spectra (d), (e), and (f), connected with different bonding sites in the bulk of these materials. The complication of the separation of volume and surface contributions does not exist of course in adsorbed

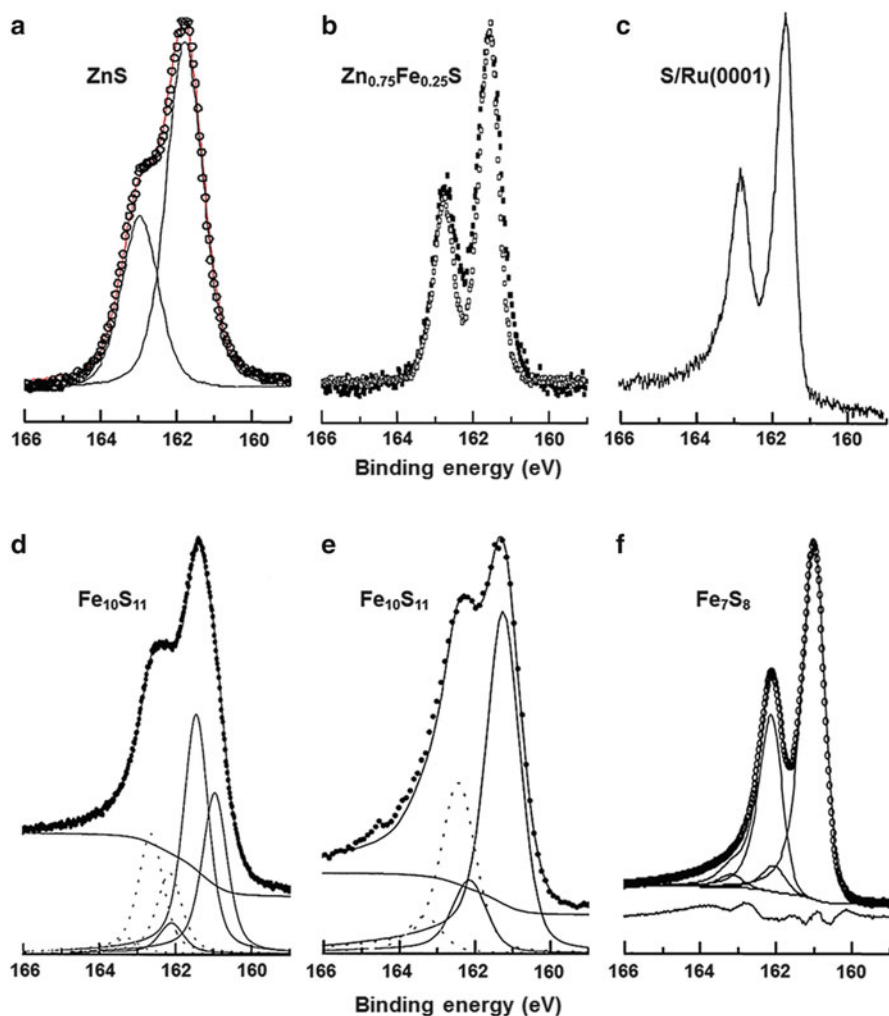


Fig. 2.16 Sulfur 2p X-ray photoelectron spectra in different environment and taken under different experimental conditions illustrating the influence of type of X-ray source, take-off angle, surface condition, and possibly charging. For explanation see text. (a) Reproduced from Ref. [87] by permission of The Electrochemical Society. (b) Reproduced with permission from Ref. [88]. Copyright 2007 Elsevier. (c) Reproduced with permission from Ref. [89]. Copyright 1998 Elsevier. (d, e) Reproduced from Ref. [90] with permission from Mineralogical Society of America. (f) Reproduced with permission from Ref. [91]. Copyright 2004 Elsevier

layers as indicated in spectrum (c) from 0.2 monolayers of S on Ru(0001) obtained with 260 eV photons [89].

The XPS spectra of monatomic materials seem at first sight simpler to analyze. That this is not so in general is illustrated with Fig. 2.17a–c [92–94] for the Fe 3p spectrum. Here we have in addition to the spin–orbit coupling and the relaxation

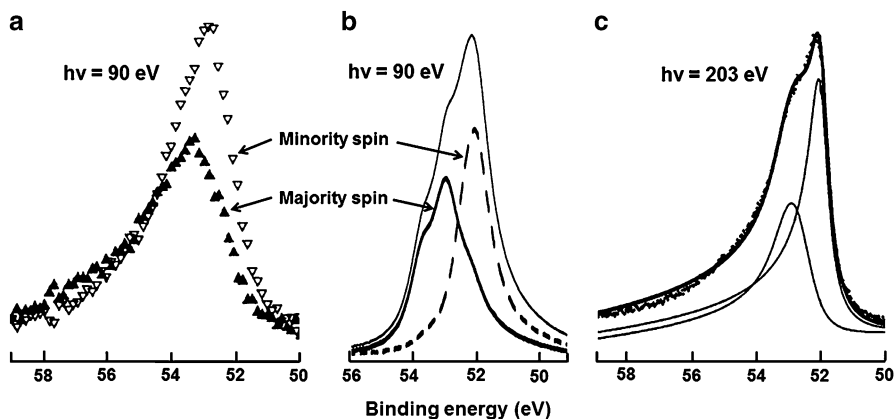


Fig. 2.17 Fe 3p XPS spectra. (a) Experimental spin-resolved spectrum [92], (b) Theoretical spin-resolved spectrum [93], (c) spin-averaged spectrum [94]. For explanation see text. (a) Reprinted with permission from Ref. [92]. Copyright 1990 by the American Physical Society. (b) Reprinted with permission from Ref. [93]. Copyright 1994 by the American Physical Society. (c) Reproduced from Ref. [94] with permission from The American Chemical Society, © 2008

effects also exchange effects. Spin-resolved XPS [92, 95, 96] has shown that the spin-up and spin-down peaks are shifted by about 0.5 eV (Fig. 2.17a [92]). The relative height of the peaks was found to depend upon the direction and polarization of the incident light with respect to the magnetization direction (magnetic dichroism) [97, 98] in agreement with theory [93]. Additional studies as a function of the magnetic field direction [99–102] revealed the complexity of the nature of the Fe 3p peak, for example its dependence upon energy, type of polarization (linear, circular) of the photons [102] and allowed to separate spin–orbit and exchange splitting contributions to the peak shape (0.67 and 0.41 eV). The spin-averaged spectrum (Fig. 2.17c) [94] is in approximate agreement with that shown in Fig. 2.17b [93], calculated for a specific combination of direction, polarization, and magnetization [93] but other peak shapes have been reported too. The 3p spectra of Co [99] and Ni [103] are of similar complexity. In materials with larger spin–orbit splitting, in which the peaks of the various multiplet configurations are separated better and which have been studied in far more detail, such as oxides and halides with well-defined oxidation states, multiplet analysis allows to determine the composition. However, as soon several oxidation states are present simultaneously or resolution and signal to noise ratio is limited, for example by the size of the features of interest, compositional analysis becomes elusive, with few exceptions such as the well-studied Si–O system. We will discuss such a difficult system in Chap. 6.5, where the nature of the features of interest, submicron crystals formed by reaction with the substrate, finally had to be determined by μ -LEED.

Despite of these limitations XPS is a valuable complement to the various imaging methods discussed in this book because it gives information on the atomic species present. XPEEM generally works with synchrotron radiation sources and is

rarely used with the traditional Al or Mg $K\alpha$ radiation, for two reasons: the photoelectrons produced by the traditional sources probe mainly the bulk and the intensity of even the most powerful X-ray sources is too low for imaging at magnifications of interest. Therefore, the quantification methods developed in the past for relative atomic composition determination are of limited value, in particular for small three-dimensional features. However, at least qualitative information can be obtained from binding energy and peak height in the spectrum. There are many tables of binding energies. The one generally used in XPEEM can be found in the X-ray data booklet of the Advanced Light Source [104, 105]. In contrast to definition (Eq. (2.17)) the binding energies of semiconducting elements are defined with respect to the top of the valence band, those of elements, which are gaseous at room temperature, with respect to the vacuum level. Of course, in compounds the chemical shifts, discussed above have to be taken into account, which rarely poses a problem because the binding energies of the elements differ sufficiently.

The XPS peak intensities characterized either by peak height or by area below the peak, are determined by a number of factors. First of all they depend on the initial ionization process and the process, which fills the hole created in the ionization. The first process is characterized by the ionization cross section, the second by the Auger yield. The ionization cross section depends upon the photon energy as illustrated for the core levels of Au in the upper part of Fig. 2.18 [106]. The Auger yield is the fraction of the ionization events, in which the system does not relax via fluorescence radiation but by ejecting a photoelectron and filling the hole via Auger electron processes. It depends upon nuclear charge as shown in the lower part of Fig. 2.18 [107] for different electron shells. In the energy range of interest in XPEEM there are always shells available for which the Auger yield is practically 1, so that all ionization processes lead to photoelectron emission. From the upper part of Fig. 2.18 the great advantage of synchrotron radiation becomes evident: by choosing the photon energy the ionization cross section can be maximized or the photoelectron energy can be selected for optimum surface sensitivity via the energy-dependent attenuation of the photoelectron current during its way to the surface.

The attenuation is caused foremost by inelastic scattering but elastic scattering also contribute to it. It is characterized by a number of quantities with the acronyms IMFP, TMFP, EAL, MED, and ID, which stand for inelastic mean free path, transport mean free path, effective attenuation length, mean escape depth, and information depth [108]. Other names such as electron sampling depth or probing depth are used too. All of them describe in one way or other the information depth of surface analytical methods and are frequently used interchangeably. A rough value for the IMFP can be extracted from the frequently used universal curve but there are many more accurate calculations and compilations of which only the most recent ones are cited here [108–113]. In particular Tanuma et al. [112] give an extensive list of IMFP values for many materials and electron energies from about 50 to 30000 eV. However care has to be taken when using them in XPS data interpretation. For example, Nakajima et al. [114] have measured the increase of the L edge signal of Fe, Co, and Ni as a function of thickness and deduced from it

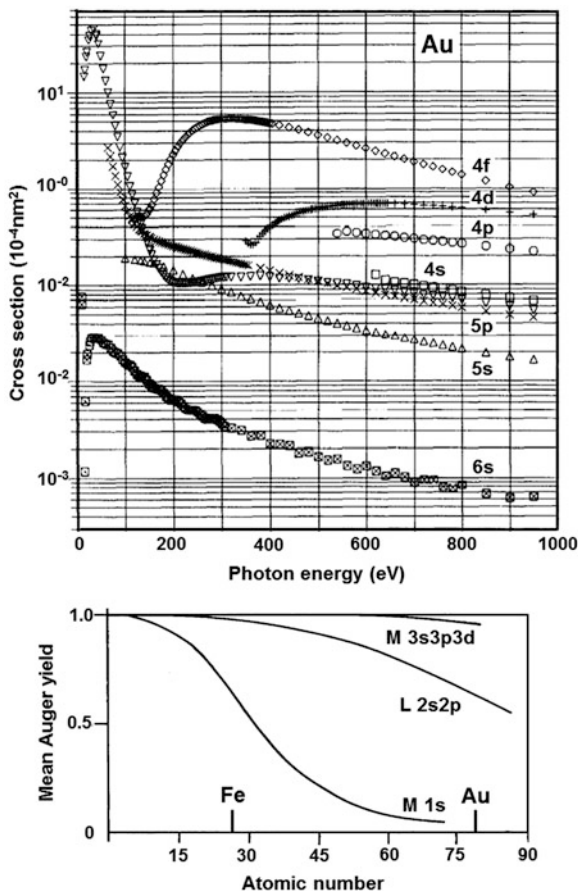


Fig. 2.18 *Top*: Atomic subshell photoionization cross sections of Au as a function of photon energy [106]. *Bottom*: Mean Auger electron yield Y_A for some subshells as a function of atomic number [107]. Y_A is a measure for the filling of the holes created by photoionization by electron emission instead of X-ray radiation. For example $Y_A \approx 1$ for the Au 4f and the Fe 3p shells, which are frequently used in PEEM, indicating that in the energy range of interest in PEEM nearly all holes in free atoms are filled by electron emission. *Top*: Reproduced from Ref. [106] with permission. Copyright 1985 Elsevier. *Bottom*: Reproduced from Ref. [107] by permission of Taylor and Francis Group, LLC

electron escape depths of 17 ± 2 , 25 ± 3 and 25 ± 3 Å at the edge energies 707, 778, and 853 eV, respectively. In contrast, the most recent tabulated IMFP values for the same energies in these metals are 13.0, 12.1, and 13.3 Å, respectively [112]. Similar differences between IMFP values and mean probing depth values λ_p ($1/e$ -values) were found in studies of the attenuation of photoelectrons of various energies E in Cr films as a function of thickness [115]. For $E = 101, 464, 707$ and 929 eV $\lambda_p = 9.8, 15.6, 25.5$, and 47 Å, while the corresponding IMFP values are 4.4, 9.5, 12.9, and 15.4 Å [112]. Thus, the values differ by as much as a factor of 3.

These last experimental data are of particular relevance for XPEEM because they were measured in a PEEM instrument with an angle-limiting aperture as used for imaging and show that caution is in place when using IMFP data in XPEEM.

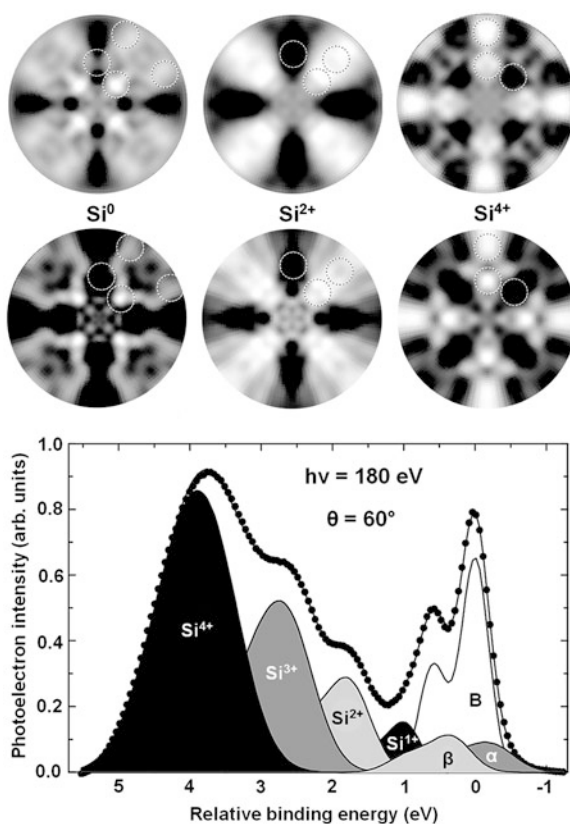
Up to now we have considered only the influence of the attenuation of the *electrons* on the information depth. When X-ray absorption is strong as it is at the absorption edges then also the finite penetration depth of the *X-ray* beam can influence the sampling depth, leading to signal saturation before electron attenuation limits the signal. This is of particular importance at large angles of incidence of the photon beam as for example at 74° in one of the commercial instruments and has to be taken into account in thick films or bulk crystals. This saturation effect is discussed in Ref. [114] in connection with XAS measurements.

The influence of elastic scattering on the effective attenuation length (EAL) mentioned above is taken into account by assuming isotropic scattering. This is an acceptable approximation in disordered or fine-crystalline materials with random crystal orientation. Many specimens are, however, single crystals or epitaxial layers and then this assumption is invalid. Elastic scattering of the photoelectron wave, which to a first approximation may be considered as a spherical wave at its origin, produces then a photoelectron diffraction pattern similar to what has been mentioned already in Sect. 2.3.3. The amplitude of a spherical wave decreases like $1/r$ with distance r so that the immediate neighbors of the source atom scatter back most strongly, creating an interference pattern characteristic for the local atomic configuration. Examples of such X-ray photoelectron diffraction (XPD) patterns are shown in Fig. 2.19 together with the XPS spectrum of an oxidized Si(111) surface from which they were taken [116]. The spectrum clearly shows the chemical shift between the different oxidation states. The XPD patterns taken at their peak energies allow by comparison with multiple scattering calculations for model SiO_x clusters determination of the bonding distances and angles in them. For a recent review of XPD experiments see Ref. [117], for a review of the theory of XPD and other diffraction processes see Ref. [118], for software packages for the analysis of X-ray multiple scattering patterns see Ref. [119]. With increasing energy the scattering occurs increasingly in the forward direction, which allows considerable simplifications in the analysis [120]. In PEEM, high-energy XPD is limited by the limited angular transmission of the objective lens. However at lower energies it can be quite useful. For example much of the XPD pattern shown in Fig. 2.19 can be observed in a PEEM instrument in the diffractive plane much faster than with most spectrometers. Alternately local variations of the oxidation states can be imaged by inserting the contrast aperture in regions, in which the intensity differs strongly between different oxidation states.

2.2.6.2 Secondary Electron Emission

The intensity of slow secondary electrons with kinetic energies from zero to several eV is orders of magnitude higher than that of most photoelectrons and, therefore, particularly well-suited for imaging, except for its wide energy distribution, which

Fig. 2.19 X-Ray photoelectron diffraction patterns (XPD, *top*) and XPS spectrum (*bottom*) of an oxidized Si(100) surface. The *top* row shows the experimental XPD patterns taken at the energies of the maxima of the Si^0 (B), Si^{2+} , and Si^{4+} states of Si shown in the spectrum, the *second* row the XPD patterns simulated with multiple-scattering calculations. Adapted with permission from Ref. [116]. Copyright 2004 by the American Physical Society



is detrimental to resolution, even with energy filtering because of the large $\Delta E/E$ ratio. Nevertheless imaging with secondary electrons is the most widely used imaging mode because of its wide application range. In contrast to the electron *emission* process discussed in the previous section, this mode makes use of the secondary products of the X-ray *absorption* process. While previously the photon energy was fixed and the energy of the photoelectrons was scanned, now the photon energy is scanned and the electron energy is fixed. The various imaging modes are described by the prefixes XANES or NEXAFS, XMCD, XMLD and XNLD added to PEEM. XANES stands for X-ray absorption near edge structure, NEXAFS for near edge X-ray absorption fine structure, XMCD for X-ray magnetic circular dichroism, XMLD for X-ray magnetic linear dichroism and XNLD for X-ray natural magnetic dichroism. It is usual not to take a series of images as a function of photon energy but first to take a spectrum—or two in the case of XMCD and XMLD—and select the energy of interest for imaging. The spectra are the subject of this section.

Because of its importance for the spatial resolution in XPEEM we have to take a look at the secondary electron distribution produced by X-rays. Henke et al. have

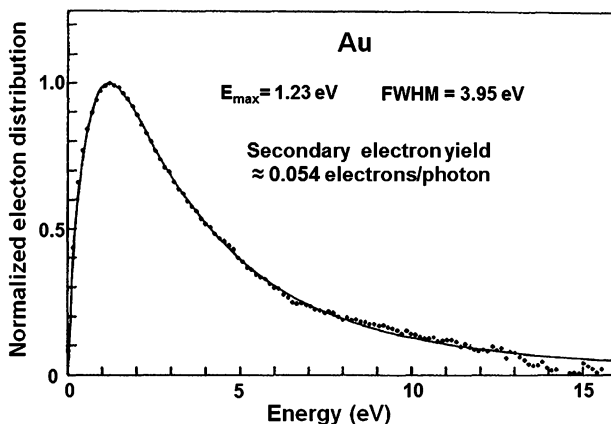


Fig. 2.20 Energy distribution of secondary electron from an evaporated Au film excited by Al K α radiation (1487 eV) at normal incidence. Reprinted with permission from Ref. [122]. Copyright 1979 by the American Physical Society

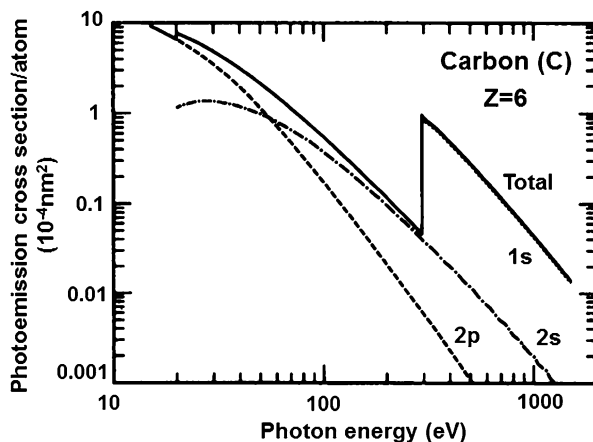
studied the low energy region of the electron distribution theoretically and experimentally for polycrystalline Au and Al [121] and for a number of metals, semiconductors, and compounds [122] using Al K α radiation. Figure 2.20 shows the secondary electron distribution of Au [122]. For metals and narrow band gap materials good approximations are

$$I_s(E) \sim \frac{E}{(E + \Phi)^n}, \quad (2.19)$$

with $n = 4$ for metals [121] and $n = 3$ for narrow band gap materials [122]. Here Φ is a fit parameter, which can be approximated by the work function Φ and the electron affinity χ , respectively. The distributions have maxima at $\Phi/3$ and $\chi/2$ and full widths at half maximum of 1.10Φ and 1.90χ , respectively. Unfortunately the secondary signal is still high up to several ten eV. This is an impediment to spectroscopy and imaging with low energy photoelectrons because they are superimposed on the strong secondary electron background from which they are increasingly more difficult to separate with decreasing energy.

With this background in mind we can now address the first XAS mode, NEXAFS, or XANES. These two acronyms stand for the same type of spectroscopy, the determination of chemical bonding via the bonding-specific ionization energies of different species, using the secondary electrons produced by the photoelectrons and Auger electron cascade in the filling of the hole created in the ionization process. With linear and circular polarized light in addition the orientation and chirality of adsorbed species can be obtained. The different bonding states produce partially overlapping absorption peaks, from which bonding distances and bond angles can be extracted by comparison with theoretical models. There is an excellent book on this subject [123] so that we will concentrate here only on the

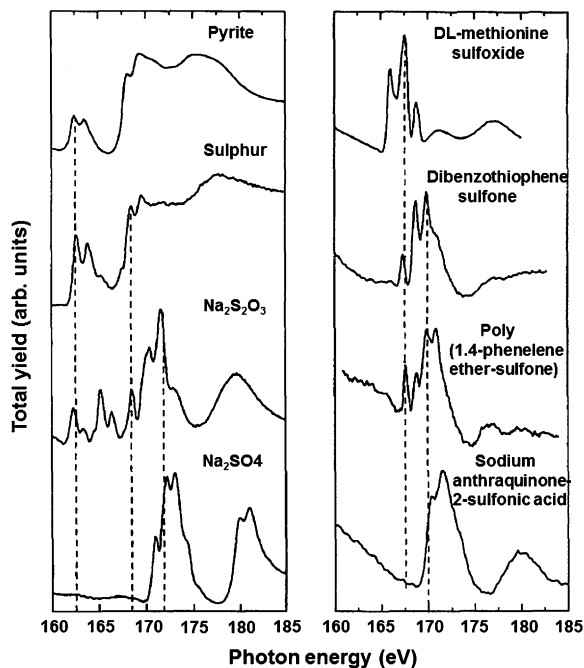
Fig. 2.21 Atomic photoionization cross section of carbon, showing the K absorption edge. Reproduced from Ref. [104] with permission



aspects important for PEEM. An example of a photoionization cross section is shown in Fig. 2.21 for atomic C [104, 105]. At the K absorption edge (277 eV), where most of the XANES imaging of C-containing materials is done, the cross section is two orders of magnitude higher than at the Al K α energy, another advantage of synchrotron radiation compared to conventional X-ray sources. Furthermore, the cross section jumps by a factor of 20 at the K edge so that chemical shifts can be measured with high signal/noise ratio. One problem frequently encountered is C-contamination of the mirrors in the synchrotron radiation beamline, which can produce a significant background in the XAS spectrum. In imaging this is less critical than in spectroscopy, because it produces only a location-independent background. However it reduces the contrast from local variations of the bonding such as in copolymers (see Chap. 6.3). Keeping the decrease of the ionization cross section with photon energy in mind, useful absorption edges for imaging are the K edges up to F and the L edges up to Ni. As an example, the sulfur L edge XAS spectra in Fig. 2.22 illustrate the sensitivity of this method to the chemical bonding, which is discussed in Ref. [124]. It should be noted that the ionization cross sections in Refs. [104, 105] and plotted in Fig. 2.18 are for free atoms with energies referred to the vacuum level. With correction for the binding energy difference between free atoms and atoms in condensed matter these data are, however an excellent criterion for the selection of the core level and photon energy. Another useful criterion for imaging with secondary electrons is the mass absorption coefficients for X-rays, which takes the atomic density in condensed matter into account [125–127].

It is useful to compare XANES with XPS. XANES measures the intensity of all slow secondary electrons, not only those produced at the selected absorption edge but also by ionization of states with lower binding energy. On the other hand the energy filter, which selects the desired photoelectrons transmits only a small fraction of the always present secondary background, resulting in a much better atom-specific signal-to-noise background ratio. The IMFP of the secondaries is

Fig. 2.22 X-Ray absorption near edge structure (XANES) at the L edge of elemental sulfur and sulfur-containing compounds, illustrating the high sensitivity of XANES to the chemical environment of the selected atom. Reproduced with permission from Ref. [124]. Copyright 1996 Elsevier



generally large compared to that of photoelectrons, in particular if the photon energy is chosen in such a manner that the photoelectrons have an energy, at which their IMFP is small. This makes photoelectron imaging more surface sensitive than XAS imaging. Of course there are also other considerations, which determine the selection of the method such as the much higher intensity of secondary electrons and the absence of the energy filter needed for XPS in many PEEM instruments, the latter leaving no choice.

While XANES is the method for chemical surface characterization in PEEM instruments without energy filter, XMCD is the workhorse for atom-specific magnetic characterization of ferromagnetic materials. Again, there is an excellent book covering this subject [128] so that we will limit the discussion here only to a brief discussion of the basic aspects of XMCD and to aspects important for XMCD imaging. Circular polarized light has angular momentum as demonstrated experimentally already 1936 [129]. In the wave picture (Maxwell's equations) this is surprising but can be derived with some effort [130, 131]. In brief, an electromagnetic wave with the energy density $\epsilon_0 E^2$ has an angular momentum $L = \epsilon_0 E^2 (|\psi_R|^2 - |\psi_L|^2) / \omega$ in direction of the propagation vector of the wave, where ψ_R and ψ_L are the amplitudes of right hand and left hand polarized waves and ω is the angular frequency. According to the correspondence principle the classical energy density $\epsilon_0 E^2$ of the wave corresponds in the particle picture the energy density $n\hbar\omega$ of n photons with energy $\hbar\omega$. Comparison with the classical expression for L shows immediately that the angular momentum of the photon

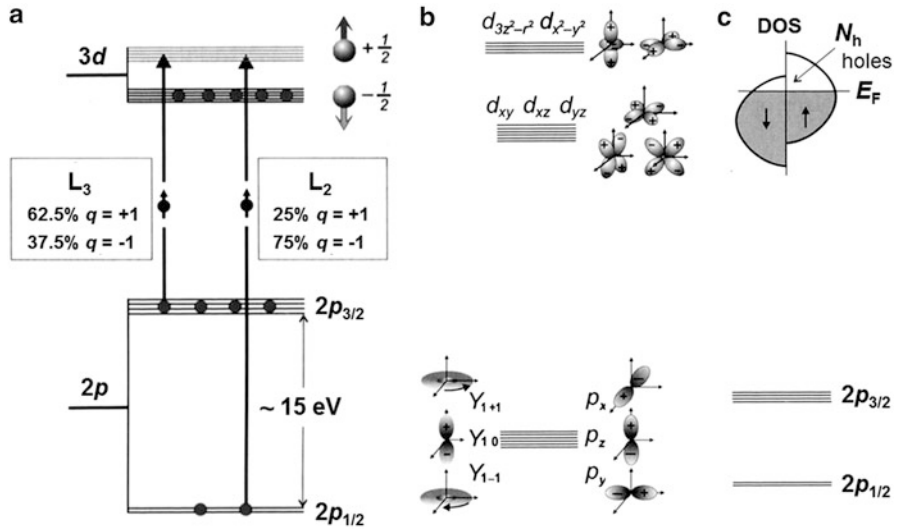


Fig. 2.23 Model of the transition processes leading to X-ray magnetic circular dichroism. (a) atomic model, (b) ligand field model, (c) band structure model. Not to scale. The energy distances between core and valence states are shown much smaller than the splitting of the 2p and 3d states. The *insets* in (a) are the relative transition probabilities as calculated in the ligand field model. Adapted from Ref. [128] with permission from Springer Science + Business Media

is $I = \hbar (|\psi_R|^2 - |\psi_L|^2)$. For right (left) hand polarized light the second (first) term is zero and the other one 1 so that $|I| = l_z = \pm \hbar$ or in the usual atomic angular momentum units (\hbar) $l_z = \pm 1$. This angular momentum is a spin angular momentum and we will call it from now on therefore s_p . From the particle point of view this is immediately obvious: photons are bosons and bosons have angular momentum of magnitude \hbar . This quantum number has to be taken into account in the absorption process, i.e., in the transition from the initial core state to the final unoccupied state.

XMCD is studied in PEEM by imaging with secondary electrons, which are created during the relaxation cascade from the nonequilibrium state produced in the excitation of core electrons by circular polarized light. The nonequilibrium states are the spin-split 3d and 4f states of ferromagnetic and antiferromagnetic materials just above the Fermi level, the corresponding core electrons are the 2p and 3d electrons ($L_{2,3}$ and $M_{4,5}$ states). As an example we consider a cubic 3d metal, first an isolated atom, then an atom surrounded by six atoms as in a cubic crystal (octahedral site) and finally an “atom” in a periodic crystal. Figure 2.23a [128] shows schematically the energy level structure of an isolated 3d metal atom with five electrons in the d band. The 2p levels are split by spin–orbit interaction into $2p_{1/2}$ (L_2) and $2p_{3/2}$ (L_3) levels, the 3d levels by exchange interaction into spin-down and spin-up level groups, each of which contains 5d orbitals. Only the spin-down levels are occupied according to Hund’s rule. When the atom interacts with neighboring atoms, which create a so-called ligand field (“crystal field”), the sequence of the energy levels is rearranged into two level groups, e_g and t_{2g} , which contain the d

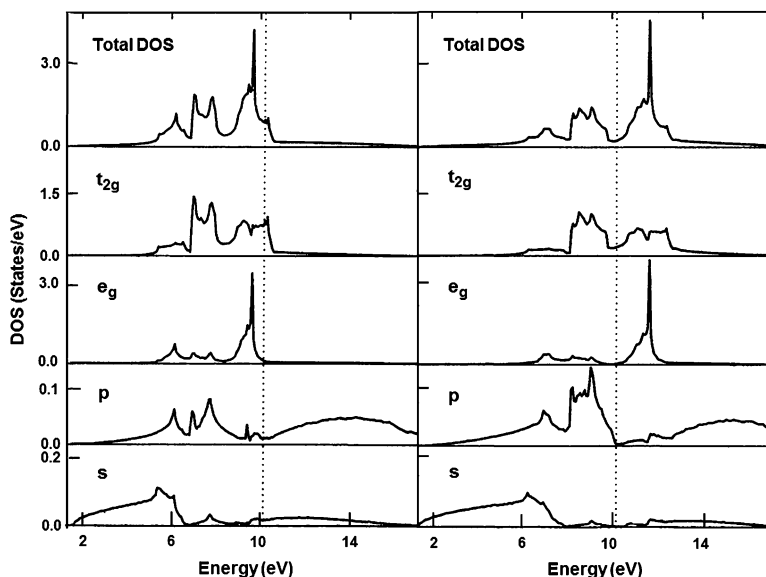


Fig. 2.24 Angular momentum-resolved and total density of states of Fe. *Left*: spin down states, *right*: spin up states. There is also a significant spin polarization in the p states although it contributes little to the total spin imbalance, which is dominated by the e_g and t_{2g} states. From Ref. [132] with permission from Springer Science + Business Media

orbitals shown in Fig. 2.23b [128]. A further redistribution occurs when the electrons become delocalized in the periodic lattice of the crystal and form majority and minority spin bands as indicated by the schematic density of states (DOS) in Fig. 2.23c [128]. The true density of states as obtained from band structure calculations for Fe, for example, shows that e_g and t_{2g} levels are no longer separated (Fig. 2.24 [132]). They both have regions above the Fermi level into which electrons from 2p levels can be excited with near-threshold radiation. The relative transition probabilities into the unoccupied d states upon right hand ($q = +1$) and left hand ($q = -1$) radiation excitation determines the probability of secondary electron emission. They can be calculated to a first approximation in the ligand field model, which gives the results shown in Fig. 2.23a by their percentages. The XMCD signal is the difference between the secondary electron emission current produced by right and left circular polarized light, which is 50 % for excitation from the L_2 state and 25 % from the L_3 state. However the L_3 state has twice the number of electrons than the L_2 state so that the XMCD signal resulting from the excitation of the two states has the same magnitude but opposite sign. Electron delocalization in the crystal modifies the relative magnitude of the two signals but the ligand field theory model gives a first good approximation to the mechanism of XMCD. It explains qualitatively the experimental absorption and XMCD spectra shown in Fig. 2.25a [128], whose quantitative description requires more sophisticated calculations as described in Ref. [128].

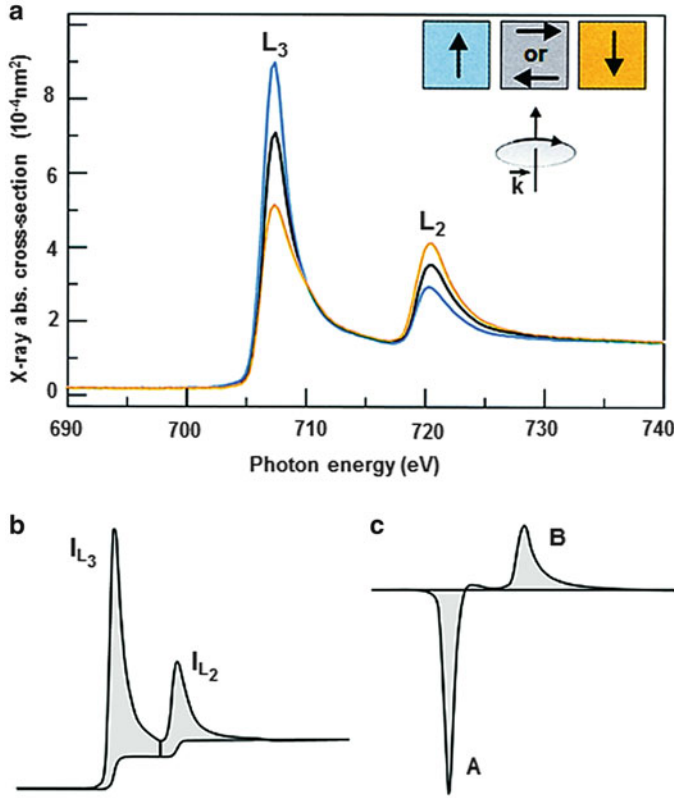


Fig. 2.25 X-Ray absorption spectrum (XAS) at the Fe $L_{2,3}$ edge (secondary electron yield) of circular polarized light (a). The directions of the angular momentum L of the photon ($L \parallel \pm \mathbf{k}$) and of the magnetization M are indicated by *arrows*. As seen in Fig. 2.23 the transition probability from the L_3 level to the levels above the Fermi level is higher when $L \parallel M$ than when $L \parallel -M$, while for the L_2 level the opposite is the case (not shown). The difference between the two spectra are the XMCD signals (b) and (c). Their magnitude is proportional to the magnetic moment of the absorbing atom in its environment and thus a measure for the magnetization. As described in the text from the areas below the peaks the number of empty d states and the orbital and spin magnetic moments can be extracted after proper background correction, which takes into account energy losses (smoothed step function seen in (b)). Adapted from Ref. [128] with permission from Springer Science + Business Media

Figure 2.25a shows that the photon spin direction has to be (anti)parallel with the spin direction of the electron for the level selection of the final state. The magnetic dichroism is defined by convention as the intensity difference between the two spectra $\Delta I = I_{\downarrow\downarrow} - I_{\uparrow\uparrow} \equiv I_{\text{XMCD}}$ and is directly proportional to the atomic magnetic moment. Frequently the angular momentum of the photon s_p is not parallel to that of the magnetic moment m connected with the angular momentum of the 3d shell and the circular polarization P of the photon beam is not 100 %. Then

$$I_{\text{XMCD}} = P s_p \cdot m = L_p \cdot m = L_p m \cos \theta, \quad (2.20)$$

where θ is the angle between the direction of the incident beam and the local magnetization direction. The polar angle of incidence is fixed in all PEEM instruments and in most of them also the azimuthal angle unless the instrument is equipped with a rotatable specimen manipulator. Therefore in XMCDPEEM usually only the component of \mathbf{m} in the direction of the incident light is measured.

The spectra in Fig. 2.25a contain not only information about the atomic moment but also about the total number of unoccupied states N_h in the 3d band and allows separation of the orbital magnetic moment m_O from the spin magnetic moment m_S . For this it is in principle necessary to saturate the specimen magnetically in the direction of the incident beam and to average over all directions, that is to make three measurements in three orthogonal directions. In XMCDPEEM these conditions are not fulfilled so that only approximate values can be obtained. These are nevertheless frequently close to the values determined with averaging measurements, with which they agree when the specimen is polycrystalline and magnetically not aligned because the averaging is done by the specimen. The information about N_h , m_S , and m_O is obtained from the shaded areas in Fig. 2.25b, c [128]. The first one shows the sum $I_{\uparrow\downarrow} + I_{\uparrow\uparrow}$ of the spectra taken with opposite helicity light, from which the transitions from the 2p level to the unoccupied 4s states have been subtracted so that only the holes in the 3d band contribute to the signal. The 3d contribution to the L_3 peak is twice as large as that to the L_2 peak because of the higher transition probability from the $2p_{3/2}$ level compared to the $2p_{1/2}$ level. Figure 2.25c shows the difference $I_{\uparrow\downarrow} - I_{\uparrow\uparrow}$, that is the XMCD spectrum. The symbols I_{L3} , I_{L2} , A , and B are the areas under the peaks. The sum rules then state that

$$N_h = I_{L3} + I_{L2}/C \quad m_S = \mu_B - A + 2B/C \quad m_O = -2\mu_B A + B/3C \quad (2.21)$$

where the brackets indicate the average mentioned and C is about 10 for Fe [128]. Frequently only the ratio m_O/m_S is determined, thus eliminating C . For a deeper insight in the use of XMCD for the determination of m_S , m_O , and the magnetic anisotropy energy from angular-dependent measurements of m_O see Ref. [133], for the influence of saturation effects see Ref. [134].

Two notes in passing: (1) in the literature the arrow in the majority band frequently is shown pointing upward and the band is correspondingly called spin-upband in contrast to the direction shown here, which follows from the atomic model. What is really meant with the direction of the arrow in this other description is the magnetic moment \mathbf{m} whose sign is opposite to the spin. (2) The high peaks at the absorption edges, in particular the L_3 peak, which are a consequence of the high density of 3d states at the Fermi edge, are frequently called white lines for historical reasons when spectra were recorded on photo plates.

Summarizing these qualitative considerations, XMCD gives atom-specific information on the magnitude and direction of the average magnetic moment and allows with some limitations separation into orbital and spin magnetic moment. Details can be found in Refs. [83, 128, 133] and in many other books and reviews, too numerous to be listed here.

X-Ray linear dichroism (XLD) is not only important for magnetic studies as X-ray magnetic linear dichroism (XMLD) but also for nonmagnetic studies as X-ray natural magnetic dichroism (XNLD). XLD occurs whenever the charge distribution around the absorbing atom is nonspherical so that the absorption depends upon the angle of the \mathbf{E} vector of the *linear* polarized wave with respect to the direction of the charge distortion. Thus whenever the specimen has directional bonds, which are well aligned over the region measured, XNLD is present, independent whether the specimen is nonmagnetic, ferromagnetic, or antiferromagnetic. In the second two cases it may be induced by symmetry reduction of a spherical charge distribution by magnetization along a certain axis. This effect is most pronounced when the 3d electrons are strongly correlated and the 3d levels are split by crystal field and spin-orbit interactions. Many antiferromagnetic oxides containing 3d transition metal ions with nonsymmetric charge distribution are systems of this type such as NiO, which has been the subject of many studies and discussion. Cubic crystals have several easy magnetic axes, which leads to multidomain formation unless some anisotropy is induced, for example by strain. Here XMLDPEEM is very useful for the understanding of the antiferromagnetic structure [135]. The XMLD can be separated from the XNLD either by measurements at the $L_{2,3}$ edge above the Néel temperature or via the O 2p orbital anisotropy at the O K edge. The calculations needed for the interpretation of the spectra are equally as or more demanding than those for XMCD spectra. Their principles and references to them can be found in Ref. [128]. Here we consider only briefly the essentials needed for XLDPEEM.

As already mentioned at the beginning, for XLD to occur \mathbf{E} must be parallel to direction of the oriented bonds in molecules, to the distortion in nonmagnetic crystals or to an easy magnetic axis in a ferromagnet or antiferromagnet, which we summarize under the term symmetry axis. The transition probability is proportional to the number of unoccupied bonding states in the direction of \mathbf{E} (“search light” effect). The XLD signal is then obtained from two measurements one parallel to the symmetry axis, the other perpendicular to it: $I_{\text{XLD}} = I_{\parallel} - I_{\perp}$. When the symmetry axis has more than twofold rotational symmetry then the angular dependence of the intensity can be written as

$$I(\theta) = I_{\parallel} \cos^2 \theta + I_{\perp} \sin^2 \theta \quad \text{or} \quad I(\theta) = I_0 - (1/\sqrt{2})(3 \cos^2 \theta - 1)I_2. \quad (2.22)$$

Here θ is the angle with the symmetry axis, I_0 and I_2 are the isotropic and the angular part of the total absorption cross section, respectively. In the case of a ferromagnetic specimen the XMLD intensity can be expressed as

$$I_{\text{XMLD}} \sim P |\mathbf{m} \cdot \mathbf{E}|^2 \sim P m^2 \cos^2 \theta, \quad (2.23)$$

where P is the degree of linear polarization and two measurements with \mathbf{E} parallel and perpendicular to \mathbf{m} are taken. Note the difference between Eqs. (2.20) and (2.23). The choice of the direction of \mathbf{E} is usually limited so that only components of \mathbf{m} can be measured.

For XMLD and XNLD there are sum rules similar to those for XMCD, which are discussed briefly in Ref. [128], where also references to their derivation can be found. The main application field of XNLD is the determination of the orientation of adsorbed molecules, that of XMLD is the study of antiferromagnetic materials and their interfaces with ferromagnetic materials. In ferromagnetic materials the XMLD effect is much weaker than the XMCD effect and, therefore, used much less. For specific studies such as of the magnetocrystalline anisotropy it may be very useful however [136]. Another important application field of XMLD together with XMCD is in multiferroics [137].

2.3 Electron Reflection

2.3.1 *General Considerations*

In this section we will discuss the interaction processes between the incident electron beam and the specimen which are important for image formation in LEEM and SPLEEM. As already mentioned earlier, these processes are not relevant for mirror electron microscopy because in this case the electrons are reflected in front of the surface. The processes involved are elastic, inelastic and thermal diffuse scattering and foremost diffraction, which is dominated by the periodicity of the specimen but also depends on the various scattering processes. Inelastic scattering is not only of interest for energy electron loss spectroscopy (EELS) but also for energy electron loss microscopy. Finally, we also have to consider briefly Auger electron emission, which can be used in the laboratory for spectroscopic Auger electron emission microscopy (AEM), provided that the microscope is equipped not only for spectroscopy but also allows to use different energies in illuminating and imaging beam.

2.3.2 *Elastic Scattering*

In the past LEEM made use of the fact that in crystalline materials the backscattered intensity is concentrated in a few diffracted beams so that images could be acquired with short exposure times. With increasing availability of aberration-corrected instruments, which allow much larger contrast apertures, imaging of materials without long-range order, such as liquids, polymers, or biological materials will become possible. Therefore we consider first backscattering in the absence of long range order. This is also relevant for the understanding of the influence of disordered adsorption layers on crystal surfaces such as two-dimensional gases. As a starting point we consider the scattering of slow electrons by an atom in a completely disordered monatomic material but with the density of its crystalline phase

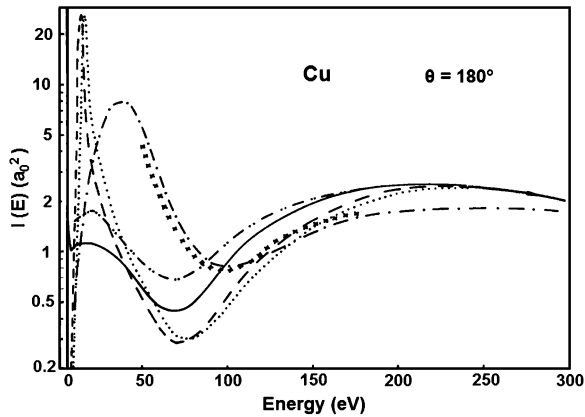


Fig. 2.26 Elastic 180° scattering of Cu atoms as a function of energy calculated for different potentials. The *cross* and *dash-dotted* curves are from free atom potentials, the others from solid state potentials, the best ones being the *dotted* and *dashed* curves, which differ only slightly in the exchange potential used in the atomic potential calculations. The curves from solid state potentials have to be shifted by 13.1 eV to lower energies because their zero is the muffin tin potential. Adapted from Ref. [141] with permission from Springer Science + Business Media

(“radium”), based on calculations which Browne and Bauer made in the early years of the development of LEEM (1964–1967). Their purpose was to ensure that there was enough backscattering at low energies for imaging and to determine the optimum energies for various materials. Except for the initial calculations for free atoms [138] only some of the results were published later [139–146].

The scattering potential is not that of a free atom as used in the calculations of the scattering of fast electrons [147] and of slow electrons sometimes down to 50 eV [148–151]. The reason is simple: the outer part of the potential, which is missing in condensed matter because of the overlap with that of the neighbors, becomes increasingly important with decreasing energy, in particular below 100 eV. This is illustrated in Fig. 2.26 [141] which compares the 180° scattering cross section of Cu atoms for different scattering potentials [140, 141, 146]. The cross sections from the free atom potentials [152, 153] differ significantly from those of the solid state atoms [154], whose overlapping potentials are cut off at some radius forming muffin tin potentials with constant potential between them, called muffin tin zero. The influence of this cut-off is even more pronounced than shown in the figure because the muffin tin zero is 13 eV below the vacuum level, which is used as zero in the figure. Taking this into account shifts the sharp maximum, which is due to a maximum in the $l = 2$ partial wave cross section, to zero. Based on this result and similar ones for other atoms we will consider in the following only scattering from muffin tin potentials used in band structure calculations.

Figure 2.27 [141] compares the backscattering of several atoms into a 30° wide cone around the backward direction [141, 142, 144–146]. Again the curves have to be shifted by the muffin tin zero, which ranges from 12 to 17 eV for these metals, to the left. It is seen that the backscattering of Cu (W) is much weaker than that of

Fig. 2.27 Elastic scattering cross sections of W, Cu, Ag, and Al atoms integrated from 180° to 150° , based on potentials from band structure calculations. The muffin tin zero has to be subtracted in order to reference the energy to the vacuum level. Adapted from Ref. [141] with permission from Springer Science + Business Media

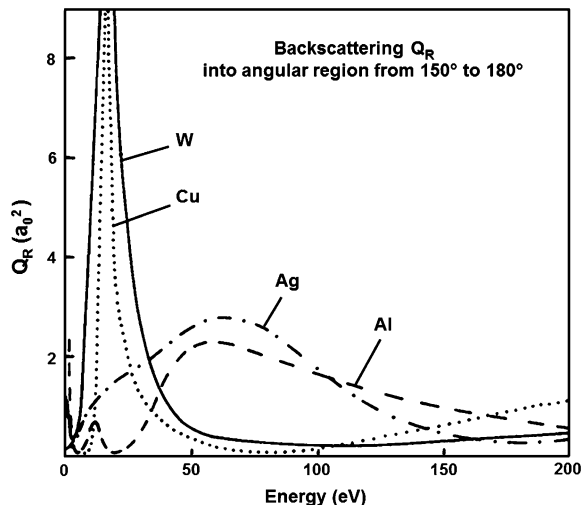
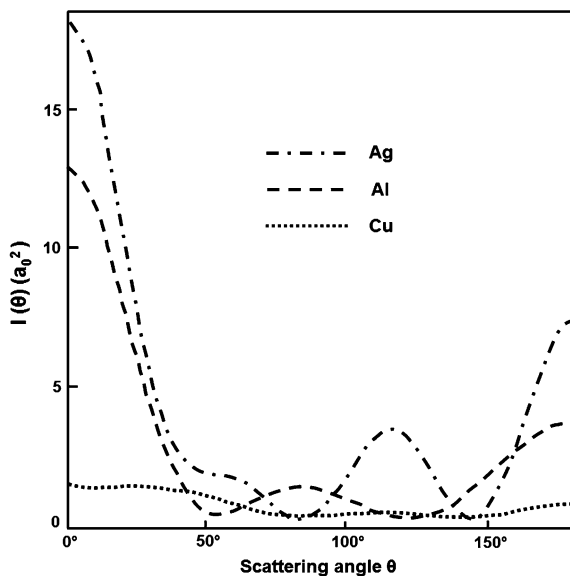


Fig. 2.28 Angular distribution in low energy electron scattering from realistic solid state atomic potentials of Al, Cu, and Ag at 50 eV. Reproduced from Ref. [139] with permission from the American Institute of Physics, © 1970



the lighter atoms Al (Ag) over a wide energy range but that at the lowest energies Cu and W scatter much more than Al and Ag. This example shows that the scattering cross section changes nonmonotonically with nuclear charge Z and energy in contrast to high energy electron scattering so that in LEEM no Z -contrast imaging like in transmission electron microscopy is possible. That the weak scattering of Cu around 50 eV is not limited to backscattering [139, 141, 142, 144] is seen in the angular distribution of the scattering from Cu, Al, and Ag muffin tin potentials in Fig. 2.28 [139]. This is also confirmed by angle-integrated measurements of several

polycrystalline metals, which extend from 2.5 keV down to 60 eV and illustrate that the nonmonotonic behavior extends up to about 1.5 keV [155]. Otherwise there are very few experimental data below 100 eV, which could be compared with theory as the most recent review of elastic backscattering from disordered and polycrystalline surfaces shows [156]. The angular distribution of electrons scattered from liquid Hg was measured only down to 100 eV [157]. Elastic backscattering cross sections of amorphous Si integrated over the angular range of a LEED optics agreed well with calculations taking double scattering and the muffin tin zero shift into account [158].

2.3.3 *Inelastic Scattering*

For a complete description of electron reflection without energy loss, elastic multiple scattering, and losses due to inelastic scattering have to be taken into account. Inasmuch as one inelastic scattering event is sufficient to remove an electron from the elastic channel, inelastic scattering can be taken into account via an inelastic mean free path (IMFP) λ_i in the elastic multiple scattering calculation. In contrast to the scattering in the much-studied higher energy range ($E > 100$ eV), where frequently strong simplifications of the angular distributions are made, in the energy range of interest in LEEM the angular distribution of the scattering by the individual atoms has to be fully taken into account. To a first approximation this can be done by considering only double scattering. This is justified by the fact that λ_i is frequently shorter than the elastic mean free path λ_e so that inelastic scattering has already caused considerable attenuation before the second elastic scattering process occurs. In the limit of very strong inelastic scattering single elastic scattering, can be used to estimate penetration depth and backscattered intensity [139–141]. In general, however, a more rigorous approach such as Monte Carlo simulation or Boltzmann transport equation methods has to be used. These methods have been developed well for higher energies as described repeatedly in reviews, for example in Refs. [159–162], but have been applied with realistic potentials to energies below 100 eV only rarely [163]. Reference [160] gives some results for the elastic MFP down to 10 eV but calculated with free atom potentials, which are inadequate at these low energies.

The theory of inelastic scattering of slow electrons is on much better footing. The original approach in connection with LEEM [139–141] assumed that the incident electron interacts with a degenerate electron gas (jellium approximation, Lindhard dielectric function), taking into account exchange and correlation, which were not included in the calculations of elastic scattering at low energies. Now calculations with more realistic descriptions of the interactions are available. In them material-specific dielectric functions are used [163, 164] or the Lindhard dielectric function is effectively replaced by a dielectric function obtained from experimental optical data (Penn algorithm [165]). In one case [163, 164] IMFP calculations were performed for SiO₂ down to below 0.1 eV, taking optical phonon excitation into account, and for C, Al and Ag down to the 1 eV range. IMFP results

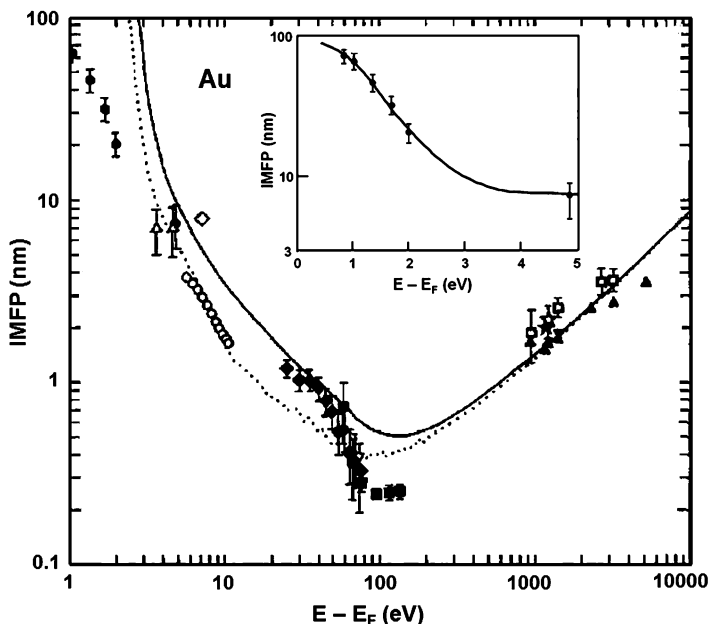


Fig. 2.29 Inelastic mean free path of electrons in Au as a function of energy. *Symbols* are from different measurements, lines from calculations using different plasmon dispersion relationships, the *dotted one* being more accurate. Adapted with permission from Ref. [166]. Copyright 1989 Elsevier

for 41 elemental solids for energies down to 50 eV calculated in this manner have been published by Tanuma et al. [112]. Below 100 eV they show a clear difference between the IMFPs of diamond on the one hand and graphite and glassy carbon on the other, indicating the strong influence of the electronic structure at low energies. For several elements the calculations down to 1 eV have been compared with experimental results [166]. Figure 2.29 shows as an example Au [166]. A difference in the dispersion relation assumed for the plasmon is responsible for the difference between the solid and the dashed curve, which gives a somewhat better fit to the experimental data. However, both curves deviate considerably from experiment, in particular at the lowest energies shown in more detail in the inset, which are, however, below the vacuum level and therefore not important for LEEM. The strong decrease above about 60 eV can be attributed to 5p excitations, which are apparently not taken into account in the dielectric function. Similar deviations below 100 eV have been found in a comparison of the calculations with elastic-peak electron spectroscopy measurements from many elemental polycrystalline solids, while above 200 eV theory and experiment agree very well [167] and follow the universal IMFP curve.

However at very low energy, let's say below 10 eV, the details of the electronic structure cause very large deviations from the "universal" IMFP, which is based on measurements from materials whose energy bands in this energy regions are

free electron-like (parabolic), such as Au, Ag, and Cu. The density of states $D(E) \sim \int dS_E / \nabla_k E(\mathbf{k})$, (dS_E surface with constant energy) into which electrons can be excited in these materials, is small. The situation is quite different in materials, which have d or f bands above the Fermi level. These are rather flat ($\nabla_k E(\mathbf{k}) \rightarrow 0$) so that $D(E)$ is very high and the probability of low energy electron excitations into these states is high, in particular if there is a high density of occupied states close to the Fermi level. For example in Fe $\lambda_i \approx 0.5$ nm below 25 eV in contrast to Au, in which λ_i rises from 1 nm into the 10 nm range. We will return to the short IMFPs in the 3d transition metals later in connection with spin-polarized low energy electron interactions. Thus, in the energy range of interest for LEEM the energy dependence of the IMFP is still poorly described by theory and—as we will see later in the discussion of diffraction by crystalline materials—is used as an adjustable parameter to fit experiment. The old calculations for low energies based on the jellium model [139–141, 168, 169] are of limited value because only Al and a few other metals are free electron-like. In the absence of reliable data for many materials an interpolation formula between a low energy expression, which had been proposed already by McRae [169], and one of the various high energy expressions of the IMFP gives probably useful IMFP values, although it contains parameters which have to be determined from experiment [170].

2.3.4 Surface Effects

The third important interaction affecting the reflection of slow electrons from surfaces in addition to the elastic and inelastic scattering *in* the specimen is scattering *from* the surface. This subject has a long history and will certainly also be studied in the future. It is immediately obvious that the reflection of a slow electron is strongly influenced by the boundary between vacuum and condensed matter in which the mean potential differs from that outside typically by 10–20 V. The relative magnitude of this influence compared to the processes which occur inside the specimen depends strongly on the shape of the boundary. The simplest model is that of a sharp planar interface between vacuum and a polarizable medium with the dielectric constant ϵ . The incident electron then produces an image charge in the medium. This in turn produces the classical image potential $V(z)$ acting on the electron

$$V(z) = -\frac{\epsilon - 1}{\epsilon + 1} \frac{1}{4z}, \quad (2.24)$$

which for ideal metals ($\epsilon = -\infty$) assumes the familiar form $V(z) = -1/4z$ (in atomic (Hartree) energy units) or $-1/2z$ (in Rydberg units). For elemental semiconductors such as Si ($\epsilon = 11.9$) and organic semiconductors such as pentacene ($\epsilon = 5.3$) $V(z)$ is only slightly smaller, 0.84 times for Si and 0.68 for pentacene. There have also been numerous quantum mechanical calculations for the approximation of the metal by a free electron gas (jellium), which is inhomogeneous near the surface. They give

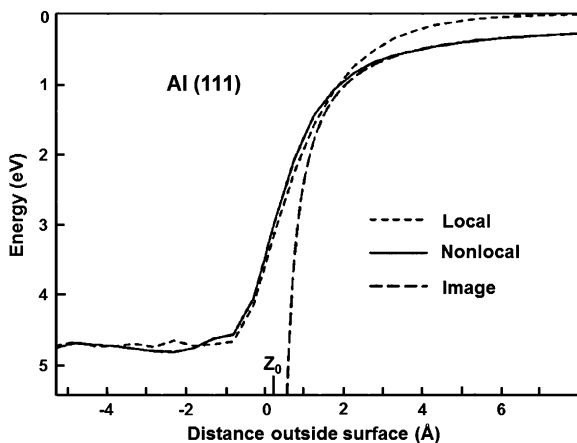


Fig. 2.30 Surface-averaged effective local potential experienced by electrons in the near-surface region of the Al(111) surface. *Long-dash line*: classical image potential, *short-dash line*: local density approximation, *continuous line*: GW approximation for the self-energy. z_0 is the image plane position obtained from the GW calculation. (G single-particle Green's function, W screened Coulomb interaction). Adapted with permission from Ref. [177]. Copyright 1998 by the American Physical Society

essentially the same $1/z$ dependence for the asymptotic form ($z \rightarrow \infty$) of $V(z)$. It has been suggested to add a correction term α_{KSx}/z to account for the exchange potential at the surface, which depends upon the potential step at the surface and the Fermi energy in the bulk: $V(z) = -(\alpha_{KSx} + 1/4)/z$ [171, 172]. α_{KSx} is approximately $1/4$ for most metals, ranging from about 0.22 for Fe to 0.26 for Cs.

While there is general agreement on the asymptotic $1/z$ form of the image potential the region close to the surface poses a problem because the potential goes to $-\infty$. The simplest and frequently used solution of this problem is to cut the potential at a distance z_0 and fit it in some manner to the potential inside the medium so that $V(z) = -1/4(z - z_0)$. In principle z_0 is the centroid of the image charge distribution but in general it is used as an adjustable parameter. Most early surface barrier models which simulate the transition to the asymptotic form have been reviewed repeatedly [173, 174] but others have been proposed too [175]. The most advanced calculations start from the electronic structure of crystal, taking the *nonlocality* of the exchange-correlation potential V_{xc} near the surface into account, similar to what has been done for jellium (see above), and fit $V(z) = -1/4(z - z_0)$ to the numerical results [176–178]. Referred to the geometric edge of the crystal, assumed to be half a layer spacing outside the outermost crystal plane, the z_0 value for Al (111) is 0.20 \AA [177, 178], for Al(100) 0.29 \AA [178] and for the jellium approximation of Al 0.38 \AA [178]. Figure 2.30 [177] show the potential near the Al(111) surface, averaged over planes parallel to the surface. The shape of the potential in the *local* density approximation (LDA) does not fit the image potential at large distances. The potential modulation parallel to the surface outside the surface is small for these densely packed surfaces so that the lateral averaging is good approximation. These calculations

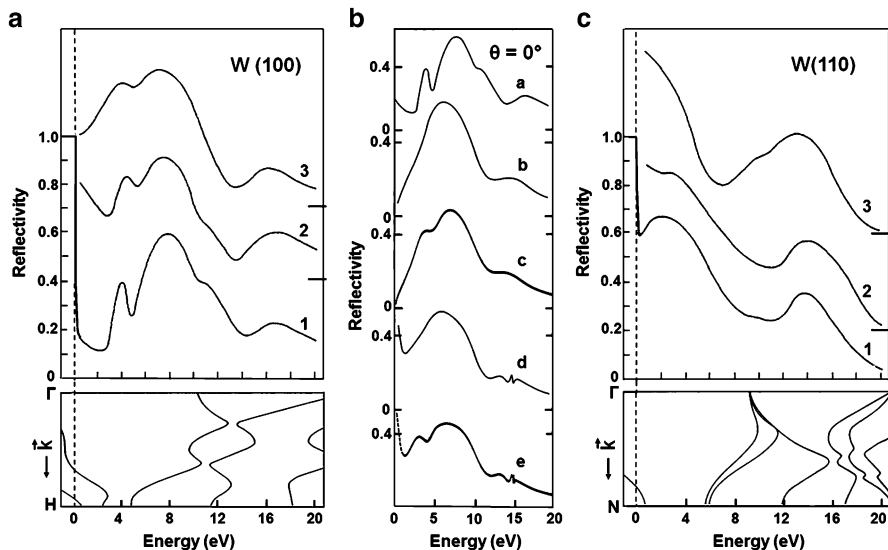


Fig. 2.31 Normal incidence specular electron reflectivity at very low energies. Comparison between experiment and theory for W(100) and W(110). The curves 1 and a are experimental curves, the curves 2, 3, and b–e are calculated for various models of the surface. d and e are from spin-dependent calculations. For explanation see text. (a, c) Adapted from Refs. [183, 184] with permission. Copyright 1981 Elsevier. (b) Reproduced from Ref. [185] with permission. Copyright 1983 by the American Physical Society

do not require any input from other calculations or from experiment but are very demanding because of the inclusion of the nonlocal V_{xc} .

Neglecting the nonlocality allows much less computer-intensive first-principle pseudopotential calculations but requires methods to bridge the gap between the self-consistent crystal potential and the correct image potential. This was achieved by several functions of z , which fit to each other also in the first derivatives and contain four parameters that are adjusted to reproduce the experimental binding energies of image states [179]. Calculations of this type for several densely packed free electron-like metals allowed construction of model potentials for 14 simple and noble metal surfaces [179]. This method was also extended to fcc(110) surfaces [180]. Still another approach to bridge the gap between crystal and asymptotic image potential is to mix the two potential $V_{\text{mix}}(z) = V_{\text{DFT}}(z)f(z) + V_{\text{im}}(z)(1 - f(z))$, with $f(z)$ changing from 0 to 1 as $\cos(z)$ in a chosen mixing region up to a chosen z_{mix} [181]. Thus theory has provided the experimentalist with a variety of surface barrier potentials which could be used in the interpretation of the reflection of the very slow electrons generally used in LEEM.

On the experimental side the surface barrier was introduced originally into LEED structure calculations more than 40 years ago to explain the resonances observed previously in nonspecular diffraction [182]. Subsequently the few specular reflectivity data at normal incidence, available before LEEM was available, were used to test various surface potential barriers. Figure 2.31 shows the fits

to the best experimental results, which were obtained in a trochoidal electron spectrometer with an energy resolution of 20 meV [183]. The fits on the left and right hand side are from Ref. [184], those in the center from Ref. [185]. Curves (1) (left and right) and (a) (in center) are the experimental data. Curves (3) (left and right) are fits with a nonreflecting barrier as used in standard LEED calculations above about 50 eV and curves (2) (left and right) are obtained by fitting the bulk potential to the asymptotic image potential with an exponential function. In the center panel (b) and (c) are for nonreflecting barrier fits without and with spin taken into account, while (d) and (e) are the corresponding fits with a bridging function to the asymptotic image potential.

It should be noted that some of the features such as the high reflectivity between 0 and 5 eV on the (110) surface and the reflectivity peak at 4 eV on the (100) surface can already be explained with the energy gaps in the bulk band structure. Most other features and the detailed energy dependence of the reflectivity however require a surface potential barrier. A band gap as the cause of a high reflectivity was already invoked by Andersson [186] to explain his results for the Cu(100) surface. That the reflectivity does not reach the value 1 is in part due to inelastic scattering of the evanescent wave decaying into the crystal in the energy range of the gap and in part due to the influence of the surface barrier. A comparison of the fits in Fig. 2.31 shows that none of them can reproduce the experiment. It remains to be seen if the methods for the calculation of the surface potential barrier, which have been developed more recently as described above, will produce quantitative agreement with experiment. Several more factors in addition to the proper magnitude and energy dependence of the imaginary potential, which is a measure for the inelastic mean free path, and of the real part of the self-energy, which will be discussed below, have to be taken onto account: surface relaxation, enhanced thermal vibrations of the surface atoms and the deviation of the scattering potential of the atoms in the topmost layers from that in the bulk. In addition also anisotropic damping can occur at energies at which the first diffracted beam emerges from the surface [187] as shown for the Cu(111) surface [188].

2.3.5 *VLEED, LEETS, TCS*

One of the main driving forces for very low energy electron diffraction (VLEED) was and is to obtain information on the electronic band structure. This can be obtained also by the complementary method of measuring the current to the crystal. Early efforts in this direction started already more than 50 years ago but did not became more broadly applied until the late 1970s, mainly thanks to the efforts of Sanche [189] and Komolov et al. [190]. Sanche called his method low energy electron transmission spectroscopy (LEETS) because he was interested in the interaction of slow electrons with thin crystalline organic and noble gas films on metals, while Komolov, whose interest was the electronic structure of crystals, called it total current spectroscopy (TCS), sometimes also called absorbed

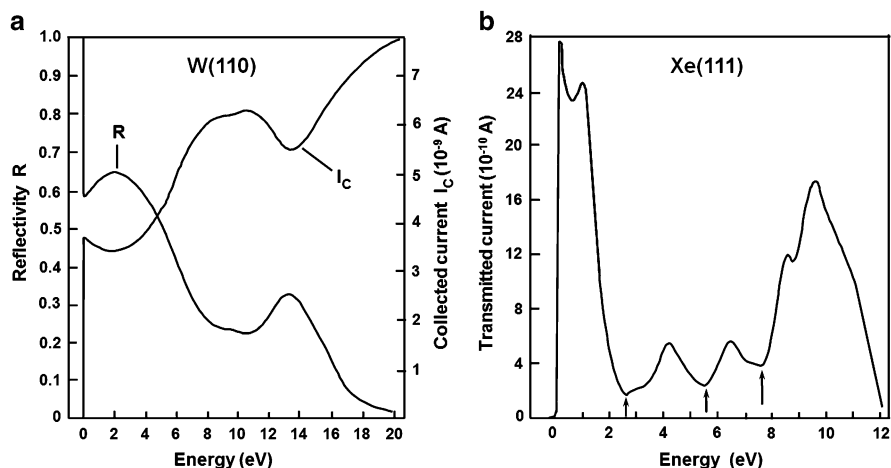


Fig. 2.32 (a) Complementarity of specular reflected current at normal incidence and collected current (“drain current”) I_c at low energies, at which inelastic scattering is small and no nonspecular scattering occurs. Example W(110). (b) Transmission of low energy electrons through a 100 monolayer thick (111)-oriented Xe film on (111)-oriented polycrystalline Pt (Pt drain current, “LEETS”). Normal incidence. The energy dependence is interpreted in terms of the density of unoccupied states and the energy-dependent inelastic mean free path. (a) From Ref. [183]. (b) Adapted with permission from Ref. [191]. Copyright 1985 by the American Physical Society

current spectroscopy. The complementarity with reflectivity is illustrated by the reflectivity $R(E)$ and $T(E)$ curves of W(110) in Fig. 2.32a [183], taken with the trochoidal electron spectrometer mentioned earlier. By proper choice of the potential of the electrodes in this system it is also possible to separate elastic from inelastic scattering [183]. Figure 2.32b [191] shows a LEETS spectrum of a (111)-orientated Xe layer on Pt from Sanche’s group [192]. The lowest energy loss that can occur in Xe is a transition into an exciton state at 8.45 eV above the conduction band. Therefore the structure seen in this figure is solely due to band structure effects and could be correlated with the electronic density of states: minima (maxima) correspond to energies with low (high) density of states. In particular, the strong decrease in transmission above 1.5 eV is due to a band gap and the subsequent oscillations are connected with variations in the band structure [193]. Above the first excitation threshold inelastic processes are superimposed on the loss-free features and give information on electronic transition.

A detailed analysis of the unoccupied density of states and of the *elastic* mean free path was made for solid Ar [194]. LEETS has been extended from simple atomic and molecular crystal layers to large biomolecules, which are difficult to crystallize. Although self-assembled monolayers can be prepared of them, for example of DNA [195], the complexity of the molecules requires an extension of the theory for the description of the scattering processes. A multiple scattering theory has been developed over the years by Caron and Sanche [196, 197] but

another approach has been taken too [198]. Several reviews [199–202] give a good impression of the possibilities and limitations of LEETS and also useful information on the interaction of slow electrons with insulating materials in general and biomolecules in particular. LEETS can become a useful complementary method in LEEM instruments without energy filter or with small beam separator angles (small energy dispersion), for example in microspectroscopy of organic materials or energy loss spectroscopy similar to Andersson's early work [203].

Total current spectroscopy (TCS) also would be a useful complement to LEEM for the same reasons, giving information on the electronic structure and excitations of the specimen. Early work has been reviewed by Komolov [204] and Strocov [205]. Close cooperation between experiment and theory has given detailed insight in the electronic structure of crystals such as NbSe₂ [206], graphite [207], TiTe₂ [208] or TiS₂ [209]. These results have been obtained in display type LEED systems with modified potentials by measuring the crystal target current $T(E)$, but have been presented as VLEED results, based on the relation $R(E) = 1 - T(E)$. While the experimental set-up of these measurements is simple, doing them in a LEEM system offers several advantages: (1) LEEM imaging allows first to select a region with well-defined microstructure, for example a step-free region, from which micro-TCS measurements can be made using a small illumination aperture; (2) the crystal surface can be aligned very precisely normal to the beam; (3) the coherence length is large; (4) in a system with an energy filter all electrons, which have lost more than 0.2–0.3 eV energy can be eliminated. Thus the reverse to what was said at the beginning of this paragraph is true too: LEEM is a good complement to TCS.

An important point, which has been mentioned several times, still has to be emphasized: the influence of the mean inner potential or muffin tin potential V_0 on the analysis of $R(E)$ and $T(E)$ measurements and of the LEED $I(V)$ analysis, which will be discussed briefly below. The value of V_0 depends upon the radius at which the periodic potential of the ion cores is cut off. It can be optimized for specific ion core combinations and can take into account surface core level shifts [210]. An additional electron injected into the N -electron system, for which the band structure was calculated, has exchange and correlation interactions with this N -electron system. Also, its energy is far above the Fermi energy and as a consequence it loses energy, which amounts to a loss of electrons in the incident electron beam (absorption). These two processes, which depend on the energy of the injected electron, are taken into account by a real part V_{or} in addition to V_0 , frequently called ΔE , and an imaginary part V_{oi} in the interaction potential ("optical potential", "self energy"). Furthermore, as already pointed out by Feibelman [9], the additional electron can also penetrate as an evanescent wave into the crystal in energy ranges, which are forbidden in the N -electron system, and lose energy. Thus the complex band structure must be used in the comparison between theory and experiment. This method is now well-developed (see for example Refs. [211, 212]). While V_{or} and V_{oi} could be calculated in principle, they are usually determined by comparison with experiment, V_{or} by shifting characteristic features in theory and experiment into coincidence, V_{oi} by fitting the widths of the peaks in the spectrum, which is determined by absorption. More details can be found in the original papers.

2.3.6 Quantum Well Effects

In an energy region in which absorption is weak, so that the IMFP is long, that is at low energies, information on the unoccupied band structure above the vacuum level normal to the surface can be obtained from interference effects in thin films with parallel boundaries, called quantum size effects (QSE). Interference effects in thin films had already been observed in specimen current (LEETS) measurements of (111)-oriented Au films on Ir by Thomas [213] and by Jonker et al. [214] in (111)-oriented Au and Ag films on W(110). While a rigorous interpretation of the interference phenomena requires a quantum mechanical treatment, to a first approximation the film may be considered as the electron wave optical analogue to the light-optical Fabry-Perot etalon. A more precise analysis takes absorption into account in a manner as described in Ref. [215] for an absorbing film on a transparent substrate, but generalized to an absorbing substrate. Extraction of the band structure does not have to go into this detail. It proceeds along the following line. For a wave with wavelength λ the condition for constructive interference in a film with thickness t is given by

$$n\lambda/2 + \varphi_1(E) + \varphi_2(E) = t \quad \text{or with } \lambda = 2\pi/k \quad kt - \Phi(E) = n\pi, \quad (2.25a)$$

where $\Phi(E) = k(E) \cdot (\varphi_1(E) + \varphi_2(E))$ and $\varphi_1(E)$, $\varphi_2(E)$ are the phase changes upon reflection at the two film boundaries. The unknown function $\Phi(E)$ can be eliminated using pairs n , t with the same energy, from which one can obtain

$$k(E) = \pi(n_2 - n_1)/(t_2 - t_1) \quad (2.25b)$$

and by inversion $E(k)$ in the direction \mathbf{k} normal to the film surface. The first band structure determinations from thin film interferences were done in a slightly different manner with LEETS using a trochoidal spectrometer by Perluzzo et al. [216]. Figure 2.33a shows their results for (111)-oriented Ar films on (111)-oriented Pt. The interference maxima in the film transmission are superimposed on the general energy dependence which is low at intermediate energies due to a band gap in Ar. The band structure deduced from these maxima is shown in Fig. 2.33b, together with the calculated band structure. More recent band structure determinations with this method have been done in the reflection mode in LEEM and will be discussed there together with other QSE effects in thin films in Chap. 5. QSE intensity oscillations in thin films occur also in reflection high energy electron diffraction as a function of angle of incidence at fixed thickness [217]. In the reflection of slow electrons at oblique incidence they have been observed as a function of film thickness [218]. In general QSE effects are unavoidable in thin films with parallel boundaries and provide many possibilities to extract information on the specimen, not only in reflection and transmission of electrons but also in photoemission and inverse photoemission, two methods, with which quantum size effects, also called quantum well effects, have been studied extensively [219].

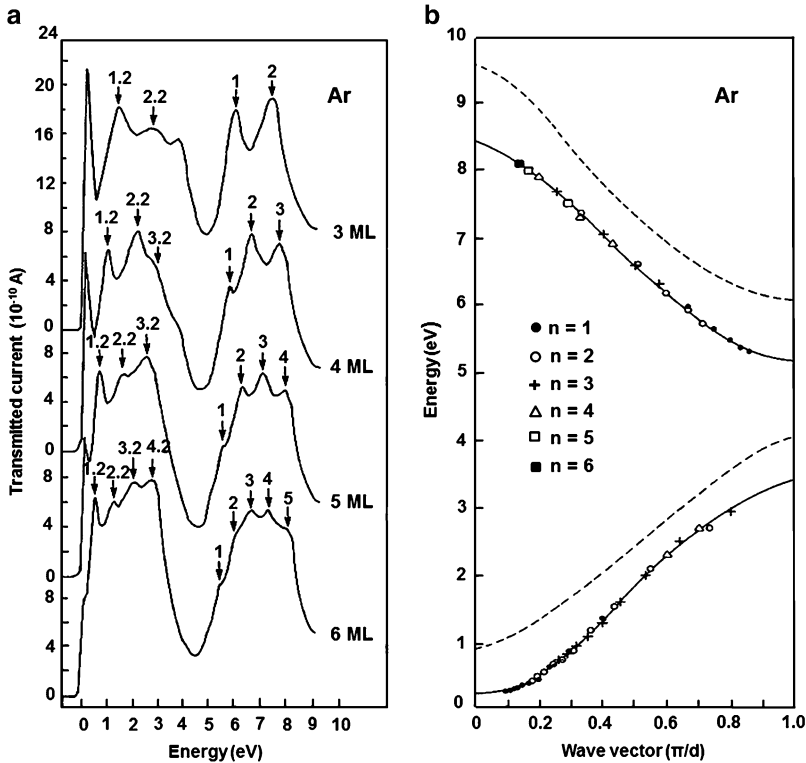


Fig. 2.33 (a) Quantum size oscillations in the transmitted current through (111)-oriented 3–6 monolayer thick Ar films on (111)-oriented polycrystalline Pt (normal incidence). The *numbers* at the maxima indicate the interference order including a phase shift factor characteristic for a given band. (b) Band structure $E(k)$ of Ar along the Γ –L direction derived from the data shown in (a). Adapted with permission from Ref. [216]. Copyright 1985 by the American Physical Society

2.3.7 Other Aspects

Concluding the discussion of the interaction of very slow electrons with surfaces, an important interaction still has to be mentioned: the specular reflection of spin-polarized electrons from ferromagnetic materials. At normal incidence and specular reflection as used in cathode lenses the reflected intensity is not influenced by spin-orbit coupling in contrast to spin-polarized LEED (SPLEED), which works with oblique angles of incidence. Therefore the only magnetic interaction, which the spin-polarized electron experiences is the exchange interaction. As a consequence the reflectivity R depends upon the relative orientation of the spin of the incident electron and of the electrons in the ferromagnetic material: $R \sim \mathbf{P} \cdot \mathbf{M}$, where \mathbf{P} is the spin polarization of the incident beam and \mathbf{M} the magnetization. All normal incidence specular reflection experiments made up to now, including the first one in

the diffraction mode [220], were made in LEEM instruments. Therefore the subject will be discussed in more detail in connection with magnetic imaging in Chap. 7. It should only be mentioned that very low energy spin-polarized electron reflectivity measurements can also be done at oblique incidence [218, 221] but the analysis is then more complicated because of the influence of the spin-orbit interaction.

Up to now we have been concerned with interactions in the energy range most frequently used in LEEM, i.e., up to about 20–30 eV. Higher energies are of relevance in combined LEEM-LEED studies using conventional LEED with energies between about 50 eV and several 100 eV. LEED studies in this energy range complement LEEM by giving information (1) on the lateral periodicity of the surface and on the surface defect structure below the resolution limit of LEEM and (2) on the atomic structure of the surface. In the first case the information is contained mainly in the intensity *distribution* in the LEED pattern, i.e., in the spot positions and shapes, which is described by the lattice factor, and its analysis requires only the kinematic theory of diffraction. In the second case the *relative intensities* of the diffraction spots allow extraction of the atomic positions within the lateral periodicity units (unit meshes) including their thermal vibrations. For this purpose the dynamical theory of diffraction which takes account of multiple scattering and absorption is used. In particular this second aspect of LEED has been covered in several books and review papers [222–229], to which the reader is referred. Reviews on spin-polarized LEED can be found in Refs. [40, 230, 231]. A number of software packages are available for structure analysis but only a few have been used up to now for LEED structure analysis in LEEM instruments. This is surprising in view of the significant advantages of LEED in a LEEM instrument compared to a standard LEED system: the (00) beam, which contains most of the information on the atomic arrangement normal to the surface, can be measured, the spots do not move with energy, there are no grids, which distort the diffraction spots and with an energy filter electrons, which suffered even only very small losses, are filtered out. Furthermore, the microstructure of surface region from which the LEED pattern is taken can be inspected. The disadvantages of slight distortions due to lens aberrations and misalignment or the limitation of the number of diffraction spots by the angular transmission of the objective lens are in general insignificant except perhaps when the lattice constants are very small.

The other application of standard LEED, determination of the lateral periodicity and of surface defects [232–235], is much more straightforward and has, therefore, found already considerable application in LEEM. Examples of such surface defects are two-dimensional island, antiphase domains, steps, in particular on vicinal planes, facet orientations, to name a few. To extract quantitative information beyond the lateral periodicity, however, requires delving somewhat into the instrument properties, which are characterized by the instrument response function. We will encounter it again in connection with the theory of image formation in Chap. 4. For LEED this function has been introduced by Park et al. [236] and subsequently discussed in more detail by others [237, 238]. The instrument response function

$T(\mathbf{k})$ describes how the instrument modifies the intensity $I_S(\mathbf{k})$ scattered from the specimen into direction \mathbf{k} as seen on the detector ($I_D(\mathbf{k})$):

$$I_D(\mathbf{k}) = I_S(\mathbf{k}) * T(\mathbf{k}), \quad (2.26)$$

where the sign $*$ means convolution. $T(\mathbf{k})$ includes the broadening of $I_S(\mathbf{k})$ caused by different angles of incidence resulting from the finite source size, the energy spread of the beam, the finite beam width, the resolution of the detector and other instrument properties. If $T(\mathbf{k})$ is known then $I_S(\mathbf{k})$ can be obtained by deconvolution and from it the real space information via Fourier transformation. Determination of $T(\mathbf{k})$ requires an ideal, defect-free specimen so that $I_S(\mathbf{k})$ is basically a δ function. In a conventional LEED system it is difficult to identify such specimen regions but in a LEEM system imaging allows to search for step-free regions and proper surface treatment can also minimize the number of adatoms and vacancies. Some refractory surfaces such as the W(110) surface are very well suited for this purpose. $T(\mathbf{k})$ is usually a Gaussian with Lorentzian tails. Of course, $T(\mathbf{k})$ depends strongly on the instrument settings such as cathode temperature, Wehnelt voltage, illumination focusing, and aperture and has to be determined for the specific settings used in the LEED experiment. Limitations of the fitting process in LEED have been pointed out in Ref. [239].

References

1. Brodskii, A.M., Gurevich, Y.Y., Levich, V.G.: General threshold theory of electron emission from the surface of a metal. *Phys Status Solidi* **40**, 139–151 (1970)
2. Jensen, K.L., Moody, N.A., Feldman, D.W., Montgomery, E.J., O'Shea, P.G.: Photoemission from metals and cesiated surfaces. *J. Appl. Phys.* **102**, 024911, 11 pages (2007)
3. Modinos, A.: *Field, Thermionic, and Secondary Electron Emission Spectroscopy*. Plenum, New York (1984)
4. Hutson, A.R.: Velocity analysis of thermionic emission from single-crystal tungsten. *Phys. Rev.* **98**, 889–901 (1955)
5. Herring, C., Nichols, M.H.: Thermionic emission. *Rev. Mod. Phys.* **21**, 185–270 (1949)
6. Dobretsov, L.N.: *Elektronen- und Ionenemission*. NASA Techn. Transl. TT F-73, NASA, Washington 1963. VEB Verlag Technik, Berlin (1954)
7. Nottingham, W.B.: Thermionic Emission. In: Flügge, S. (ed.) *Encyclopedia of Physics*, vol. 21, pp. 1–175. Springer, Berlin (1956)
8. Schwede, J.W., Bargatin, I., Riley, D.C., Hardin, B.E., Rosenthal, S.J., Sun, Y., Schmitt, F., Pianetta, P., Howe, R.T., Shen, Z.X., Melosh, N.A.: Photo-enhanced thermionic emission for solar concentrator systems. *Nat. Mater.* **9**, 762–767 (2010)
9. Feibelman, P., Eastman, D.E.: Photoemission spectroscopy: correspondence between quantum theory and experimental phenomenology. *Phys. Rev. B* **10**, 4932–4947 (1974)
10. Pendry, J.B.: Theory of photoemission. *Surf. Sci.* **57**, 679–705 (1976)
11. Berglund, C.N., Spicer, W.E.: Photoemission studies of silver and copper: theory. *Phys. Rev.* **136**, A1030–A1044 (1964)
12. Feuerbacher, B., Fitton, B., Willis, R.F. (eds.): *Photoemission and the Electronic Properties of Surfaces*. John Wiley & Sons, Chichester (1978)
13. Kevan, S.D. (ed.): *Angle-Resolved Photoemission*. Elsevier, Amsterdam (1992)

14. Hedin, L.: On correlation effects in electron spectroscopies and the GW approximation. *J. Phys. Condens. Matter* **11**, R489–R528 (1999)
15. Hüfner, S.: *Photoelectron Spectroscopy Principles and Applications*, 3rd edn. Springer, Berlin (2003)
16. Schattke, W., van Hove, M.A. (eds.): *Solid-State Photoemission and Related Methods*. Wiley-VCH, Weinheim (2003)
17. Hüfner, S. (ed.): *Very High Resolution Photoelectron Spectroscopy*. Springer, Berlin (2007)
18. Schwabl, F.: *Advanced Quantum Mechanics*, p. 187. Springer, Berlin (1999)
19. Kantorovich, I.I.: Nonlinear surface photoelectric effect in metals subjected to intense light. *Sov. Phys. Tech. Phys.* **22**, 397–399 (1977)
20. Anisimov, S.I., Benderskiĭ, V.A., Farkas, G.: Nonlinear photoelectric emission from metals induced by laser irradiation. *Sov. Phys. Usp.* **20**, 467–488 (1977)
21. Ferrini, G., Banfi, F., Giannetti, C., Parmigiani, F.: Non-linear electron photoemission from metals with ultrashort laser pulses. *Nucl. Instrum. Meth. Phys. Res. A* **601**, 123–131 (2009)
22. Fowler, R.H.: The analysis of photoelectric sensitivity curves for clean metals at various temperatures. *Phys. Rev.* **38**, 45–56 (1931)
23. DuBridge, L.A.: Theory of the energy distribution of photoelectrons. *Phys. Rev.* **43**, 727–741 (1933)
24. Mahan, G.D.: Theory of photoemission in simple metals. *Phys. Rev. B* **2**, 4334–4350 (1970)
25. Kong, X., Rowe, J.E., Nemanich, R.: Single molecule measurements with photoelectron emission microscopy. *J. Vac. Sci. Technol. B* **26**, 1461–1465 (2008)
26. Kane, E.O.: Theory of photoelectric emission from semiconductors. *Phys. Rev.* **127**, 131–141 (1962)
27. Kuch, W., Schneider, C.M.: Magnetic dichroism in valence band photoemission. *Rep. Prog. Phys.* **64**, 147–204 (2001)
28. Braun, J., Borstel, G.: Relativistic photoemission theory applied to GaAs(110). *Phys. Rev. B* **48**, 14373–14380 (1993)
29. Eckardt, H., Fritsche, L., Noffke, J.: Self-consistent relativistic band structure of the noble metals. *J. Phys. F Met. Phys.* **14**, 97–112 (1984)
30. Krasovskii, E.E., Schattke, W., Jiříček, P., Vondráček, M., Krasovska, O.V., Antonov, N.V., Shpak, A.P., Bartoš, I.: Photoemission from Al(100) and (111): experiment and ab initio theory. *Phys. Rev. B* **78**, 165406, 9 pages (2008)
31. Feibelman, P.: Surface electromagnetic fields. *Progr. Surf. Sci.* **12**, 284–408 (1982)
32. Gartland, P.O., Berge, S., Slagsvold, B.J.: Surface-effect characteristics of photoemission from clean copper-crystal surface. *Phys. Rev. Lett.* **30**, 916–919 (1973)
33. Gartland, P.O., Slagsvold, B.J.: Transitions conserving parallel momentum in photo emission from the (111) face of copper. *Phys. Rev. B* **12**, 4047–4058 (1975)
34. Pedersoli, E., Greaves, C.M.R., Wan, W., Coleman-Smith, C., Padmore, H.A., Pagliara, S., Cartella, A., Lamarca, F., Ferrini, G., Galimberti, G., Montagnese, M.: dal Conte, S., Parmigiani, F.: Surface and bulk contribution to Cu(111) quantum efficiency. *Appl. Phys. Lett.* **93**, 183505, 3 pages (2008)
35. Lobo-Checa, J., Ortega, J.E., Mascaraque, A., Michel, E.G., Krasovskii, E.E.: Effect of photoelectron mean free path on the photoemission cross-section of Cu(111) and Ag(111) Shockley states. *Phys. Rev. B* **84**, 245419, 6 pages (2011)
36. Rios Rubiano, C.A., Gravielle, M.S., Mitnik, D.M., Silkin, V.M.: Band-structure effects in photoelectron-emission spectra from metal surfaces. *Phys. Rev. A* **85**, 043422, 8 pages (2012)
37. Bisio, F., Nývlt, M., Franta, J., Petek, H., Kirschner, J.: Mechanisms of high-order perturbative photoemission from Cu(001). *Phys. Rev. Lett.* **96**, 087601, 4 pages (2006)
38. Roth, S., Leuenberger, D., Osterwalder, J., Dahl, J.E., Carlson, R.M.K., Tkachenko, B.A., Fokin, A.A., Schreiner, P.R., Hengsberger, M.: Negative-electron-affinity diamondoid monolayers as high-brilliance source for ultrashort electron pulses. *Chem. Phys. Lett.* **495**, 102–108 (2010)

39. Feder, R. (ed.): Polarized Electrons in Surface Physics. World Scientific Publications, Singapore (1985)
40. Kirschner, J.: Polarized Electrons at Surfaces (Springer Tracts in Modern Physics), vol. 106. Springer, Berlin (1985)
41. Heinzmann, U.: Angle-, energy- and spin-resolved photoelectron emission using circularly polarized synchrotron radiation. *Phys. Scr.* **T17**, 77–88 (1987)
42. Johnson, P.D.: Spin-polarized photoemission. *Rep. Prog. Phys.* **60**, 1217–1304 (1997)
43. Winkelmann, A., Lin, W.-C., Bisio, F., Petek, H., Kirschner, J.: Interferometric control of spin-polarized electron populations at a metal surface observed by multiphoton photoemission. *Phys. Rev. Lett.* **100**, 206601, 4 pages (2008)
44. Chiang, C.-T., Winkelmann, A., Henk, J., Bisio, F., Kirschner, J.: Spin-selective pathways in linear and nonlinear photoemission from ferromagnets. *Phys. Rev. B* **85**, 165137, 4 pages (2012)
45. Tusche, C., Ellguth, M., Ünal, A.A., Chiang, C.-T., Winkelmann, A., Krasnyuk, A., Hahn, M., Schönhense, G., Kirschner, J.: Spin resolved photoelectron microscopy using a two-dimensional spin-polarizing electron mirror. *Appl. Phys. Lett.* **99**, 032505, 3 pages (2011)
46. Marx, G.K.L., Elmers, H.J., Schönhense, G.: Magneto-optical linear dichroism in threshold photoemission electron microscopy of polycrystalline Fe films. *Phys. Rev. Lett.* **84**, 5888–5891 (2000)
47. Nakagawa, T., Yokoyama, T.: Magnetic circular dichroism near the fermi level. *Phys. Rev. Lett.* **96**, 237402, 4 pages (2006)
48. Nakagawa, T., Yokoyama, T., Hosaka, M., Katoh, M.: Measurements of threshold photoemission magnetic dichroism using ultraviolet lasers and a photoelastic modulator. *Rev. Sci. Instrum.* **78**, 023907, 5 pages (2007)
49. Dil, J.H.: Spin and angle resolved photoemission on non-magnetic low-dimensional systems. *J. Phys. Condens. Matter* **21**, 403001, 22 pages (2009)
50. Aeschlimann, M., Schmittenmaier, C.A., Elsayed-Ali, H.E., Miller, R.J.D., Cao, J., Gao, Y., Mantell, D.A.: Observation of surface enhanced multiphoton photoemission from metal surfaces in the short pulse limit. *J. Chem. Phys.* **102**, 8606–8613 (1995)
51. Raether, H.: Surface Plasmons on Smooth and Rough Surfaces and on Gratings. Springer Tracts in Modern Physics, vol. 111. Springer, New York (1988)
52. Liebsch, A.: Electronic Excitations at Metal Surfaces. Plenum, New York (1997)
53. Zayats, A.V., Smolyaninov, I.I., Maradudin, A.A.: Nano-optics of surface plasmon polaritons. *Phys. Rep.* **408**, 131–314 (2005)
54. Pitarke, J.M., Silkin, V.M., Chulkov, E.V., Echenique, P.M.: Theory of surface plasmons and surface-plasmon polaritons. *Rep. Prog. Phys.* **70**, 1–87 (2007)
55. Berini, P.: Long-range surface plasmon-polariton waveguides in silica. *J. Appl. Phys.* **102**, 053105, 9 pages (2007)
56. Maier, S.A.: Plasmonics: Fundamentals and Applications. Springer, New York (2007)
57. Kawata, S. (ed.): Near-Field Optics and Surface Plasmon Polaritons. Springer, Berlin (2001)
58. Homola, J.: Surface Plasmon Resonance Based Sensors. Springer, Berlin (2006)
59. Ozbay, E.: Plasmonics: merging plasmonics and electronics at nanoscale dimensions. *Science* **311**, 189–193 (2006)
60. Shalaev, V.M., Kawata, S. (eds.): Nanophotonics with Surface Plasmons. Elsevier, Amsterdam (2007)
61. Halas, N.J.: Plasmons in strongly coupled metallic nanostructures. *Chem. Rev. Mod. Phys.* **111**, 3913–3961 (2011)
62. Stockman, M.I.: Nanoplasmonics: past, present, and glimpse into future. *Opt. Express* **19**, 22029–22106 (2011)
63. Kubo, A., Petek, H.: Femtosecond time-resolved photoemission electron microscope study of surface plasmon dynamics. *J. Vac. Soc. Jap. (Japanese)* **51**(368–376) (2008)
64. Shalaev, V.M., Douketis, C., Haslett, T., Stuckless, T., Moskovits, M.: Two-photon electron emission from smooth and rough metal films in the threshold region. *Phys. Rev. B* **53**, 11193–11206 (1996)

65. Kelly, K.L., Coronado, E., Zhao, L.L., Schatz, G.C.: The optical properties of metal nanoparticles: the influence of size, shape, and dielectric environment. *J. Phys. Chem. B* **107**, 668–677 (2003)
66. Geshev, P., Klein, S., Witting, T., Dickmann, K., Hietschold, M.: Calculation of the electric-field enhancement at nanoparticles of arbitrary shape in close proximity to a metallic surface. *Phys. Rev. B* **70**, 075402, 16 pages (2004)
67. Gotschy, W., Vonmetz, K., Leitner, A., Aussenegg, F.R.: Optical dichroism of lithographically designed silver nanoparticle films. *Optics Lett.* **21**, 1099–1101 (1996)
68. Kreibig, U., Vollmer, W.: *Optical Properties of Metal Clusters*. Springer, Berlin (1995)
69. Lehmann, J., Merschdorf, M., Pfeiffer, W., Thon, A., Voll, S., Gerber, G.: Surface plasmon dynamics in silver nanoparticles studied by femtosecond time-resolved photoemission. *Phys. Rev. Lett.* **85**, 2921–2924 (2000)
70. Kennerknecht, C., Hovel, H., Merschdorf, M., Voll, S., Pfeiffer, W.: Surface plasmon assisted photoemission from Au nanoparticles on graphite. *Appl. Phys. B* **73**, 425–429 (2001)
71. Merschdorf, M., Kennerknecht, C., Pfeiffer, W.: Collective and single-particle dynamics in time-resolved two-photon photoemission. *Phys. Rev. B* **70**, 193401, 4 pages (2004)
72. Irvine, S.E., Dechant, A., Elezzabi, A.Y.: Generation of 0.4-keV femtosecond electron pulses using impulsively excited surface Plasmons. *Phys. Rev. Lett.* **93**, 184801, 4 pages (2004)
73. Yalunin, S.V., Gulde, M., Ropers, C.: Strong-field photoemission from surfaces: theoretical approaches. *Phys. Rev. B* **84**, 195426, 14 pages (2011)
74. Faraggi, M., Aldazabal, I., Gravielle, M.S., Arnau, A., Silkin, V.M.: Study of the induced potential produced by ultrashort pulses on metal surfaces. *J. Opt. Soc. Am. B* **26**, 2331–2336 (2009)
75. Faraggi, M.N., Gravielle, M.S., Mitnik, D.M.: Interaction of ultrashort laser pulses with metal surfaces: impulsive jellium-Volkov approximation versus the solution of the time-dependent Schrödinger equation. *Phys. Rev. A* **76**, 012903, 6 pages (2007)
76. Bagus, P.S., Ilton, E.S.: Effects of covalency on the p-shell photoemission of transition metals: MnO. *Phys. Rev. B* **73**, 155110, 14 pages (2006)
77. Haverkort, M.W., Zwierzycki, M., Andersen, O.K.: Multiplet ligand-field theory using Wannier orbitals. *Phys. Rev. B* **85**, 165113, 20 pages (2012)
78. Bagus, P.S., Broer, R., Ilton, E.S.: Atomic near-degeneracy for photoemission: generality of 4f excitations. *J. Electron. Spectrosc. Relat. Phenom.* **165**, 46–49 (2008)
79. Bagus, P.S., Freeman, A.J., Sasaki, F.: Prediction of new multiplet structure in photoemission experiments. *Phys. Rev. Lett.* **30**, 850–853 (1973)
80. Nelín, C.J., Bagus, P.S., Ilton, E.S., Chambers, S.A., Kühlenbeck, H., Freund, H.-J.: Relationships between complex core level spectra and materials properties. *Int. J. Quantum Chem.* **110**, 2752–2764 (2010)
81. Uldry, A., Vernay, F., Delley, B.: Systematic computation of crystal-field multiplets for x-ray core spectroscopies. *Phys. Rev. B* **85**, 125133, 14 pages (2012)
82. Egelhoff Jr., W.F.: Core-level binding-energy shifts at surfaces and in solids. *Surf. Sci. Rep.* **6**, 253–415 (1987)
83. de Groot, F., Kotani, A.: *Core Level Spectroscopy of Solids*. CRC Press, Boca Raton (2008)
84. Gerson, A.R., Bredow, T.: Interpretation of sulphur 2p XPS spectra in sulfide minerals by means of ab initio calculations. *Surf. Interface Anal.* **29**, 145–150 (2000)
85. www.casaxps.com/help_manual/manual_updates/peak_fitting_in_xps.pdf
86. Yamashita, T., Hayes, P.: Effect of curve fitting parameters on quantitative analysis of Fe_{0.94}O and Fe₂O₃ using XPS. *J. Electron. Spectrosc. Relat. Phenom.* **152**, 6–11 (2006)
87. Pratt, A.: Fine structure in XPS and XANES spectra acquired from a series of sphalerite samples. *ECS Trans.* **28**, 95–103 (2010)
88. Harmer, S.L., Goncharova, L.V., Kolarova, R., Lennard, W.N., Munoz-Marquez, M.A., Mitchell, I.V., Nesbitt, H.W.: Surface structure of sphalerite studied by medium energy ion scattering and XPS. *Surf. Sci.* **601**, 352–361 (2007)

89. Jirsak, T., Rodriguez, J.A., Chaturvedi, S., Hrbek, J.: Chemistry of SO₂ on Ru(001): formation of SO₃ and SO₄. *Surf. Sci. Rep.* **418**, 8–21 (1998)
90. Nesbitt, H.W., Schaufuss, A.G., Scaini, M., Bancroft, G.M., Szargan, R.: XPS measurement of fivefold and sixfold coordinated sulfur in pyrrhotites and evidence for millerite and pyrrhotite surface species. *Am. Mineral.* **86**, 318–326 (2001)
91. Skinner, W.M., Nesbitt, H.W., Pratt, A.R.: XPS identification of bulk hole defects and itinerant Fe 3d electrons in natural troilite (FeS). *Geochim. Cosmochim. Acta* **68**, 2259–2263 (2004)
92. Sinkovic, B., Johnson, P.D., Brookes, N.B.: Magnetic structure of oxidized Fe(001). *Phys. Rev. Lett.* **65**, 1647–1650 (1990)
93. Tamura, E., Waddill, G.D., Tobin, J.G., Sterne, P.A.: Linear and circular dichroism in angle resolved Fe 3p photoemission. *Phys. Rev. Lett.* **73**, 1533–1536 (1994)
94. Tait, S.L., Wang, Y., Costantini, G., Lin, N., Baraldi, A., Esch, F., Petaccia, L., Lizzit, S., Kern, K.: Metal-organic coordination interactions in Fe-terephthalic acid networks on Cu (100). *J. Am. Chem. Soc.* **130**, 2108–2113 (2008)
95. Jungblut, R., Roth, Ch., Hillebrecht, F.U., Kisker, E.: Spin-polarized electron spectroscopy as a combined chemical and magnetic probe. *Surf. Sci.* **269/270**, 615–621 (1992)
96. Van Campen, D.G., Pouliot, R.J., Klebanoff, L.E.: Spin-resolved x-ray-photoelectron-spectroscopy study of ferromagnetic iron. *Phys. Rev. B* **48**, 17535, 5 pages (1993)
97. Roth, C., Hillebrecht, F.U., Rose, H.B., Kisker, E.: Linear magnetic dichroism in angular resolved Fe 3p core level photoemission. *Phys. Rev. Lett.* **70**, 3479–3482 (1993)
98. Roth, C., Rose, H.B., Hillebrecht, F.U., Kisker, E.: Magnetic linear dichroism in soft X-ray core level photoemission from iron. *Solid State Commun.* **86**, 647–650 (1993)
99. Rossi, G., Sirotti, F.: 3p Fine structure of ferromagnetic Fe and Co from photoemission with linearly polarized light. *Solid State Commun.* **90**, 557–562 (1994)
100. Tobin, J.G., Goodman, K.W., Schumann, F.O., Willis, R.F., Kortright, J.B., Denlinger, J.D., Rotenberg, E., Warwick, A., Smith, N.V.: Generalized description of magnetic x-ray circular dichroism in Fe 3p photoelectron emission. *J. Vac. Sci. Technol. A* **15**, 1766–1769 (1997)
101. Huang, D.-J., Riffe, D.M., Erskine, J.I.: Simultaneous determination of Fe 3p spin-orbit and exchange splittings in photoemission. *Phys. Rev. B* **51**, 15170–15179 (1995)
102. Bansmann, J., Lu, L., Meiwes-Broer, K.H., Schlatholter, T., Braun, J.: Relationship between magnetic circular and linear dichroism in photoemission from Fe 3p core level: an experimental and theoretical investigation. *Phys. Rev. B* **60**, 13860–13868 (1999)
103. Liu, Y., Xu, Z., Johnson, P.D., van der Laan, G.: Spin-orbit coupling, exchange interaction, and hybridization in the photoexcitation of the Ni 3p core level. *Phys. Rev. B* **52**, R8593–R8596 (1995)
104. Thompson, A., et al. (eds.): X-Ray Data Booklet. Lawrence Berkeley National Laboratory, Berkeley, CA (2009)
105. <http://xdb.lbl.gov>
106. Yeh, J.J., Lindau, I.: Atomic subshell photoionization cross sections and asymmetry parameters: $1 < Z < 103$. *At. Data. Nucl. Data Tables* **32**, 1–155 (1985)
107. Ferguson, I.: Auger Microprobe Analysis. Adam Hilger, Bristol (1989)
108. Powell, C.J., Jablonski, A.: Surface sensitivity of X-ray photoelectron spectroscopy. *Nucl. Instrum. Meth. Phys. Res. A* **601**, 54–65 (2009)
109. Jablonski, A., Powell, C.J.: Practical expressions for the mean escape depth, the information depth, and the effective attenuation length in Auger-electron spectroscopy and x-ray photoelectron spectroscopy. *J. Vac. Sci. Technol. A* **27**, 253–261 (2009)
110. Jablonski, A., Powell, C.J.: Improved analytical formulae for correcting elastic-scattering effects in X-ray photoelectron spectroscopy. *Surf. Sci.* **604**, 327–336 (2010)
111. Powell, C.J., Jablonski, A.: Progress in quantitative surface analysis by X-ray photoelectron spectroscopy: current status and perspectives. *J. Electron. Spectrosc. Relat. Phenom.* **178–179**, 331–346 (2010)

112. Tanuma, S., Powell, C.J., Penn, D.R.: Calculations of electron inelastic mean free paths. IX. Data for 41 elemental solids over the 50 eV to 30 keV range. *Surf. Interface Anal.* **43**, 689–713 (2011)
113. Seah, M.P.: An accurate and simple universal curve for the energy-dependent electron inelastic mean free path. *Surf. Interface Anal.* **44**, 497–503 (2012)
114. Nakajima, R., Stöhr, J., Idzerda, Y.U.: Electron-yield saturation effects in L-edge x-ray magnetic circular dichroism spectra of Fe, Co, and Ni. *Phys. Rev. B* **59**, 6421–6429 (1999)
115. Frazer, B.H., Gilbert, B., Sonderegger, B.R., De Stasio, G.: The probing depth of total electron yield in the sub-keV range: TEY-XAS and X-PEEM. *Surf. Sci. Rep.* **537**, 161–167 (2003)
116. Dreiner, S., Schurmann, M., Westphal, C.: Structural analysis of the SiO₂/Si(100) interface by means of photoelectron diffraction. *Phys. Rev. Lett.* **93**, 126101, 4 pages (2004)
117. Woodruff, D.P.: Surface structural information from photoelectron diffraction. *J. Electron. Spectrosc. Relat. Phenom.* **178–179**, 186–194 (2010)
118. Sébilleau, D., Natoli, C.R.: Some insight into the convergence of the multiple scattering series expansion. In: 14th Int. Conf. on X-Ray Absorption Fine Structure (XAFS14) 2009, pp. 1–12. *J. Phys. Conf. Ser.* (2009)
119. Sébilleau, D., Natoli, C., Gavaza, G.M., Zhao, H., Da Pieve, F., Hatada, K.: MsSpec-1.0: a multiple scattering package for electron spectroscopies in material science. *Comput. Phys. Commun.* **182**, 2567–2579 (2011)
120. Fadley, C.S.: X-ray photoelectron spectroscopy: progress and perspectives. *J. Electron. Spectrosc. Relat. Phenom.* **178–179**, 2–32 (2010)
121. Henke, B.L., Smith, J.A., Attwood, D.T.: 0.1–10-keV x-ray-induced electron emissions from solids: models and secondary electron measurements. *J. Appl. Phys.* **48**, 1852–1866 (1977)
122. Henke, B.L., Liesegang, J., Smith, S.D.: Soft-x-ray-induced secondary-electron emission from semiconductors and insulators: models and measurements. *Phys. Rev. B* **19**, 3004–3021 (1979)
123. Stöhr, J.: *NEXAFS Spectroscopy*. Springer, Berlin (1992)
124. Kasrai, M., Brown, J.R., Bancroft, G.M., Yin, Z., Tan, K.H.: Sulphur characterization in coal from X-ray absorption near edge spectroscopy. *Int. J. Coal Geol.* **32**, 107–135 (1996)
125. Henke, B.L., Lee, P., Tanaka, T.J., Skimabukuro, R.L., Fujikawa, B.K.: Low-energy X-ray interaction coefficients: photoabsorption, scattering and reflection, $E = 100\text{--}2000$ eV, $Z = 1\text{--}94$. *At. Data. Nucl. Data Tables* **27**, 1–144 (1982)
126. Henke, B.L., Gullikson, E.M., Davis, J.C.: X-ray interactions: photoabsorption, scattering, transmission, and reflection at $E = 50\text{--}30,000$ eV, $Z = 1\text{--}92$. *At. Data. Nucl. Data Tables* **54**, 181–342 (1993)
127. www-cxro.lbl.gov/optical_constants/
128. Stöhr, J., Siegmann, H.C.: *Magnetism*. Springer, Berlin (2006)
129. Beth, R.A.: Mechanical detection and measurement of the angular momentum of light. *Phys. Rev.* **50**, 115–125 (1936)
130. Stewart, A.M.: Angular momentum of the electromagnetic field: the plane wave paradox resolved. *Eur. J. Phys.* **26**, 635–641 (2005)
131. Mansuripur, M.: Angular momentum of circularly polarized light in dielectric media. *Opt. Express* **13**, 5315–5324 (2005)
132. Papaconstantopoulos, D.A.: *Handbook of the Band Structure of Elemental Solids*. Plenum, New York (1986)
133. Stöhr, J.: Exploring the microscopic origin of magnetic anisotropies with X-ray magnetic circular dichroism (XMCD) spectroscopy. *J. Magn. Magn. Mater.* **200**, 470–497 (1999)
134. Wilhelm, F., Pouloupoulos, P., Srivastava, P., Wende, H., Farle, M., Baberschke, K., Angelakeris, M., Flevaris, N.K., Grange, W., Kappler, J.-P., Ghiringhelli, G., Brookes, N. B.: Magnetic anisotropy energy and the anisotropy of the orbital moment of Ni in Ni/Pt multilayers. *Phys. Rev. B* **61**, 8647–8650 (2000)
135. Arai, K., Okuda, T., Tanaka, A., Kotsugi, M., Fukumoto, K., Oura, M., Senba, Y., Ohashi, H., Nakamura, T., Matsushita, T., Muro, T., Kakizaki, A., Kinoshita, T.: Complete assignment of

- spin domains in antiferromagnetic NiO(100) by photoemission electron microscopy and cluster model calculation. *J. Phys. Soc. Jpn.* **79**, 013703, 4 pages (2010)
136. Kunes, J., Oppeneer, P.M.: Anisotropic x-ray magnetic linear dichroism at the L_{2,3} edges of cubic Fe, Co, and Ni: Ab initio calculations and model theory. *Phys. Rev. B* **67**, 024431, 9 pages (2003)
 137. Spaldin, N.A., Cheong, S.-W., Ramesh, R.: Multiferroics: past, present, and future. *Phys. Today* **63**, 38–43 (2010)
 138. Bauer, E., Browne, H.N.: Elastic Scattering of Electrons by the Many-Electron Atom. In: McDowell, M.R.C. (ed.) *Proc. 3rd Int. Conf. on the Physics of Electronic and Atomic Collisions*, London 1963. Atomic Collision Processes, pp. 16–27. North-Holland, Amsterdam (1964)
 139. Bauer, E.: Interaction of slow electrons with surfaces. *J. Vac. Sci. Technol.* **7**, 3–12 (1970)
 140. Bauer, E.: Interaction of slow electrons with radium-jellium. In: *Les Interactions des Electrons avec la Matiere Condensee. Applications a l'Etude du Solide*. pp. 42–96. AVCP (1972)
 141. Bauer, E.: Low Energy Electron Diffraction (LEED) and Auger Methods. In: Gomer, R. (ed.) *Interactions on Metal Surfaces*, pp. 225–274. Springer, Berlin (1975)
 142. Bauer, E., Teliaps, W.: Low energy electron microscopy. In: *Scanning Microscopy*, vol. Suppl. 1. pp. 99–108. Scanning Microscopy Int., Chicago (1987)
 143. Bauer, E.: Low energy electron microscopy and normal incidence VLEED. In: Koukal, J. (ed.) *Physics of Solid Surfaces. Studies in Surface Science and Catalysis*, vol. 40, pp. 26–36. Elsevier, Amsterdam (1988)
 144. Bauer, E., Teliaps, W.: Emission and low energy reflection electron microscopy. In: Howie, A., Valdre, U. (eds.) *Surface and Interface Characterization by Electron Optical Methods*, vol. 191 NATO ASI Series B: Physics, pp. 195–233. Plenum, New York (1988)
 145. Bauer, E.: Low energy electron microscopy. *Rep. Prog. Phys.* **57**, 895–938 (1994)
 146. Bauer, E.: LEEM basics. *Surf. Rev. Lett.* **5**, 1275–1286 (1998)
 147. Berger, M.J., Seltzer, S.M., Wang, R., Schechter, A.: NISTIR Report No. 5188. In: Database ELAST (1993)
 148. Jablonski, A., Salvat, F., Powell, C.J.: NIST Standard Reference Database 64 version 3.1. (2003)
 149. www.nist.gov/srd/nist64.htm.
 150. Elastic scattering of electrons and positrons, ICRU report no. 77. In: ICRU – International Commission on Radiation Units and Measurements. (2007)
 151. Salvat, F., Jablonski, A., Powell, C.J.: ELSEPA-Dirac partial-wave calculation of elastic scattering of electrons and positrons by atoms, positive ions and molecules. *Comput. Phys. Commun.* **165**, 157–190 (2005)
 152. Herman, F., Skillman, S.: *Atomic Structure Calculations*. Prentice Hall, Englewood-Cliffs, NJ (1963)
 153. Fink, M., Martin, M.R., Somorjai, G.A.: Comparison of backscattering intensities for low energy electrons from various surface atoms (H, Li, Be, C, O, Al, Si, S, V, Cr, Ni, Cu, Ag, Pt, Au). *Surf. Sci.* **29**, 303–308 (1972)
 154. Snow, E.C.: Self-consistent energy bands of metallic copper by the augmented-plane-wave method. II. *Phys. Rev.* **171**, 785–789 (1968)
 155. Schmid, R., Gaukler, K.H., Seiler, H.: Measurement of elastically reflected electrons ($E \leq 2.5$ keV) for imaging of surfaces in a simple ultra high vacuum scanning electron microscope. In: *Scanning Electron Microscopy vol. II*, pp. 501–509. Scanning Electron Microscopy, Inc., O'Hare, Chicago (1983)
 156. Gergely, G.: Elastic backscattering of electrons: determination of physical parameters of electron transport processes by elastic peak electron spectroscopy. *Prog. Surf. Sci.* **71**, 31–88 (2002)
 157. Schilling, J.S., Webb, M.B.: Low-energy electron diffraction from liquid Hg: multiple scattering, scattering factor, and attenuation. *Phys. Rev. B* **2**, 1665–1676 (1970)
 158. Dietzel, W., Meister, G., Bauer, E.: Elastic and inelastic backscattering of slow electrons from silicon. *Z. Phys. B* **47**, 189–194 (1982)

159. Rösler, M., Brauer, W., Devooght, J., Dehaes, J.-C., Dubus, A., Cailler, M., Ganachaud, J.-P.: Particle Induced Electron Emission. Springer, Berlin (1991)
160. Ding, Z.-J., Shimizu, R.: A Monte Carlo modeling of electron interaction with solids including cascade secondary electron production. *Scanning* **18**, 92–113 (1996)
161. Dapor, M.: Electron-Beam Interactions with Solids: Application of the Monte Carlo Method to Electron Scattering. Springer, Berlin (2003)
162. Salvat, F., Fernandez-Varea, J.M.: Overview of physical interaction models for photon and electron transport used in Monte Carlo codes. *IOP Publ. Metrol.* **46**, S112–S138 (2009)
163. Fitting, H.-J., Schreiber, E., Kuhr, J.-C., von Czarnowski, A.: Attenuation and escape depths of low-energy electron emission. *J. Electron. Spectrosc. Relat. Phenom.* **119**, 35–47 (2001)
164. Kuhr, J.-C., Fitting, H.-J.: Monte Carlo simulation of electron emission from solids. *J. Electron. Spectrosc. Relat. Phenom.* **105**, 257–273 (1999)
165. Penn, D.R.: Electron mean-free-path calculations using a model dielectric function. *Phys. Rev. B* **35**, 482–486 (1987)
166. Ding, Z.-J., Shimizu, R.: Inelastic collisions of kV electrons in solids. *Surf. Sci.* **222**, 313–331 (1989)
167. Tanuma, S., Shiratori, T., Kimura, T., Goto, K., Ichimura, S., Powell, C.J.: Experimental determination of electron inelastic mean free paths in 13 elemental solids in the 50 to 5000 eV energy range by elastic-peak electron spectroscopy. *Surf. Interface Anal.* **37**, 833–845 (2005)
168. Penn, D.R.: Electron mean free paths for free-electron-like materials. *Phys. Rev. B* **13**, 5248–5254 (1976)
169. McRae, E.G.: Calculation of absorptive potentials for low energy electron scattering from optical data for solid Mg, Al, Cu, Ag, Au, Bi, C and Al_2O_3 . *Surf. Sci. Rep.* **57**, 761–765 (1976)
170. Ziaja, B., London, R.A., Hajdu, J.: Ionization by impact electrons in solids: electron mean free path fitted over a wide energy range. *J. Appl. Phys.* **99**, 033514, 9 pages (2006)
171. Qian, Z., Sahni, V.: Quantum mechanical image potential theory. *Phys. Rev. B* **66**, 205103, 4 pages (2002)
172. Qian, Z., Sahni, V.: Exact electronic properties in the classically forbidden region of a metal surface. *Int. J. Quantum Chem.* **104**, 929–945 (2005)
173. Jones, R.O., Jennings, P.J.: LEED fine structure: origin and applications. *Surf. Sci. Rep.* **9**, 165–196 (1988)
174. Jennings, P.J., Jones, R.O., Weinert, M.: Surface barrier for electrons in metals. *Phys. Rev. B* **37**, 6113–6120 (1988)
175. Malmstrom, G., Rundgren, J.: A program for calculation of the reflection and transmission of electrons through a surface potential barrier. *Comput. Phys. Commun.* **19**, 263–270 (1980)
176. Manghi, F.: Nonlocal exchange and correlation in surface calculations: an application to GaAs(110). *Phys. Rev. B* **33**, 2554–2558 (1986)
177. White, D., Godby, R.W., Rieger, M.M., Needs, R.J.: Dynamic image potential at an Al(111) surface. *Phys. Rev. Lett.* **80**, 4265–4268 (1998)
178. Heinrichsmeier, M., Fleszar, A., Hanke, W., Eguiluz, A.G.: Nonlocal density-functional calculations of the surface electronic structure of metals: application to aluminum and palladium. *Phys. Rev. B* **57**, 14974–14982 (1998)
179. Chulkov, E.V., Silkin, V.M., Echenique, P.M.: Image potential states on metal surfaces: binding energies and wave functions. *Surf. Sci.* **437**, 330–352 (1999)
180. Tsirkin, S.S., Ereameev, S.V., Chulkov, E.V.: Model pseudopotential for the (110) surface of fcc noble metals. *Surf. Sci.* **604**, 804–810 (2010)
181. Hanuschkin, A., Wortmann, D., Blügel, S.: Image potential and field states at Ag(100) and Fe(110) surfaces. *Phys. Rev. B* **76**, 165417, 6 pages (2007)
182. Jennings, P.J.: Surface barrier effects in low-energy electron diffraction. *Surf. Sci.* **25**, 513–525 (1971)
183. Herlt, H.-J.: Elastische Rückstreuung sehr langsamer Elektronen an reinen und an gasbedeckten Wolfram-Einkristalloberflächen. Ph.D. thesis, TU Clausthal (1982)

184. Herlt, H.-J., Feder, R., Meister, G., Bauer, E.: Experiment and theory of the elastic electron reflection coefficient from tungsten. *Solid State Commun.* **38**, 973–976 (1981)
185. Jones, R.O., Jennings, P.J.: Fine-structure analysis of spin-polarized low-energy electron diffraction from W(001). *Phys. Rev. B* **27**, 4702–4711 (1983)
186. Andersson, S.: Low-energy electron diffraction intensities from the clean copper (001) surface. *Surf. Sci.* **18**, 325–340 (1969)
187. Bartos, I., Koukal, J.: On electron damping in VLEED. *Surf. Sci.* **251/252**, 508–510 (1991)
188. Bartos, I., van Hove, M.A., Altman, M.S.: Cu(111) electron band structure and channeling by VLEED. *Surf. Sci.* **352–354**, 660–664 (1996)
189. Sanche, L.: Transmission of 0–15 eV monoenergetic electrons through thin-film molecular solids. *J. Chem. Phys.* **71**, 4860–4881 (1979)
190. Komolov, S.A., Chadderton, L.T.: Total current spectroscopy. *Surf. Sci.* **90**, 359–380 (1979)
191. Pleniewicz, B., Pleniewicz, P., Perluzzo, G., Jay-Gerin, J.-P.: Analysis of low-energy electron transmission experiments through thin solid xenon films in the elastic scattering region. *Phys. Rev. B* **32**, 1253–1256 (1985)
192. Bader, G., Perluzzo, G., Caron, L.G., Sanche, L.: Elastic and inelastic mean-free-path determination in solid xenon from electron transmission experiments. *Phys. Rev. B* **26**, 6019–6029 (1982)
193. Kessler, B., Eysers, A., Horn, K., Muller, N., Schmiedeskamp, B., Schonhense, G., Heinzmann, U.: Determination of xenon valence and conduction bands by spin-polarized photoemission. *Phys. Rev. Lett.* **59**, 331–334 (1987)
194. Goulet, T., Jung, J.-M., Michaud, M., Jay-Gerin, J.-P., Sanche, L.: Conduction-band density of states in solid argon revealed by low-energy-electron backscattering from thin films: role of the electron mean free path. *Phys. Rev. B* **50**, 5101–5109 (1994)
195. Pan, X., Sanche, L.: Mechanism and site of attack for direct damage to DNA by low-energy electrons. *Phys. Rev. Lett.* **94**, 198104, 4 pages (2005)
196. Caron, L.G., Sanche, L.: Low-energy electron diffraction and resonances in DNA and other helical macromolecules. *Phys. Rev. Lett.* **91**, 113201, 4 pages (2003)
197. Caron, L., Sanche, L., Tonzani, S., Greene, C.H.: Low-energy electron scattering from DNA including structural water and base-pair irregularities. *Phys. Rev. A* **80**, 012705, 6 pages (2009)
198. Orlando, T.M., Oh, D., Chen, Y., Aleksandrov, A.B.: Low-energy electron diffraction and induced damage in hydrated DNA. *J. Chem. Phys.* **128**, 195102, 7 pages (2008)
199. Bass, A.D., Sanche, L.: Absolute and effective cross-sections for low-energy electron-scattering processes within condensed matter. *Radiat. Environ. Biophys.* **37**, 243–257 (1998)
200. Sanche, L.: Primary interactions of low energy electrons in condensed matter. In: Ferradini, C., Jay-Gerin, J.-P. (eds.) *Excess Electrons in Dielectric Media*, pp. 1–42. CRC Press, Boca Raton (1991)
201. Bass, A., Sanche, L.: Interactions of Low-Energy Electrons with Atomic and Molecular Solids. In: Hatano, Y., Mozumder, A. (eds.) *Charged Particle and Photon Interactions with Matter: Chemical, Physicochemical and Biological Consequences with Applications*, pp. 207–257. Marcel Dekker, New York (2004)
202. Sanche, L.: Nanoscale dynamics of radiosensitivity: role of low energy electrons. In: Gómez-Tejedor, G., Fuss, M.C. (eds.) *Radiation Damage in Biomolecular Systems*, pp. 3–44. Springer, Dordrecht (2012)
203. Andersson, S.: Plasmon thresholds in the secondary electron yield – I experiment. *Solid State Commun.* **11**, 1401–1404 (1972)
204. Komolov, S.A.: *Total Current Spectroscopy of Surfaces*. Gordon and Breach, Philadelphia, PA (1992)
205. Strocov, V.N.: Unoccupied band structure of layered materials by very-low-energy electron diffraction: implications in photoemission. In: Hughes, H.P., Starnberg, H.I. (eds.) *Electron Spectroscopies Applied to Low-Dimensional Structures*, pp. 161–208. Kluwer, New York (2000)
206. Krasovskii, E.E., Schattke, W., Strocov, V.N., Claessen, R.: Unoccupied band structure of NbSe₂ by very low-energy electron diffraction: experiment and theory. *Phys. Rev. B* **66**, 235403, 11 pages (2002)

207. Barrett, N., Krasovskii, E.E., Themlin, J.-M., Strocov, V.N.: Elastic scattering effects in the electron mean free path in a graphite overlayer studied by photoelectron spectroscopy and LEED. *Phys. Rev. B* **71**, 035427, 9 pages (2005)
208. Strocov, V.N., Krasovskii, E.E., Schattke, W., Barrett, N., Berger, H., Schrupp, D., Claessen, R.: Three-dimensional band structure of layered TiTe₂: photoemission final-state effects. *Phys. Rev. Lett. B* **74**, 195125, 14 pages (2006)
209. Krasovskii, E.E., Strocov, V.N.: Very-low-energy electron diffraction from TiS₂: experiment and ab initio theory. *J. Phys. Condens. Matter* **21**, 314009, 7 pages (2009)
210. Rundgren, J.: Optimized surface-slab excited-state muffin-tin potential and surface core level shifts. *Phys. Rev. B* **68**, 125405, 9 pages (2003)
211. Krasovskii, E.E., Schattke, W.: Surface electronic structure with the linear methods of band theory. *Phys. Rev. B* **56**, 12874–12883 (1997)
212. Krasovskii, E.E.: Augmented-plane-wave approach to scattering of Bloch electrons by an interface. *Phys. Rev. B* **70**, 245322, 11 pages (2004)
213. Thomas, R.E.: Interference effects in the reflection of low-energy electrons from thin films of Au on Ir. *J. Appl. Phys.* **41**, 5330–5334 (1970)
214. Jonker, B.T., Bartelt, N.C., Park, R.L.: Quantum size effect in electron transmission through Cu and Ag films on W(110). *Surf. Sci.* **127**, 183–199 (1983)
215. Born, M., Wolf, E.: *Principles of Optics*, p. 628. Cambridge University Press, Cambridge (1980)
216. Perluzzo, G., Bader, G., Caron, L.G., Sanche, L.: Direct determination of electron band energies by transmission interference in thin films. *Phys. Rev. Lett.* **55**, 545–548 (1985)
217. Jalochowski, M., Bauer, E.: Quantum size and surface effects in the electrical resistivity and high-energy electron reflectivity of ultrathin lead films. *Phys. Rev. B* **38**, 5272–5280 (1988)
218. Kerkmann, D., Pescia, D., Krewer, J.W., Vescovo, E.: Low energy electron oscillations during epitaxial growth of thin films. *Z. Phys. B* **85**, 311–314 (1991)
219. Chiang, T.-C.: Photoemission studies of quantum well states in thin films. *Surf. Sci. Rep.* **39**, 181–235 (2000)
220. Wurm, K.: Spin-polarisierte LEEM-Untersuchungen an dünnen Kobalt-Epitaxieschichten auf W(110). M.S. thesis, Technische Universität Clausthal (1994)
221. Egger, S., Back, C.H., Krewer, J., Pescia, D.: A spin selective electron interferometer. *Phys. Rev. Lett.* **83**, 2833–2836 (1999)
222. Pendry, J.B.: *Low Energy Electron Diffraction*. Academic Press, London (1974)
223. Van Hove, M.A., Tong, S.Y.: *Surface Crystallography by LEED*. Springer, Berlin (1979)
224. Heinz, K., Müller, K.: LEED intensities – experimental progress and new possibilities of surface structure determination. In: *Structural Studies of Surfaces (Springer Tracts in Modern Physics)*, vol. 91, pp. 1–53. Springer, Berlin (1982)
225. Marcus, P.M., Jona, F. (eds.): *Determination of Surface Structure by LEED*. Plenum, New York (1984)
226. Van Hove, M.A., Weinberg, W.H., Chen, C.-M.: *Low-Energy Electron Diffraction*. Springer, Berlin (1986)
227. Heinz, K.: LEED and DLEED as modern tools for quantitative surface structure determination. *Rep. Prog. Phys.* **58**, 637–704 (1995)
228. Garcia de Abajo, F.J., Van Hove, M.A., Fadley, C.S.: Multiple scattering of electrons in solids and molecules: a cluster-model approach. *Phys. Rev. B* **63**, 075404, 16 pages (2001)
229. Soares, E.A., de Castilho, C.M.C., de Carvalho, V.E.: Advances on surface structural determination by LEED. *J. Phys. Condens. Matter* **23**, 303001, 19 pages (2011)
230. Feder, R.: Spin-polarised low-energy electron diffraction. *J. Phys. C Solid State Phys.* **14**, 2049–2091 (1981)
231. Elmers, H.-J.: Spin-polarized low-energy electron diffraction. In: Kronmüller, H., Parkin, S. (eds.) *Handbook of Magnetism and Advanced Magnetic Materials*. John Wiley & Sons, Chichester (2007)
232. Henzler, M.: Defects in surface structure: informations with LEED. In: *Advances in Solid State Physics*, vol. 19, pp. 193–205. Vieweg, Braunschweig (1979)

- 233. Henzler, M.: Measurements of surface defects. *Appl. Phys. A* **34**, 205–214 (1984)
- 234. Henzler, M.: Quantitative analysis of LEED spot profiles. In: Van Hove, M.H., Tong, S.Y. (eds.) *The Structure of Surfaces* (Springer Series in Surface Science), vol. 2, pp. 351–357. Springer, Berlin (1985)
- 235. Lagally, M.G.: Diffraction Techniques. In: Park, R.L., Lagally, M.G. (eds.) *Solid State Physics: Surfaces*, pp. 237–298. Academic Press, Orlando, FL (1985)
- 236. Park, R.L., Houston, J.E., Schreiner, D.G.: The LEED instrument response function. *Rev. Sci. Instrum.* **42**, 60–65 (1971)
- 237. Comsa, G.: Coherence length and/or transfer width? *Surf. Sci.* **81**, 57–68 (1979)
- 238. Lu, T.-M., Lagally, M.G.: The resolving power of a low-energy electron diffractometer and the analysis of surface defects. *Surf. Sci.* **99**, 695–713 (1980)
- 239. Vuorinen, J., Pussi, K., Diehl, R.D., Lindroos, M.: Correlation of electron self-energy with geometric structure in low-energy electron diffraction. *J. Phys. Condens. Matter* **24**, 015003, 7 pages (2012)

<http://www.springer.com/978-1-4939-0934-6>

Surface Microscopy with Low Energy Electrons

Bauer, E.

2014, XIX, 496 p. 216 illus., 71 illus. in color., Hardcover

ISBN: 978-1-4939-0934-6